INVESTIGATION OF THE STRUCTURAL BEHAVIOUR OF MECHANICALLY JOINTED AZOBE BEAMS

Understanding the Key Factors Influencing Load-Bearing Strength in Mechanically Jointed Azobe Beams Using Dowels: An Experimental and Analytical Approach

CIEM0400: THESIS

Kawuki Andrew

AN INVESTIGATION OF THE STRUCTURAL BEHAVIOUR OF MECHANICALLY JOINTED AZOBE BEAMS USING STEEL DOWELS

"Understanding the Key Factors Influencing Load-Bearing Strength in Mechanically Jointed Azobe Beams Using Dowels: An Experimental and analytical Approach"

by

Kawuki Andrew

Student Name	Student Number
Kawuki Andrew	5238293

TU Delft, supervising chair:	JanWillem van der Kuilen
	G.J.P. Ravenshorst
TU Delft :	P.A. de Vries
Wijma Hupkes BV :	Marcus Schiere
Project Duration:	April, 2024 - April, 2025
Faculty:	Civil Engineering and Geosciences, Delft

Cover: Azobé bridge in the Netherlands with mechanically jointed beams: Hupkes Wijma BV

TU Delft

Abstract

This research investigates the structural behaviour of multilayered Azobé timber beams mechanically jointed using steel dowels. Driven by increasing limitations in the availability of large-section hardwoods and the necessity for sustainable material use in construction, the study focuses on understanding the composite action and effective bending stiffness of such assembled beams. Experimental testing—including four-point and three-point bending tests—was performed on both individual lamellae and mechanically jointed beam configurations to determine the global and local Modulus of Elasticity (MOE), interlayer slip, and Effective stiffness EI_{eff}. The results were compared against analytical predictions derived using the γ-method as per Eurocode 5 as suggested by Möhler in the Din 1058, complemented by Schelling's extension for multilayer systems. The findings indicate that the theoretical models often underestimate the gamma values of dowelled Azobé beams in some cases and in other cases underestimate them , and show that slip modulus k_{ser} values differ from those suggested in current standards being far lower than calculated. The research concludes that while current analytical approaches provide a useful baseline, they require refinement to more accurately reflect the performance of high-density hardwoods such as Azobé.

Keywords: Mechanically Jointed Timber Beams, Azobé Wood, Composite Action, -Method, Experimental Bending Tests, Effective Stiffness, Slip Modulus, Structural Behaviour, Schelling.

Summary

A summary...

This thesis investigates the structural behaviour of mechanically jointed Azobé timber beams, focusing on their effective stiffness and load-bearing capacity when connected using steel dowels. Azobé (Lophira alata), a dense tropical hardwood classified under strength class D70, is commonly used in heavy structural applications, particularly in bridge construction, due to its high durability and strength. However, growing export restrictions on large cross-sections of Azobé timber have strengthened the interest in mechanically jointing the beams using smaller sections and mechanical fasteners. This study aims to fill the knowledge gap between existing analytical models, notably those in Eurocode 5, and the actual performance of these mechanically jointed hardwood systems.

The research was driven by three main questions: how to analytically determine stiffness in dowelled timber beams, how joint configurations affect bending stiffness, and how material variations in the timber and dowels influence beam performance. Two beam configurations—two-layer and four-layer beams—were fabricated from Azobé lamellae and connected using 20 mm steel dowels. Prior to jointing, lamellae were tested individually to determine local, global, and dynamic Modulus of Elasticity (MOE). After assembly, both three-point and four-point bending tests were conducted to evaluate stiffness and interlayer slip.

Experimental findings revealed that the actual stiffness of mechanically jointed beams often exceeded analytical predictions, particularly when high-quality lamellae were used. The γ-method, derived in the Eurocode 5 using Möhler's and Schelling's work at Karlsruhe, consistently underestimated the stiffness when applied to Azobé beams. Slip modulus k_{ser} values calculated from experimental data were much lower than those recommended in Eurocode 5 for hardwoods, suggesting the need for recalibration of the theoretical models.

Increasing the number of layers in a beam, while keeping overall depth constant, did not proportionally increase stiffness as expected but if the γ-method is wrongly used then that outcome is achieved thus Schelling's work should be utilised. Moreover, factors such as dowel spacing, moisture content, and lamella grading were found to significantly influence composite action and overall beam performance. Mechanical failures in tested beams included dowel yielding and lamella splitting, often originating at the dowel holes due to stress concentrations.

In conclusion, the thesis demonstrates that mechanically jointed Azobé beams exhibit higher experimental structural performance compared to Eurocode 5 analytical predictions but the slip modulus k_{ser} calculated produces different results from the overly simplified Eurocode 5 method. The current analytical models are inadequate for dense hardwoods like Azobé and should be updated to reflect their material-specific behaviour. Recommendations include the development of revised γ-factor equations tailored for hardwoods, incorporation of empirical slip modulus k_{ser} values, and broader experimental validation to support future code development. These results support the use of mechanically jointed Azobé systems in sustainable, high-performance timber engineering, particularly for applications requiring long-span or high-load resistance.

Acknowledgments

I would like to extend my deepest gratitude to everyone who has been a part of this journey toward completing this thesis. Although the process was long and challenging, I am truly thankful to have reached this milestone. I am deeply grateful to ***Jan-Willem G. van de Kuilen****, who graciously assumed the role of committee chair and provided invaluable guidance during the final stages of my thesis. I am particularly grateful to* ***Geert Ravenshorst****, who initiated this topic together with* ***Marcus Schiere****, whose guidance kept me on track throughout the research. I extend my special thanks to* ***Peter de Vries*** *for his insightful clarifying questions that not only guided the experimental setup but also guided my overall approach to the research. Serving as both my lab mentor and an active committee member, his openness to inquiry—combined with Geert's supportive insights and open door policy helped me refine and clarify the research questions and thesis. I am also grateful to* ***Roel Schipper****, whose timely intervention gave this project a much needed boost when progress stalled. My great thanks also goes to* ***Wijma Hupkes*** *for providing the lamellas and beams that were essential to this study. Without their contribution, this work would not have come to life. I also appreciate* ***Marcus Schiere****for his invaluable assistance structuring the thesis and offering very detailed feedback that helped improved the final document I would also like to acknowledge* ***Derek*** *for his assistance in setting up the lab experiments and for his remarkable flexibility with scheduling. Additionally, my gratitude goes to* ***Giorgos****, whose tips in the lab and work with the DIC was very useful. Finally, I would like to express my heartfelt appreciation to my dear wife* ***Berfu Kawuki****, whose unwavering support and care during difficult times ensured that I always had everything I needed, allowing me to fully focus on my work. Thank you all for your invaluable support.*
...

Kawuki Andrew
Delft, April 2025

Contents

List of Figures

List of Tables

1

Introduction

In the evolving landscape of structural engineering, the emphasis on sustainability has guided a shift towards environmentally friendly construction materials [22]. Wood, especially valued for its ecological and sustainable benefits, is widely used in the construction of various bridge types, ranging from traditional drawbridges to pedestrian bridges. Among the woods used, Azobé stands out due to its high strength (classified as D70) and superior durability, making it ideal for structures exposed to varying climatic conditions.

When making bridge beams with timber, higher cross sections are needed to lower the deflections that ought to be achieved. To accommodate larger spans by increasing sectional height and ensure structural integrity, Azobé beam layers/lamellas are mechanically joined using mechanical fasteners such as dowels(steel or wooden),screws and bolts. This connection affects the global stiffness of the beam by introducing a composite action. Möhler [34] in the 1950s carried out laboratory tests on mechanically joined beams, and his research findings proposed that you could achieve near-full composite action in the beams with the use of dowels. However there remains a huge gap in the practical research of these tropical hardwood beams especiually in the degree of composite action from the analytical recommendations in Eurocode 5 [17]. This significant gap in practical knowledge, is what this thesis will try to fulfil.

Mechanically jointed timber beams are gaining prominence in modern construction due to their versatility, sustainability, and cost-effectiveness [10]. These beams are particularly advantageous for applications in the outdoor environment like bridges as the wood exhibits very high strength and durability characteristics compared to softer woods. Mechanical jointing of the beams allows for the use of smaller timber cross sections together to reach higher beam heights, enhancing resource efficiency while maintaining or even improving the mechanical performance of the beam.

Moreover, sourcing Azobé timber has recently become increasingly challenging, particularly for larger cross-sectional sizes. Azobé Timber from regions like the Congo Basin, Cameroon, and Gabon is typically restricted to a maximum lengths and crossection sizes before shipping due to export regulations. This limitation necessitates the use of built-up members in construction, thus the need for in-depth research into the performance of mechanically jointed timber elements. This thesis aims to understand the behaviour of this performance of mechanically jointed beams.

1.1. RESEARCH PROBLEM

Despite the increasing use of Azobe wood in bridge construction, there remains significant uncertainty regarding the performance of mechanically jointed Azobe beams. Jointing methods, such as using dowels, screws, or other fasteners, are employed to enhance the strength and stiffness of multi-layered beams by increasing the composite action of the beam. However, these techniques change by manufacturer and often lack comprehensive experimental validation, leading to potential discrepancies between theoretical predictions and actual performance. Although existing literature, including Eurocode 5 and various research papers, describes the performance of built-up cross-sections using steel dowels, some manufacturers, such as Hupkes Wijma, a company specializing in timber structures, suspect that their current steel dowel joints may exhibit higher stiffness values than those calculated in the Eurocode 5 like Möhler's findings [35].

1.2. RESEARCH SCOPE

This thesis investigates multilayered Azobe beams which are mechanically joined using steel dowels, as produced by the manufacturer Hupkes Wijma in the Netherlands. The primary objective is to evaluate the effective global stiffness and strength of these beams, targeting a maximum load of 100 kN. Laboratory experiments and analytical calculations will be carried out to achieve these goals, following, where possible, the guidelines specified in Eurocode standards EN 408, EN 26891, and Eurocode 5 [43, 52, 17].

1.3. Research Question

The main research question guiding this study is:

What is the true effective stiffness of mechanically jointed Azobé beams? What factors influence the load-bearing capacity and structural behaviour of these beams?

To address this overarching question, three main sub-questions will be explored:

1. How is the analytical stiffness of mechanically joined beams determined?

2. How do specific joint configurations (e.g., type of fasteners, spacing, pre-stress levels) affect the overall bending stiffness of thee mechanically jointed Azobé beams compared to a monolithic (unjointed) azobé timber members?

3. How do variations in timber properties (e.g., density, moisture content, MOE) and mechanical fastener characteristics (e.g., steel grade, diameter, shear resistance) interplay to influence the load-bearing capacity of the mechanically jointed beams?

And a few other questions that may be answered along the way like;

1. How does the number of layers in multi-layered dowelled Azobé beams affect their effective stiffness and overall structural performance?
2. How do the properties of steel dowels (e.g., diameter, spacing, material strength) influence the load-bearing capacity and stiffness of the beams?
3. What are the specific failure mechanisms that occur within mechanically jointed Azobé beams under bending loads?
4. To what extent does the existing analytical model by Wolfgang [56] accurately predict the effective stiffness and structural behaviour of mechanically joined Azobé beams?
5. What discrepancies exist between theoretical predictions from analytical models, and the experimental results obtained in this study?

1.4. Research Theory and Methods

This section outlines the experimental and analytical methodologies used to investigate the mechanical properties of mechanically jointed Azobé beams.

Initially, four-point bending and three-point bending tests were performed in the elastic range on individual Azobé lamella members to determine their Modulus of Elasticity (MOE). Keeping within the elastic range, the global and local MOE was calculated, which, when correlated with the stiffness measurements, facilitated an estimation of the members' strength [51]. The lamellas could then be graded and the actual MOE values used.

Then the stacked beams of the individual lamellas were also tested with the four-point and three-point bending tests and slip measured between the lamellae at different points.

After these initial tests, the lamellae were transported back to the Hupkes Wijma company, where they were assembled into mechanically jointed beams using steel dowels. The assembled beams then underwent further four- and three-point bending tests in the laboratory to determine their new stiffness. These results were compared with predictions from the analytical model and values compared. All experimental procedures where possible adhered to Eurocode standards Nen-EN 1995-A1+C1 [1], ensuring compliance with established European technical assessment protocols Nen-EN 1380 [39], Nen-EN 338 [2], EN 26891 [52], Nen-EN 383 [42], and Nen-EN 408 [43].

For calculations, an analytical model based on Möhler's and Schelling's theoretical calculations [56], as defined in Eurocode 5 [1],The gamma method was implemented to estimate the stiffness of the beam assemblies. Two configurations, comprising four-layer and two-layer mechanically jointed beams of 3600mm span distance with steel dowels of 20mm placed at 200mm spacing of similar global cross sectional height, were subjected to four-point bending tests to compare their mechanical behaviour under load. The outcomes from these tests were compared with the predictions from the analytical calculations.

This comprehensive approach integrated both experimental data and analytical modelling to ensure a thorough investigation of the behaviour of mechanically jointed timber beams. Further details on these methodologies were expanded upon in chapter 4 and 5.

The thesis shall follow this pattern as described below.

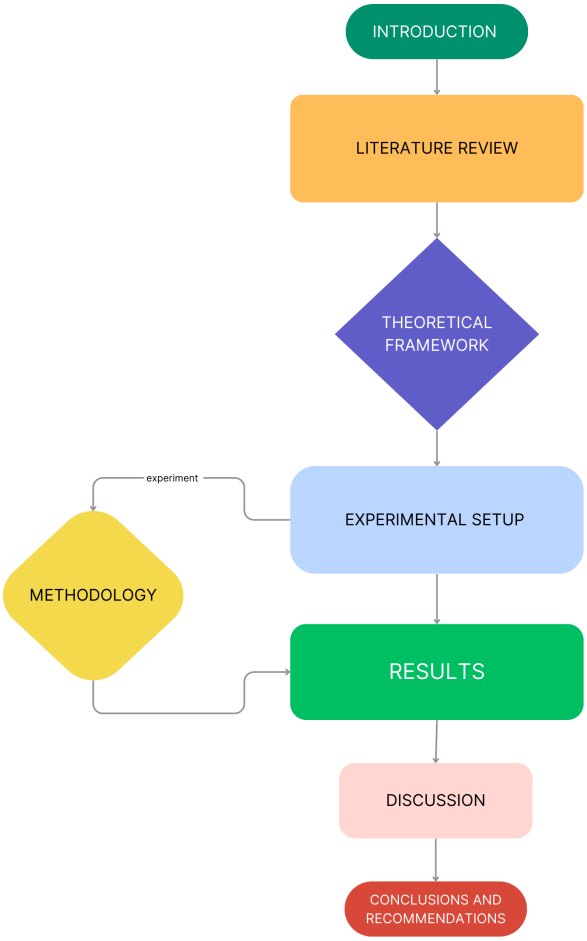

Figure 1.1: Organizational Structure of the Thesis

2

LITERATURE REVIEW

The articles identified in the literature search discuss a variety of topics, including the properties of Azobé wood, the embedment strength of dowels in both soft and hard woods, the shear forces experienced by the timber beams, the bending moments, and the stiffness of the beam. In addition, analytical methods are explored to calculate stiffness, bending moments. To understand the strength and stiffness of multilayered dowelled Azobé beams jointed with steel dowels, we must understand the properties of the Azobé wood itself.

2.1. Material and Mechanical Properties of Azobé

Figure 2.1: Azobé tree as photographed by Dotun

2.1.1. Anatomical and Physical Properties of Lophira alata (Azobé)

Lophira alata, commonly known as Azobé or Ekki, is a significant hardwood species native to West Africa. The species has numerous vernacular names across different regions, including Bongossi (Germany), Kaku (Ghana), Ekki and Akoga (Gabon), reflecting its widespread distribution and cultural importance. Taxonomically, it has several scientific synonyms, including Lophira Alata, Lophira tholloni Tiegh., Lophira spatulata Tiegh., and Lophira procera A. Chev.

Only by fully understanding the anatomy of Azobé wood can we appreciate its mechanical and other physical properties and use it in ways that ensure material compatibility or maximise its potential. At the most practical level, a trunk can be evaluated in terms of its structural qualities, which involves the identification of knots and other growth characteristics. A macroscopic examination of Azobé, indicates several characteristics visible to the naked eye like straight-grained and clear wood segments.

The anatomical structure of L. alata exhibits distinctive characteristics that contribute to its mechanical properties and durability. The wood is diffuse porous with predominantly solitary vessels exceeding 200 micas in tangential diameter. Notable features include white deposits in heartwood vessels, vestured pits, and simple perforation plates. The axial parenchyma appears in continuous tangential lines with prismatic crystals present in both chambered and non-chambered cells. The ray structure is characterised by abundant, non-storied, commonly biseriate rays with homogeneous or sub-homogeneous cellular composition. The fibre structure consists of nonseptate fibres with simple to minutely bordered pits.

The large diameter of the vessel facilitates efficient water transport in living trees, but can affect the permeability of the wood during processing. The presence of white deposits in heartwood vessels and vestured pits contributes to the natural durability of the wood against decay and insect attack. The interlocked grain pattern provides improved mechanical strength and resistance to splitting. These anatomical features result in a wood structure that is particularly well suited for heavy construction and marine applications where durability and strength are paramount.

L. alata trees reach heights of up to 50 metres with trunk diameters of 150 centimetres. The characteristic of the trunk, including a straight, clear, and cylindrical form extending up to 30 metres, makes it particularly valuable for wood production. It is a hard tropical wood that grows year-round, resulting in a relatively homogeneous structure without clear growth rings. Although the species lacks buttresses, it often exhibits basal swelling. The tree occurs predominantly in wet evergreen tropical forests.[19]

Classified as strength class D70 [55] in the EN 338[2] with durability class 1/2, Azobé is ideal for outdoor applications

Azobé wood has inherent properties of the material that directly influence the strength and stiffness of the beams constructed from it. Key material properties include

Variations in these properties across different layers of a beam can impact the overall performance of mechanically jointed beams.

The **mechanical properties** of Azobé as detailed by Jan Willem and Blass in 2004 [53] reflect its response to external forces and is for structural applications. Significant mechanical properties include:Modulus of Elasticity (MOE),Modulus of Rupture (MOR),Shear Strength, tensile and Compression Strength are clearly detailed in that paper.

Table 2.1: Average mechanical properties of the wood.

Property	**Average Value**
Moisture Content (MC)	12%
Bending Strength (MOR)	162.3 N/mm^2
Modulus of Elasticity (MOE)	21,417 N/mm^2
Compression Strength (parallel)	95.6 N/mm^2
Compression Strength (perpendicular)	14.8 N/mm^2
Shear Strength (radial)	14.5 N/mm^2
Janka Hardness (side)	14,012 N
Janka Hardness (end grain)	13,619 N

Azobé's dense, interlocked grain structure and substantial volume of rays contribute to its high strength perpendicular to grain and stiffness [19].

Due to its anisotropic nature, Azobé tends to fail in a brittle manner under tensile stress parallel to the grain but demonstrates ductile behaviour under compression [48].

Figure 2.2: Structure of Azobé and appearance of Azobé grain surfaces

At the microscopic level, the wood fibres within vessels, Azobé possess large, water-conducting cells, along with fibres that contribute to both reinforcement and water transport. Beyond cell walls, the chemical composition, cellulose, hemicellulose, lignin, and other constituents, also critically shapes Azobé performance.

Azobé shares the anisotropic tendencies common to wood species. These arise from elongated cells, orientated cell walls, and variations in cell size during growth, compounded by the preferred orientation of certain cell types, such as rays. The submicroscopic structure of Azobé's cell walls explains why shrinkage and swelling perpendicular to the grain can be 10 to 20 times greater than in the grain direction. Meanwhile, the microscopic features of clear wood explain

why Azobé is 20-40 times stiffer along the grain than across it. Macrolevel attributes, such as knots or twisted fibres, ultimately affect its tensile strength along the grain, which in clear wood samples can exceed 100 N/mm2, yet this can drop below 10 N/mm² in lower-quality sections.[23]

Most of the relevant mechanical properties of Azobé are fall under the grading in the NEN-EN 338 [2], providing mean values and characteristic strengths. However, according to Sandhaas [48], modern timber design codes incorporate multiple safety factors, and even the characteristic values provided account for the nonlinear, viscoelastic and moisture-dependent nature of wood.

Shear failure in Azobé is less common than other failure mechanisms, such as compression perpendicular to the grain. It is important to note that beam shear stress may decrease with an increase in the ratio of shear span to cross-sectional height [29]. Understanding these failure mechanisms is essential for accurately predicting the performance of mechanically jointed beams and ensuring their structural integrity in practical applications.

2.2. Durability Of Azobé Timber

Durability is an aspect of Azobé beams as organic materials. It involves resistance to destructive organisms, ensuring the ability to guarantee the load-bearing capacity and usability throughout the service life of the beams.

The durability and structural performance of Azobé beams (Lophira alata) can be largely attributed to their chemical composition and heartwood formation processes. Unlike temperate wood species that typically contain 1-10% extractives, Azobé possesses a higher extractive content ranging from 5-25%. These extractives, predominantly composed of phenolic compounds and terpenes, play a role in the natural resistance of wood to biological degradation, making it particularly suitable for heavy structural applications in challenging environments. The transformation of sapwood to heartwood in Azobé is characterised by cellular mechanisms that enhance its structural integrity. The formation of tyloses, which are outgrowths of parenchyma cells that effectively seal the vessels, creates a naturally protective barrier within the structure of the wood. This process, combined with the deposition of extractives, results in a virtually impermeable heartwood core that forms the basis of high-performance structural beams. The tyloses influence it's mechanical properties by reinforcing the cellular structure.

The heartwood of Azobé beams has greater resistance to biological degradation compared to sapwood, primarily due to the presence of specific phenolic compounds. Natural resistance mechanisms eliminate the need for chemical preservation treatments, making Azobé beams an environmentally sustainable choice for heavy-duty structural applications.

2.3. Mechanical Properties of Dowels

The performance of mechanically jointed timber beams is influenced by the properties and configuration of the dowels used in their assembly. Steel dowels are commonly used due to their high strength and stiffness, which facilitate efficient load transfer between timber layers [17]. The key factors affecting the overall stiffness and load-bearing capacity of the beam include the dowel dimensions and material properties, properties of the connected timber members, joint configuration, and loading conditions [12]

Figure 2.3: steel dowels used in different sizes

2.3.1. Dowel Dimensions and Material Properties

Various characteristics of the dowels impact joint performance ; including size, length, and diameter; surface condition (clean, smooth, or rough); surface treatment (plating, galvanising, or other coating); and dowel stiffness and flexural properties. These parameters directly influence the load-carrying capacity and deformation behaviour of the connection.

Larger dowel diameters generally enhance the stiffness of the connection, reduce interlayer slip, and can transfer more load before failing due to their increased cross-sectional area, thereby improving overall structural performance [10].

2.3.2. Properties of the Connected Timber Members

The mechanical properties of the timber components are determinants of joint performance. These include compressive and embedding strength; elastic and creep moduli; and displacement modulus and elastic or plastic bearing constant. These properties are intrinsically related to the density, grain direction, and moisture content of the wood. In addition, friction between the dowel and its surrounding wood material contributes to the overall stiffness of the joint.

While increasing dowel size can enhance stiffness and strength, practical limits exist. There must be a proportionality between the size of the dowel and the wood elements being connected to ensure effective load transfer without introducing stress concentrations or causing damage to the timber members.

The strength of the embedding f_h represents the resistance offered by the wood surrounding the dowels, and plays a vital role in the stability and durability of the connections. Recent studies have proposed updated models for calculating the embedment strength based on experimental data, particularly for hardwoods such as Azobé [46].

2.3.3. Joint Configuration

The geometric arrangement of the connection affects its structural behaviour. Important considerations include the use of single or multiple dowels per joint; the presence of single, or multiple shear planes; member thickness; edge and end distances of the dowels etc.

However, the right spacing and edge distances are to prevent wood splitting due to forces acting transversely to the grain and to ensure an effective load distribution [4]. The European standard Eurocode 5 [17] provides guidelines for the design of dowel joints, including recommendations for minimum spacing and edge distances.

2.3.4. Loading Conditions

The nature of the applied loads substantially influences the behaviour of the joint of the dowel. Relevant factors include the type of loading (static, repetitive, or dynamic); duration (short or long-term); rate and range of loading; and the time interval between dowel insertion and load application. These factors affect both the immediate response and long-term performance of the dowelled connection.

The slip modulus k_{ser} of the lamellae interface joints, which measures the resistance of the joint to relative movement under load, is a key parameter for predicting joint performance [7]. It is essential to calculate deformations in wooden structures and the k_{ser} depends on factors such as the diameter of the dowel and the density of the wood [46].

Optimising parameters such as size, spacing, slip modulus, etc. can improve load bearing capacity and reduce the risk of joint failure in mechanically joined beams. [28].

2.4. Manufacturing Process

The manufacturing process of Azobé beams begins with selecting Azobé lamellas from climate-controlled facilities to ensure optimal moisture content. The lamellas are visually graded and with the known sizes, these lamellas are then precisely planed and dimensioned. Once the appropriate dowel dimensions are determined, the lamellas are assembled in a stacked configuration with a pre-camber to account for anticipated load-induced deflections. A CNC drilling machine is used to accurately bore aligned holes through the lamellas. These holes are produced with diameters equal to, or marginally less (by less than one millimeter) than, the specified dowel sizes. Finally, the dowels are hammered into the holes while preserving the shape and pre-camber, resulting in a mechanically jointed beam.

Proper preparation of dowel holes is essential for the achieving optimal performance in mechanically jointed timber beams. According to Ehlbeck and Werner [16], the dowel holes should be pre-drilled to the exact nominal diameter of the dowels to ensure a proper fit and effective load transfer. In some cases, it is recommended to replace one or more dowels with fitted bolts or screws to enhance joint cohesion during assembly and prevent gaps between individual members [17].

The manufacturing process employed by Hupkes Wijma involves pre-drilling holes slightly smaller than the dowel diameter to achieve a tight interface fit when inserting the dowels. Additionally, a pre-camber is introduced to the beams during assembly to counteract deflections under load and improve structural performance. However, the effects of these practices on the slip modulus and overall joint behaviour are not fully documented and require further investigation.

Undersized holes can cause splitting or excessive insertion forces during dowel installation, potentially damaging the timber [4]. Oversized holes may lead to inadequate load transfer and increased deformation. Therefore, adherence to recommended drilling practices is essential for ensuring the desired performance of mechanically jointed beams.

2.4.1. Number of Dowels

In multi-layered beams, the number of dowels affects the slip modulus k_{ser} and the γ factor, which govern the beam's stiffness. More dowels increase inter-layer slip resistance [49], distribute load more evenly, reduce displacement, and raise γ, thus promoting near full composite action [8]. Connection strength also improves, as multiple dowels share shear and bending forces until the timber's inherent strength becomes the limiting factor [27].

However, practical considerations must be taken into account:

Spacing and Edge Distances: Proper spacing and edge distances are essential to prevent splitting of the timber and to ensure effective load transfer. Minimum requirements for spacing and edge distances are specified in design standards such as EN 1995-1-1 (Eurocode 5) [17] and will be elaborated on more in the 4th chapter.

Diminishing Returns: Beyond a certain point, adding more dowels may not increase the connection's strength or stiffness due to limitations imposed by the timber's capacity and the potential for localized crushing around the dowels. The concept of the effective number of fasteners n_{ef} is used in design to account for this phenomenon and is well detailed in the Eurocode 5 [17].

2.4.2. Dowel Arrangement

The arrangement of the dowels and their material properties influence the load-carrying capacity and stiffness of multilayered beams. [8].

The arrangement of the dowels can also affect performance. However, some studies indicate that certain factors, such as the staggering of dowels, may have a negligible impact on the overall strength and stiffness of the assembly [16].

Layer Orientation

The orientation of individual layers within a multilayered beam influences mechanical properties such as modulus of elasticity and strength. Aligning the grain direction with the primary stress directions maximises structural performance.

2.5. Mechanically Jointed Beams Theory γ-Method

To analyse multi-layered beams, the γ-method (Gamma method) is commonly used to determine stiffness and account for the semi-rigid connection between layers [35]. This method considers the slip between layers and provides a more accurate prediction of the beam's deflection and load-bearing capacity.

Figure 2.4: A Bridge setup inside the factory of Hupkes Wijma displaying clearly the mechanically jointed beams manufactured on site on the sides

The γ factor for composite action between composite members in Eurocode 5 originates from the analytical modeling of the slip behaviour at the interfaces of the composite assembly. In essence, it is a non-dimensional parameter derived from the solution of the differential equations governing the relative slip between layers that are connected via fasteners or adhesive and goes from 0 (no composite action) to 1 (full composite action). This derivation assumes linear-elastic behaviour for both the timber and the connectors and considers factors such as the slip modulus $k_{ser}$of the connectors, the spacing between them (s), and the Modulus of elasticity (E) of the individual layers.

The γ-method, as outlined in the Eurocode 5 [1] provides the simplest framework for calculating the flexural properties of mechanically jointed beams.[44]. In Germany, Tests were previously done by Prof. Möhler (Experiments with Bongossi Wood - Test Report). On multi-layered (max 4 layered) Azobé beams held by dowels. He also tested the shear strength of the dowels embedded in timber-to-timber connections using the 16mm and 24 mm and 30mm.

Specifically, when three members are intended to act as a composite beam, there are two

interfaces at which slip can occur. The γ factor quantifies the reduction in effective stiffness EI_{eff} due to the partial interaction across these interfaces. By solving the governing equations under appropriate boundary conditions, Eurocode 5 introduces this γ factor to adjust the idealized fully composite bending stiffness to a more realistic value that mirrors the actual performance of the connection.

For further details on the derivation and application of this factor, one can consult the notes and technical annexes accompanying EN 1995-1-1, which present the analytical, probabilistic, and experimental basis for the approach. Additional guidance on a two-member section can be found in Annex 5 of Timber Engineering – Design Principles by Sandhaas [47].

Wolfgang Schelling further added the possibility to do calculations of the γ stiffness factor of 3 - layered beams to n number of layers [56] and with this extension made it possible to calculate any cross section type within the setup. In his formulation he used symmetry and concluded that the gamma factor for the central beam given an odd number of layers was still 1 in this calculation.

This method expanded by Schelling, accounts for the stiffness contributions of individual layers and the inter-layer slip facilitated by dowels by relying on the slip modulus k_{ser}. The method has also been validated through numerous experimental studies, including those by [36], which examined the behaviour of multi-layered beams with inter-layer slips. These studies emphasize the role of the γ-factor in predicting the mechanical behaviour of complex timber assemblies under various loading conditions.

The γ-factor will be discussed further in the next chapter

2.6. Possible Failure Mechanisms of Mechanically Jointed Beams

Mechanically jointed beams predominantly exhibit two principal failure mechanisms: brittle failure and ductile failure.

Brittle Failure : This type of failure occurs when the tensile stresses in the lowest lamella exceed the wood's bending strength, causing the lamella to rupture. Accurately determining the bending stresses throughout the cross-section is critical for predicting this mode of failure.

In brittle failure mechanisms, a premature failure by splitting can also occur. This process can begin when a crack initiates around the dowel holes and then propagates along the wood grain dowel holes ultimately causing the lamellae to split.

Ductile Failure : In contrast, ductile failure arises from the steel dowels yielding in shear, thereby permitting substantial interlayer slip. This behaviour indicates that the connections undergo considerable plastic deformation, which can allow for larger deflections and energy dissipation prior to complete failure. this is indeed not a true failure as the dowels continue to perform in shear even when deformed

Shear Failure and Interlayer Slip :

Early work by Johansen [26] laid the foundation for understanding shear failure in dowel joint connections. mechanically jointed assemblies are made of these connections. His research focused on interlayer slip between members, which is resisted by the shearing action of dowels placed between the layers. The number of shear planes directly influences how dowels yield or fail, resulting in different failure patterns.

Further studies by Natterer *et al.* [37] corroborated these findings and demonstrated shear failure in multi-layered, mechanically jointed systems, including tests conducted on up to six members. As more shear planes are introduced, the dowel arrangement and slip behaviour become increasingly complex, and an understanding of how interlayer slip evolves under loading.

Embedment Strength And Embedment Stiffness Embedment stiffness refers to the resistance offered by the wood fibres surrounding a dowel, as it is inserted into the timber member. This resistance is for ensuring the stability and load-bearing capacity of the connection. It is a critical parameter in assessing the load carrying capacity of joints with dowel-type fasteners, along with the yield moment of the dowels.

According to the European timber design code Eurocode 5, embedment strength formulas are applicable to all timber species and are dependent on fastener diameter and material density. Although the tests were primarily focused on softwood, recent experimental research has expanded to include European and tropical hardwoods.([48])

The visual representation below according to sandhaas highlights the material's response under compression load during an embedment test. It can be seen the difference in embedment strength of Azobé, a typical tropical hardwood, compared to other timber species under similar conditions.

In further research by [54], the concept of embedment stiffness is explored with an emphasis on its critical role in ensuring the stability and load-bearing capacity of timber connections.

These studies collectively contribute to a deeper understanding of mechanical behaviours in these beams, informing both current practices and future developments in structural engineering and design.

2.7. The Research

While previous studies have primarily focused on numerical analyses of the behaviour of timber dowel connections and inter-layer slips, there is a significant need for further laboratory experiments to determine the actual stiffness and strength of mechanically jointed timber beams. Experimental validation is to bridge the gap between anlaytical calculations and real-world performance.

Beams with different numbers of layers but similar overall height: The last substantial experimental study was conducted in the 1960's by Möhler [35], which focused exclusively on beams composed of four layers. To fully understand the mechanical behaviour of mechanically jointed beams, it is essential to investigate beams with varying numbers of layers—such as a two-layer and four-layer configurations — while maintaining the same overall beam height. This approach will help assess how the number of layers affects stiffness, strength, load distribution, and failure mechanisms.

Validation of the analytical calculations in the eurocode for hardwoods like azobé. Existing analytical models incorporated into Eurocode 5 [17] focused on softwoods mostly and have not been updated, there lacks validation of this against experimental data for hardwoods like Azobé. analysis need experimental verification to ensure their accuracy in predicting the behaviour of mechanically jointed beams under various loading conditions.

3

Work By Karl Möhler

Karl Möhler's 1968 test report "Versuche mit Bongossiholz"[34] had asprimary onbjective to perform an investigation into the the structural performance of the tropical hardwood Bongossi (Azobé)in construction. The report was motivated by the growing use of Bongossi in West Germany in civil structures e.g. for pedestrian bridges and other components and the lack of existing data for design.

3.1. Analysis of Möhler's "Versuche mit Bongossiholz – Prüfbericht"

Möhler, in collaboration with the Dutch timber company T.C. Groot (Lemmer), aimed to determine key material properties of Bongossi and to evaluate the behaviour of rod-dowel connections and multi-layer beams made from this hardwood. The ultimate goal was to provide data and design recommendations, addressing inquiries from building authorities and filling gaps in standards (since existing codes had no specific values for Bongossi or rod-dowel joints) . In summary, the research question was: How can Bongossi wood's strength properties and dowel-connected beam performance be quantified, and can standard design methods be applied to this material?

Description of Beam Specimens

The beam specimens tested were large composite timber beams made of Bongossi lamellas joined with steel rod dowels like in this thesis. Specifically, the report examined 15×60 cm cross-section beams composed of multiple Bongossi wood planks (lamellae) mechanically connected to act together. The company provided beams assembled from individual Bongossi members (dense, tropical hardwood sections) using steel Stabdübel (rod dowels) as connectors. Two full-size beam configurations were tested: one beam was built from four lamellas (stacked to form the 60cm depth) with a pre-camber (upward curvature) introduced during fabrication, and another beam had a similar 15×60 cross-section but with a different lamella arrangement (e.g. possibly three lamellas – a "three-part" beam). Each lamella was a single sawn timber element of Bongossi(Azobe), and when bolted together with multiple steel dowels across the depth, they formed a composite section(Mechanically jointed beam). The dowel diameters used ranged (e.g., 16mm, 24mm, up to 30mm) to study different connector sizes. In the first beam (Träger Nr.1), a slight construction deviation was noted – some dowels were placed a bit closer to the edge than planned – whereas in the second beam (Träger Nr. 2) the dowel positioning matched the design exactly. Apart from that, both beams had comparable dimensions (15 cm width, 60 cm depth) and were several meters long to allow bending tests.

3.1.1. Experiments Conducted (Methodology and Setup)

Möhler's experimental program was divided into three parts, addressing: (1) fundamental material properties of Bongossi, (2) behaviour of steel dowel connections in Bongossi, and (3) performance of multi-layer (dowel-jointed) Bongossi beams under load. The methodology and setup for each part were as follows:

Material Property Tests

A series of standard small-specimen tests were carried out to quantify Bongossi's basic mechanical properties. Following DIN norms, compression tests were done both parallel to grain (axial compression) and perpendicular to grain. Small cubes (e.g. 3×3×6cm) were compressed to determine compressive strength along and across the fibers. Shear tests parallel to grain were performed using standardized block shear specimens to measure shear strength. Bending tests (static flexural tests) were conducted on clear wood specimens of two sizes – 5×5cm and 12×12cm cross-sections – in a four-point bending setup (per DIN52186) to obtain the bending strength and modulus of elasticity (MOE) . The bending MOE was calculated from load–deflection data. Additionally, embedment (bearing) strength tests were done: steel dowels were loaded in holes through wood blocks to measure the Lochleibungsfestigkeit (embedment strength of wood parallel to grain), which is critical for dowel connections. All samples were cut from a stock of Bongossi timbers provided by the company (dimensions 5×5×150cm and 12×12×300cm stock, from which test specimens were extracted). The wood's density (Rohdichte) and moisture content were recorded for each specimen. (In particular, Bongossi is extremely dense; the average density was approximately 1170kg/m3, and some large sections retained core moisture above 30% during testing.) These material tests followed relevant standards to ensure reliable property values.

Dowel Connection Tests

The next phase examined Stabdübelverbindungen, i.e. steel rod dowel connections in Bongossi wood. Möhler investigated double-shear dowel joints ("zweischnittige" connections), meaning that each dowel passed through two shear planes (as in a sandwich of wood-steel wood or wood-wood-wood). The test specimens for these connection tests consisted of Bongossi wood members joined by one or more steel dowels, loaded in a setup to simulate joint shear conditions. The variables studied included the dowel diameter (d) and the. By testing multiple diameters (e.g. 16mm, 24mm, 30mm) and wood thickness configurations, the experiments aimed to see how dowel size and the thickness of wood it passes through affect the joint strength and stiffness. Each connection specimen was loaded until failure in a tensile testing machine or similar rig, while measuring the load–displacement (slip) Behaviour. The failure modes (whether the wood crushed around the dowel, the dowel yielded, or the wood split) were documented. For each configuration, the ultimate load capacity of the joint and the slip modulus (initial stiffness of the load-slip curve) were determined. These tests yielded data for allowable dowel loads and slip modulus C in Bongossi, which were absent from current codes. Results were tabulated (e.g. Table7 in the report compiles the outcomes for various diameters and thicknesses), and they enabled comparison of Bongossi's joint performance to known values for softwood.

Beam Bending Tests

The final and most experiments were full-scale bending tests on the dowel-laminated Bongossi beams (section 15×60 cm as described). Each composite beam was simply supported and loaded in bending (a four-point bending setup was used to create a constant moment region in the middle). Numerous steel dowels were used along the span to connect the layers; their pattern and spacing followed design guidelines (edge distances of about 6.5 cm and certain spacing along the beam length). Instruments measured the mid-span deflection of the beam and

possibly the relative slip between layers (to assess partial composite action). Träger Nr. 1 (the first beam with four lamellas and pre-camber) was tested in incremental stages: initial "service-level" load tests to evaluate stiffness, followed by loading to higher levels until near failure. Träger Nr. 2 (the second beam) was then tested, likely to failure, to compare Behaviour. Throughout these tests, observations were made on whether full composite action was achieved or if slip occurred between layers. The pre-camber in the first beam was noted – under load, the beam's deflection would first cancel out the camber before sagging, so they monitored how the camber influenced the load-carrying Behaviour. Key measurements obtained were the effective bending stiffness EI_{eff} of the composite beams (to compare against theoretical predictions) and the ultimate bending capacity. After testing, the beams were examined for failure modes: e.g. whether failure happened by dowel yielding or wood crushing at the connections, or by wood flexural failure in the extreme fibers. These results were compiled (Table8 in the report contains the beam test results and specifics of steel grades of dowels, etc.) and used to evaluate design methods.

3.2. Findings from the Experiments

Material Strength

Bongossi wood was confirmed to be very dense. The average density was about roughly 1170kg/m³, far higher than typical construction softwoods. Moisture content during testing was approximately 32.9%. Its compressive strength parallel to grain was measured around 58–59N/mm² (with 10% coefficient of variation). Compression strength perpendicular to grain was measured for both tangential (9.74 N/mm²) and radial (12.54 N/mm²) loading. Shear strength parallel to grain averaged 15.83 N/mm². The modulus of elasticity (MOE) in bending was measured as 16,000–20,000N/mm². Additionally, the embedment (bearing) strength of Bongossi (resistance to dowel bearing) was determined to be high. For instance, under parallel-to-grain loading of steel dowels, the wood's embedment strength values were above those for pine or spruce. In summary, the material tests justify Bongossi's use in heavy-duty applications, albeit with the consideration of its brittle nature

Dowel Connection Behaviour

Rod-dowel connection tests revealed that dowel diameter and wood thickness (slenderness ratio) affect connection strength and stiffness. Larger dowels (24mm and 30mm) achieved higher load capacities; however, failure modes varied. Smaller dowels failed by wood crushing or splitting (embedment failure), whereas some 30mm dowels reached the yield strength of the steel—using standard St37—indicating that steel quality is diameter-dependent. Specifically, only the 30mm rods consistently met the St37 grade, while the 16mm and 24mm rods showed reduced strength, likely due to manufacturing differences. The slip modulus (C) of the Bongossi connections was quantified, with the wood's hardness yielding a high initial stiffness and minimal slip under service loads. Load–displacement curves exhibited linear behavior up to approximately twice the permissible load, with maximum loads of about 247–280kN for 16mm dowels, 545–744kN for 24mm dowels, and 858–1128kN for 30mm dowels. Brittle failure modes, particularly wood splitting near dowel holes, occurred when edge distances were insufficient. For example, in beam Träger 1, dowels placed 1–2.5 cm too close to the edge likely induced premature local splitting. The findings establish specific allowable loads for various dowel sizes in Bongossi and recommend slip modulus C values for design calculations, demonstrating that mechanical dowel connectors can form strong, stiff joints in this hardwood—albeit with a brittle failure mode.

Composite Beam Performance

Composite beam performance was evaluated through tests on two full-scale Bongossi beams, each 6000mm long with a 150×600cm cross-section. The beams were constructed from four lamellas, each measuring 150×150cm, connected by 20mm steel dowels spaced at 150mm intervals. Testing under both center-point and two-point bending configurations involved measuring midspan deflections and slip between lamellas until failure. An effective bending stiffness of approximately 20,830 N/mm^2 was determined, which corresponded closely with predictions from the *gamma*-method and other analytical models when the experimentally determined slip modulus was applied. One beam achieved a maximum load of 228kN with a deflection of 189mm, while the other reached 190.8kN with a deflection of 114mm. In one specimen, an initial upward camber was observed that was overcome during loading, leading to conventional downward deflection without affecting the ultimate capacity, although it contributed to smaller service deflections. Failure occurred primarily due to tensile rupture at the beam's bottom or excessive slip in the connections; one beam exhibited minor shear slip and slight connector yielding prior to overall failure when the extreme fibre stress in the wood was reached. Additionally, proper dowel spacing and edge distances proved critical in preventing premature splitting, as evidenced by specimens with optimal layouts. The 30mm dowels yielded plastically at peak load, whereas thinner or lower-grade dowels may not yield before wood failure, potentially shifting the failure mode. These findings confirm that layered Bongossi beams can achieve near-composite action, transferring loads effectively through the dowel connectors and performing comparably to solid beams of equivalent cross-section.

3.3. Conclusions by the Möhler

Dowel-jointed Bongossi beams can be safely and effectively designed using existing engineering methods. The tests showed that composite beams with 2 or 3 layers (and even 4-layer, as in the one beam) behave as predicted by standard formulas. In fact, Möhler concludes that one can calculate two- and three-part composite Bongossi beams using the equations given in DIN1052 (the old German timber design code) for mechanically jointed beams, with the experimentally determined parameters . In practice, this means the γ-method (slip factor method) in the Eurocode 5 is applicable to Bongossi. the slip modulus and permissible dowel loads obtained from the tests should be used, but no fundamentally new design approach is required.

Because prior standards did not have values for rod dowel connections in Bongossi, Möhler's results fill that gap. The report likely recommends that the characteristic strength values (embedment strength, etc.) and slip modulus for Bongossi be incorporated into code provisions.

Möhler concludes that to ensure reliable performance, proper detailing of dowel connections is crucial. Adequate edge distances, spacing, and using the appropriate dowel diameter relative to member thickness will prevent premature wood failures. The tests indicated that when these details are respected, the failure mode can be ductile (steel yielding) or at least as predictable as other timber connections. So, design recommendations include using the provided slip modulus values and perhaps limiting the slenderness ratio or using multiple smaller dowels rather than one very large dowel, to balance wood and steel capacities.

The study confirms that Bongossi's high material strength can be utilized in structural applications. For instance, the allowable bending stress and compression stress derived from the tests are much higher than those for pine or other common timbers. Möhler likely notes that Bongossi's brittleness (low deformation at failure) means safety factors and careful quality control are needed.

The outcome is that these experiments provided the confidence and data to use Bongossi in

engineered structures such as long-span beams and bridges. Möhler's work paved the way for design methods of mechanically-jointed beams (which later were incorporated into Eurocode5) . The report's conclusions emphasize that mechanically jointed Bongossi beams are a viable construction solution.

4

THEORETICAL FRAMEWORK

This section delineates the multitude of variables central to the research project, accompanied by graphical representations. At its core lies the exploration of the strength and stiffness of dowelled multi-layered Azobe beams, comprising more than three layers. The key to this framework is a profound understanding of the structural properties of Azobe wood, notably its density, modulus of elasticity (MOE), and dowel embedment strength, all of which exert direct influence on the overall strength and stiffness of the beams. Moreover, the inter-layer slip between members, facilitated by dowel joints, significantly shapes the behaviour of multi-layered beams under load. Employing this seeks to compare the experimental findings with analytical solutions derived from Eurocode 5 to see if there is alignment in results

4.1. Introduction To Mechanically Jointed Timber Beams

Mechanically jointed timber beams consist of two or more timber components joined together using mechanical fasteners, such as dowels or screws, to enhance structural performance. The fundamental principle involves distributing loads through the jointed layers to achieve improved flexural stiffness, strength, and stability [8]. The inter-layer connections ensure effective load transfer, reducing differential movement between layers and enhancing overall structural integrity. The space in the interlayers typically serves only to transmit shear that is absorbed by the fasteners. Upon deformation, the total beam cross-section of the members no longer remains planar since the individual layers deform longitudinally due to shear. Consequently, it cannot be calculated using Euler-Bernoulli beam theory, as it violates the fundamental principle of maintaining planarity.

The load bearing capacity, stiffness, and degree of composite action in mechanically jointed timber beams are between those of glued and unjointed timber [30]. They are frequently used in outdoor applications to achieve nearly the same composite behaviour that would otherwise be obtained by gluing hardwoods. However, this approach introduces challenges such as glue line delamination and reduced adhesive penetration, problems related to the denser fibre structure of hardwoods, which have been thoroughly examined by Leggate [32].

As Kreuzinger et al. show in [6], the bending stress analysis of these members - compared to pure solid and unjointed timber in a three-layer configuration, as illustrated in the figures below - shows that unjointed timber undergoes significantly greater deformation than sawn timber, with jointed timber showing intermediate deformation characteristics.

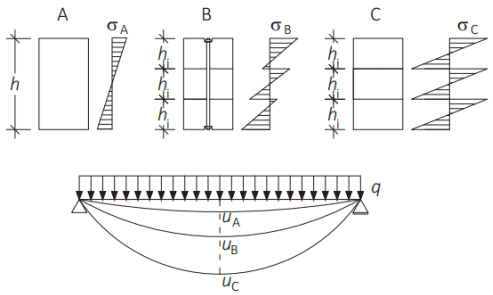

Figure 4.1: Bending stress comparison of solid timber, mechanically jointed timber, and unjointed timber.

Mechanical beams are classified as composite beams, encompassing a wide range of possible configurations, as illustrated below. To analyse these semi-rigid jointed beams, the γmethod is typically employed for configurations involving up to three layers. For assemblies exceeding three layers, Schelling [56] or the shear analogy method are generally utilized.

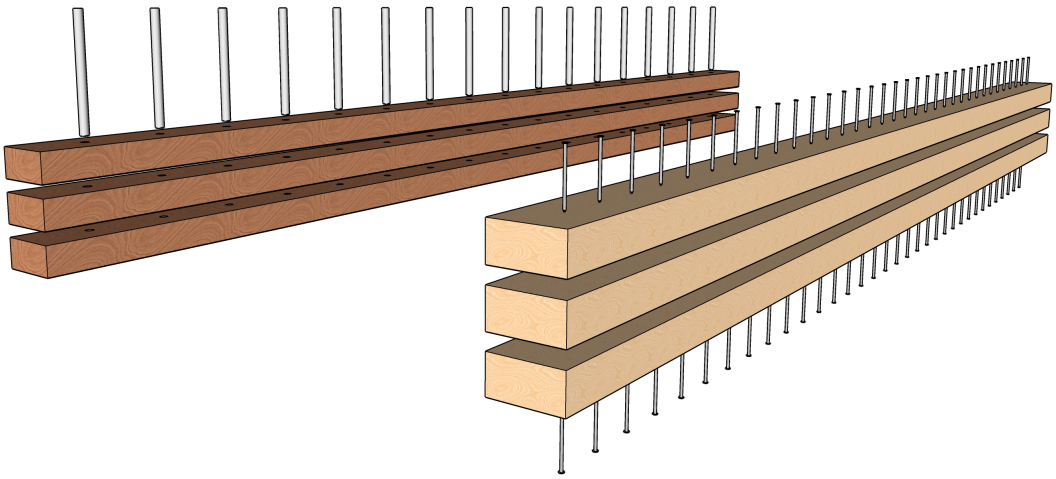

Figure 4.2: Steel dowel-jointed beams are shown in dark brown wood, while screw-jointed beams are depicted in lighter wood.

4.2. Gamma Method for Multi-layered Beams (γ)

4.2.1. Historical Development: Möhler's and Schelling's Contributions

The γ-method, originally proposed by Möhler [33], was a breakthrough in understanding the stiffness behaviour of mechanically jointed multi-layered beams. Möhler introduced the concept of inter-layer slip, which significantly affects the effective stiffness of the composite beam. Later, Schelling refined this method, extending its applicability to a wider range of beam configurations, including varying cross-sectional geometries and complex joint arrangements [56] explained in the next section. The contributions of Möhler laid the foundation for the analytical evaluation of multi-layered beams, bridging the gap between theoretical predictions

and experimental observations.

4.2.2. Mathematical Formulation

The effective flexural stiffness $(EI)_{\text{eff}}$ of a mechanically jointed beam with n layers using the γ method is given in the Eurocode [41] by:

$$(EI)_{\text{eff}} = \sum_{i=1}^{n} \left(E_i \cdot I_i + \gamma_i \cdot E_i \cdot A_i \cdot a_i^2 \right) \tag{4.1}$$

and γ_i is the reduction coefficient for the i-th layer, calculated as:

$$\gamma_i = \frac{1}{1 + \frac{\pi^2 \cdot E_i \cdot A_i \cdot S_i}{K_i \cdot \ell^2}} \quad \text{for } i = 1, 3 \qquad \gamma_2 = 1 \tag{4.2}$$

Where:

E_i - modulus of elasticity of the i-th layer.

I_i - moment of inertia of the i-th layer.

A_i - cross-sectional area of the i-th layer.

a_i - distance from the centroid of the i-th layer to the neutral axis of the composite section.

K_i - slip modulus (stiffness of the connection) for the i-th layer.

S_i - coefficient related to the spacing or arrangement of the fasteners.

ℓ - span length of the beam.

In a three-member connection as specified by Eurocode 5 [17], the coordinates a_i of the neutral axes are found by considering both the geometry and the moduli of elasticity E_i of the individual members. The coordinate of the neutral axis in the second member, a_2, can be written as

$$a_2 = \frac{\sum_{i=1}^{3} x_i \cdot E_i \cdot A_i}{\sum_{i=1}^{3} E_i \cdot A_i} = \frac{E_1 A_1 (h_1 + h_2) \; - \; E_3 A_3 (h_2 + h_3)}{2 \left(E_1 A_1 + E_2 A_2 + E_3 A_3 \right)} \tag{4.3}$$

The center of gravity x_{0c} of the entire beam in relation to a reference axis 0 is determined by the equation below with x_{0i} as the distance from reference axis 0 to the centre of gravity of that member

$$x_{0c} = \frac{\sum_{i=1}^{n} x_{0i} \cdot E_i \cdot A_i}{\sum_{i=1}^{n} E_i \cdot A_i} \tag{4.4}$$

Once a_2 is obtained, the neutral axes in the other two members, a_1 and a_3, follow from simple shifts: Here, h_i denotes the thickness (or height) of each member, A_i its cross-sectional area, E_i its modulus of elasticity, and x_i the distance from a chosen reference axis.

$$a_1 = -\frac{h_1 + h_2}{2} + a_2 \quad \text{and} \quad a_3 = \frac{h_2 + h_3}{2} + a_2 \tag{4.5}$$

The γ- method only applies to three given members. Attempting to calculate the γvalue for more members will result in a continuous increase in the effective (EI) if the width and height

remain constrained, with changes occurring only in the height of the members. The following graph provides a summary of this effect.

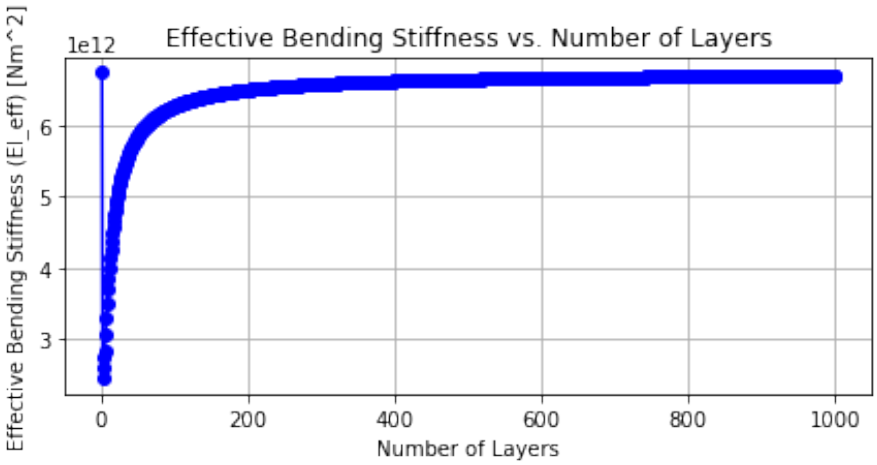

Figure 4.3: Effective bending stiffness (EI_eff) based on only the γfactor calculation vs. number of layers, with total height and width fixed while layer thickness decreases as the number of layers approaches infinity.

However, if the true stiffness is determined from the full effective EI while increasing the number of layers—but keeping the cross-sectional height constant—this behavior can be expected across different stiffness levels. This is based on the assumption that, regardless of how many layers are added, the stiffness values remain similar for each corresponding case.

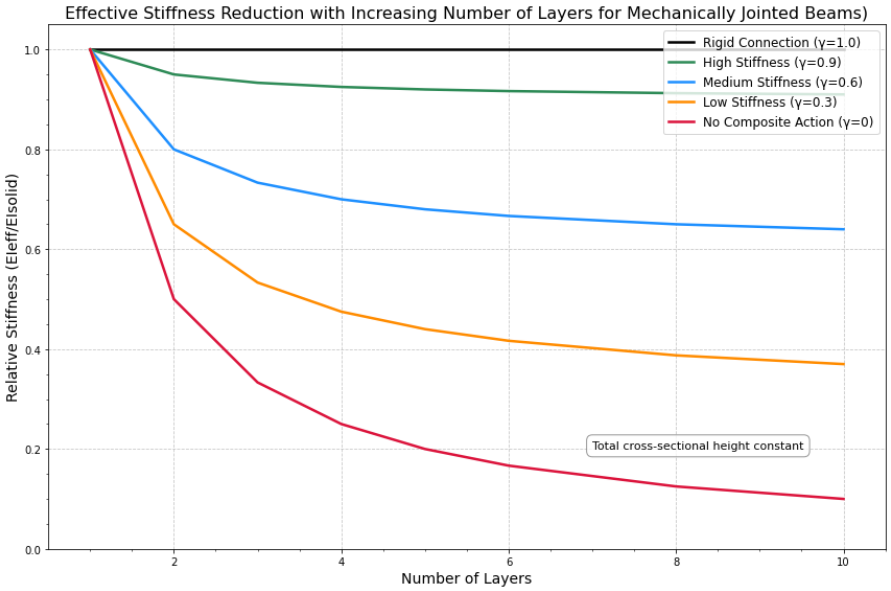

Figure 4.4: Effective Stiffness Reduction with Increasing Number of Layers for Mechanically Jointed Beams

4.2.3. Slip Modulus K_{ser} and Its Significance

The slip modulus, denoted as K_{ser}, is a critical parameter in the analysis of mechanically jointed timber structures. Also known as slip stiffness or slip resistance, it quantifies the resistance offered by a joint or connection to relative movement or slippage between its components under applied loads. Specifically, it measures the ability of mechanical joints, such as with dowels, to

resist slip when subjected to loading.

When a load is applied to a structure, it induces forces and displacements that may cause relative movement between the connected members. The slip modulus characterizes the deformation behaviour of the connection under load, typically expressed as the force required to induce a unit displacement (e.g., force per unit of slippage). It is an important parameter in predicting the mechanical performance of connections and, by extension, the global response of the structure.

The value of the slip modulus is influenced by various factors, including the dowel diameter and the density of the timber. Accurate determination of K_{ser} is essential for analysis, as it directly affects the predicted calculated stiffness and strength of the connections.

Methods for Determining Slip Modulus

The slip modulus can be determined using both experimental and analytical methods. Experimentally, it can be obtained through shear tests on connections, following standardized procedures such as those outlined in EN 26891 [52] or EN 383[42]. These tests involve applying load to a joint and measuring the corresponding displacement, allowing for the direct calculation of K_{ser}.

The standard provides an empirical formula for the slip modulus K_{ser} (serviceability stiffness) per shear plane per fastener as a function of fastener diameter d and timber density ρ_mm . For example, for steel dowels in wood-to-wood joints, Eurocode 5[17] suggests:

$$K_{\text{ser}} = \frac{\rho_m^{1.5} \cdot d}{23} \tag{4.6}$$

where:

- ρ_m is the mean timber density in kg/m^3.
- d is the dowel diameter in mm.

Jockwer and Jorissen [24] conducted an extensive investigation into the origins of the serviceability slip modulus k_{ser} in Eurocode 5, attributing much of the foundational work to Ehlbeck and Larsen [14].

Although commonly referenced simply as Ehlbeck and Larsen (1993), the underlying research actually appears in a series of CIB-W18 (Working Commission W18—Timber Structures) conference papers from the early 1990s [15, 13, 14], with the pivotal connection-stiffness investigations presented at the 26th CIB-W18 meeting in Venice (1993).

In their paper on the stiffness and deformations of connections with dowel-type fasteners, Jockwer and Jorissen [24] note that the Eurocode 5 stiffness equations are based on simplified assumptions and their background is not clearly stated. They further conclude that various standards propose different equations for stiffness, and there considerable differences between experimentally measured connection stiffnesses and those predicted by Eurocode 5.

Impact on Overall Beam Behaviour

The slip modulus directly influences the deflection of the beam and the distribution of the load. Under bending action, the initial deformation under self-weight and low-level loads is influenced by the slip of the connections in the shear planes between the adjacent layers that slide relative to one another with the maximum slip being at the ends and no slip in the centre. And due to slip, which causes changes in the overall cross-section in other words causes non

planarity, the Euler bending theory cannot be directly applied to determine the deformation. Even when the maximum load on the connections is reached , the individual fasteners continue to carry the load and failure often occurs in the individual timber members.

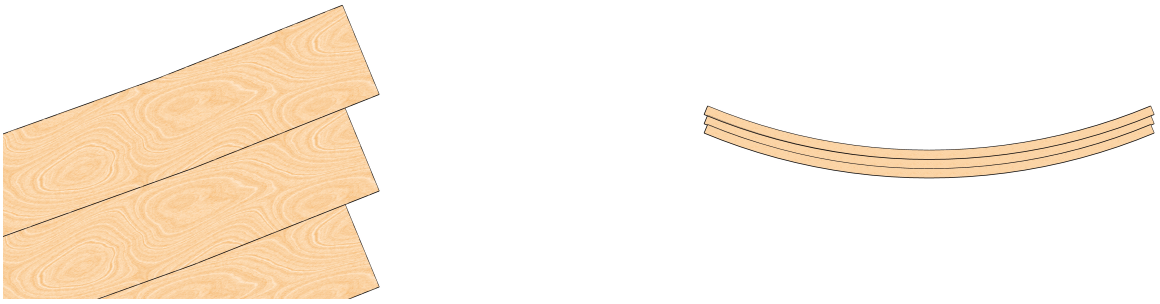

(a) slip between layers **(b)** full scale beam

Figure 4.5: Comparison of slip in mechanically jointed beams

A higher K_{ser} leads to greater composite action, resulting in reduced deflection and increased load-bearing capacity. Conversely, a lower slip modulus increases inter-layer slip, reducing overall stiffness and potentially compromising structural performance [8].

The initial deformation observed at low load levels exhibits a soft behaviour characterized by an initial slip in the connection. This slip depends, among other factors, on the tolerances in the assembly of the connection[24]. According to Dubas (1981)[11], the initial slip is commonly smaller for connections tested in laboratory settings due to the higher precision compared to connections produced in practice. However, with the advent of more precise machinery, such as the elaborate CNCs, the manufacturing precision has improved significantly.

Upon full contact between the components of the connection, the load-deformation behaviour becomes approximately linear. This linear range typically occurs between 10% and 40% of the maximum load and remains below the yield point. At higher load levels, the load-deformation behaviour becomes non-linear and considerably softer if sufficient ductility is available, continuing until the maximum or ultimate load F_{max} or F_{u} is reached. [24]Failure is defined when the load reduces to 80% the force F_{u}. Jockwer [24] provides a detailed analysis of the load-slip deformation.

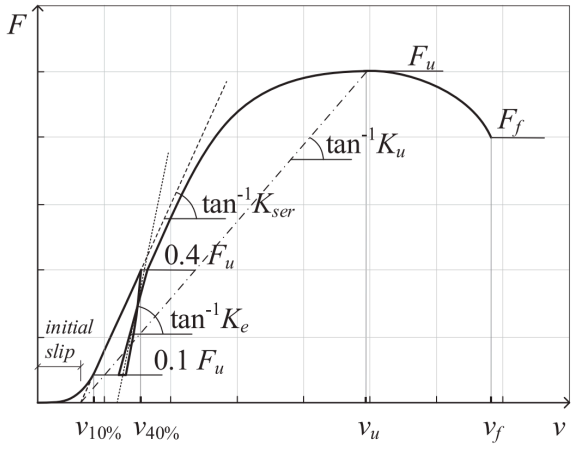

Figure 4.6: slip-moduli for the non-linear load deformation curve of connection

4.2.4. Limitations

The γ-method is based on several key assumptions that simplify the analysis of mechanically jointed beams. These assumptions include linear-elastic behaviour of timber and dowels, perfect contact between layers, uniform load distribution across dowels, and the application of sinusoidal or uniformly distributed loads.

Firstly, it is assumed that both the timber and the dowels exhibit linear-elastic behaviour. This means they respond proportionally to applied loads and return to their original shape upon unloading, without any permanent deformation.

Secondly, the method presumes perfect contact between all layers and neglects gap formation and slip between the layers. This ensures consistent load transfer across the entire beam cross-section. However, in practical applications involving mechanically jointed beams, achieving perfect contact is nearly impossible. Under compressive forces, the layers tend to move upwards, especially at the center of the beam, creating gaps that can affect the load transfer mechanism.

Thirdly, the γ-method assumes that external loads are evenly distributed across all dowels, neglecting localized overstressing. In reality, dowels experience varying stress levels due to factors such as beam geometry and load application points. Dowels located near the center of the beam often carry less load compared to those near the supports or edges, which can lead to uneven stress distribution.

Finally, the analysis considers the beam to be subjected to a sinusoidal or uniformly distributed load. While the method primarily addresses sinusoidal loading conditions, it is also applicable to any uniform load distribution, as noted by Ceccotti [9]. This assumption simplifies the calculation of internal forces and moments but may not accurately represent all real-world loading scenarios.

These assumptions are instrumental in simplifying the complex behavior of mechanically jointed beams for analytical purposes. However, they introduce limitations that must be acknowledged. Deviations from ideal conditions—such as imperfect contact between layers and non-uniform stress distribution in dowels—can lead to discrepancies between theoretical predictions and actual performance. Therefore, when applying the γ-method, it is crucial to consider these limitations and, if necessary, incorporate correction factors or perform additional analyses to account for real-world conditions.

One other limitation of this method is that it does not fully account for non-linearities that may arise due to material plasticity or varying environmental conditions, such as changes in moisture content [27].

In conclusion, these assumptions try to simplifying the complex behaviour of a slip joint for analytical purposes. However, they introduce limitations that must be acknowledged. Deviations from ideal conditions—such as imperfect contact between layers, non-uniform stress distribution in dowels, and unaccounted non-linearities often lead to discrepancies between theoretical predictions and actual performance. Therefore, when applying the γ-method, it is crucial to consider these limitations and, if necessary or possible, incorporate correction factors or perform additional analyses to account for real-world conditions.

Determining the slip modulus experimentally for a four- and two-layered beam requires the ability to reverse engineer the formula using the efficient stiffness as a value we obtain from the experiments and then tweak it to find the kser values.

For the 2 layered beam with different elastic moduli,its expected to have one shear plane but there is a possibility of two values of the Kser owing to the whichever MOE is used even for

similar geometric properties. There is a shift in neutral line but if the neutral axis is assumed to be between the members then the formula for k_{ser} is :

$$k_{\text{ser}} = \frac{\pi^2 s}{L^2} \cdot \frac{E_1 A_1 \cdot E_2 A_2}{E_1 A_1 + E_2 A_2} \left(\frac{1}{\frac{1}{\gamma_{1,2}} - 1} \right). \tag{4.7}$$

For a four-layered beam, there are three shear planes (between layers 1–2, 2–3, and 3–4), and thus three values of k_{ser}. Based on Schelling's method, we assume

$$k_{\text{ser}_{1,2}} = k_{\text{ser}_{3,4}} = k_{\text{ser}_{2,3}}, \tag{4.8}$$

By using the following quantities:

$$(EI)_0 = \sum_{i=1}^{4} E_i \, I_i, \tag{4.9}$$

$$C_1 = E_1 \, A_1 \, a_1^2 + E_4 \, A_4 \, a_4^2, \tag{4.10}$$

$$C_2 = E_2 \, A_2 \, a_2^2 + E_3 \, A_3 \, a_3^2, \tag{4.11}$$

$$\Delta EI = (EI)_{\text{eff}} - (EI)_0. \tag{4.12}$$

To solve for the parameter K, let

$$a = 2 \, \Delta EI, \tag{4.13}$$

$$b = -\frac{2 \, C_1}{3}, \tag{4.14}$$

$$c = -\Big(\Delta EI + \frac{C_1}{3} + C_2 \Big). \tag{4.15}$$

Then K follows from the standard quadratic equation:

$$K = \frac{-b \pm \sqrt{b^2 - 4 \, a \, c}}{2 \, a}. \tag{4.16}$$

Once K is found, compute the shear stiffness values accordingly.

$$k_{\text{ser}_{1,2}} = \frac{\pi^2 \, E_{1,2} \, A_{1,2} \, s}{2 \, l^2 \, (K - 1)} \tag{4.17}$$

$$k_{\text{ser}_{2,3}} = \frac{\pi^2 \, E_{2,3} \, A_{2,3} \, s}{2 \, l^2 \, (K - 1)} \tag{4.18}$$

4.3. Stresses Within The Members And Forces

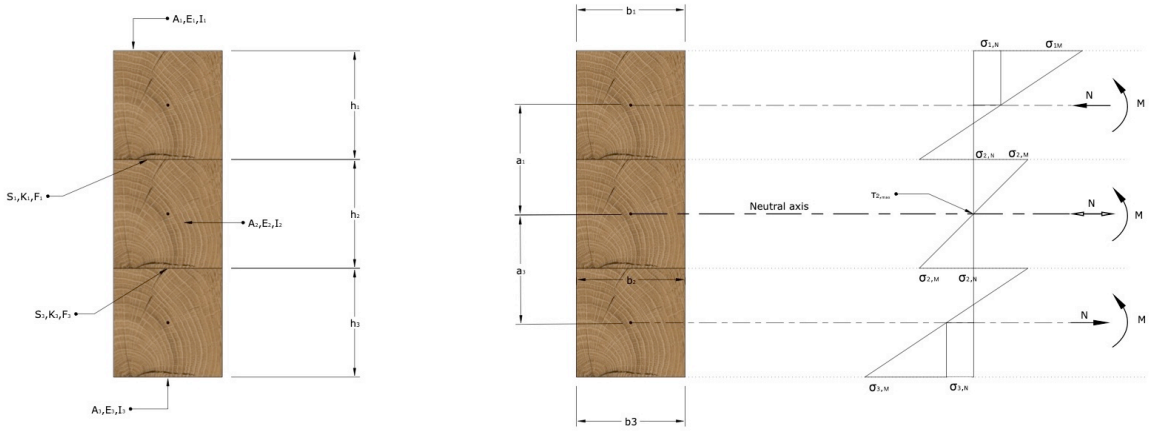

Figure 4.7: Three-layered timber beam illustrating how the axial force N and bending moment M produce normal (tensile/compressive) stresses and shear stresses in each layer, with the neutral axis and stress distributions shown for each segment

The bending stresses in the beams arise from two sources: the bending moment in the beams and the internal forces due to their partial composite action. In the figure above, note that the members—identical in both geometry and modulus of elasticity—have their axes coinciding at the exact center of the middle member; therefore, a_2 is not visible in the diagram. The external moment generated by the applied forces results in the stress distribution shown below. Annex 5 of the Eurocode 5 [17] explains how these stresses are derived, so the derivation will not be repeated in this thesis. For the outer fibers of individual components , the bending stresses are calculated using the external moment as follows:

$$\sigma_{i,M} = \frac{M}{(EI)_{\text{ef}}} E_i \frac{h_i}{2}. \tag{4.19}$$

For calculating normal stresses at the center of gravity of individual components, the γ_i coefficients are added:

$$\sigma_{i,N} = \frac{M}{(EI)_{\text{ef}}} \gamma_i E_i a_i \tag{4.20}$$

The total beam stress is obtained by combining the normal and bending stresses in the outer fiber.

$$\sigma_i = \frac{M}{(EI)_{\text{ef}}} E_i (\gamma_i a_i + \frac{h_i}{2}) \tag{4.21}$$

In this particular model, the maximum shear stress is observed at the neutral axis of the second member.

The shear stress, τ, is given by

$$\tau = \frac{V\,(ES)_{\text{eff}}}{E\,I_{\text{eff}}\,b} \tag{4.22}$$

where

- V is the shear force,
- E is the modulus of elasticity,
- I_{eff} is the effective moment of inertia,
- b is the width at the considered section,
- S is the first moment of area above the neutral axis, defined by

$$S = \int_{y_{NA}}^{h} b(y)\, y\, dy. \tag{4.23}$$

Here, y_{NA} is the position of the neutral axis and h is the total height of the beam.

It is also important to note that the γ -values must be added for all components above or below the neutral axis. In this case γ_2 is 1 , the effective stress (ES_{eff}) will be calculated accordingly.

$$ES_{eff} = \gamma_1 a_1 E_1 A_1 + \gamma_2 \left(\frac{1}{4} h_2\right) \left(\frac{1}{2} E_2 A_2\right) \tag{4.24}$$

The A_2 in this equation is related to the area of the section above the neutral axis of the second member. Consequently, the maximum shear on the neutral axis is determined using an h value that represents the distance from the centre of the middle member to a reference point of contact connecting the adjacent member. This simplifies the equation.

$$\tau_{\max} = \frac{V_{\max}(\gamma_1 E_1 A_1 a_1 + 0.5 E_2 b_2 h^2)}{(EI)_{\text{ef}} b_2} \tag{4.25}$$

The force on the dowels between the shearing planes and s_i as the spacing between the dowels is then given by

$$F_{1,3} = \frac{V_{\max} \cdot \gamma_{1,3} \cdot E_{1,3} \cdot A_{1,3} \cdot a_{1,3} \cdot s_{1,3}}{(EI)_{\text{eff}}} \tag{4.26}$$

The distribution of forces across mechanically jointed beams with multiple fastener rows necessitates consideration of both the spatial arrangement and mechanical engagement of dowels. When multiple rows are implemented, the applied force is distributed proportionally among rows and contributing fasteners (this means that the force on the has to be divided by the number of rows); however, a critical distinction must be made between the nominal quantity of dowels present and the effective number actively participating in load transfer. This effective participation may be governed by the specific loading configuration and resulting internal force distribution.

In four-point bending configurations, the shear force diagram exhibits zero magnitude in the central region between loading points, theoretically resulting in minimal to negligible activation of dowels within this zone. Conversely, three-point bending induces shear forces throughout the entire beam length, potentially mobilizing all dowels along the span. The differential activation patterns of the dowels under varied loading conditions have significant implications for the action of the composite and the effective stiffness of the mechanically joined beams. These hypothesised behavioural differences will be systematically investigated through experimental validation in the subsequent phases of this research study.

4.3.1. Application to Beams with More Than Three Layers

Originally, the γ-method was formulated for beams with up to three layers, since extending it to beams with additional layers would lead to complex and unwieldy calculations. Schelling [56] resolved this issue by generalizing the γ-method to beams composed of more than three layers. His extension involves summing the contribution of each layer while accounting for the cumulative slip across all interfaces. As the number of layers grows, the beam's effective stiffness becomes increasingly sensitive to the slip modulus, making an accurate determination of K_{ser} essential for reliable predictions of the beam's mechanical behaviour.

Building on Mohler's work, Schelling presented calculations for beams with four and five layers, specifying the corresponding γ-values. For a four-layer beam, he gave:

$$K = 1 + \frac{\pi^2 \cdot E \cdot A_1}{l^2 \cdot 2 \cdot \overline{C}} \tag{4.27}$$

where

$$\overline{C} = \frac{k_{\text{ser}}}{s} \tag{4.28}$$

with k_{ser} denoting the slip modulus per connector and s the spacing between connectors (or members).

For a crossection comprised of four parts:

$$\gamma_2 = \gamma_3 = \frac{1}{2K^2 - 1} \tag{4.29}$$

$$\gamma_1 = \gamma_4 = \frac{(2K + 1)\,\gamma_2}{3} \tag{4.30}$$

For five parts:

$$\gamma_2 = \gamma_4 = \frac{K^2 + \frac{K}{2} - \frac{1}{4}}{4K^4 - 3K^2 + \frac{1}{4}} \tag{4.31}$$

$$\gamma_1 = \gamma_5 = K \cdot \gamma_2 \tag{4.32}$$

γ_3 is not required.

For a four-layer beam with the neutral axis at the interface between layers 2 and 3, the effective stiffness is:

$$(EI)\text{eff} = \sum_{i=1}^{4} (E_i I_i) + \sum_{i=1}^{4} \gamma_i E_i A_i a_i^2 \tag{4.33}$$

In a four-layer beam whose neutral axis lies at the interface between layers 2 and 3, the maximum shear stress is:

$$\tau_{\max} = \frac{V_{\max}[\gamma_1 E_1 A_1 a_1 + \gamma_2 E_2 A_2 a_2]}{(EI)_{\text{eff}} \cdot b} \tag{4.34}$$

Thus, the load forces on the fasteners in the joint between the individual components can be determined.

$$F_1 = \frac{V_{\max} \cdot \gamma_1 \cdot E_1 \cdot A_1 \cdot a_1 \cdot s_1}{(EI)_{\text{eff}}} \tag{4.35}$$

$$F_2 = \frac{V_{\max} \cdot \gamma_2 \cdot E_2 \cdot A_2 \cdot a_2 \cdot s_2}{(EI)_{\text{eff}}} \tag{4.36}$$

$$F_3 = \frac{V_{\max} \cdot \gamma_4 \cdot E_4 \cdot A_4 \cdot a_4 \cdot s_4}{(EI)_{\text{eff}}} \tag{4.37}$$

Divide by the number of rows of fasteners if multiple rows are utilised.

4.4. Shear analogy method

In contrast to the Gamma method, which assumes a sign load, the Shear Analogy method proposed by Kreuzinger[30] and Möhler[34]. It can calculate any built-up beam under any loading condition.

The concept is to partition the entire setup of the built-up beam into two components. This approach has been extensively detailed by Scholz [50] under the supervision of Kreuzinger.

In summary, the bending stiffness (EI) of all the components is placed in component A, while the shear stiffness (S^B) of all the components is placed in component B. The shear stiffness encompasses all shear deformations of the components and joint slip of the overall composite beam.

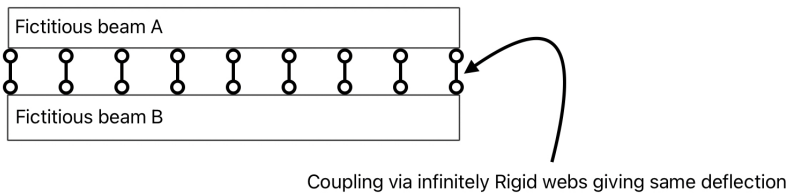

Figure 4.8: Fictitious beam with coupled fictitious components A and B.

The bending stiffness of the A components is calculated as usual. However, the bending stiffness of the B components is the sum of the Steiner parameters (S^B).

$$B^A = \sum_{i=1}^{n} (E_i \cdot I_i) = \sum_{i=1}^{n} \left(E_i \cdot \frac{b_i \cdot d_i^3}{12} \right) \tag{4.38}$$

Where z_i is the distance of the centre of gravity of each part to the centre of gravity of the overall built-up beam.

The bending stiffness of the B components is:

$$B^B = \sum_{i=1}^{n} \left(E_i \cdot A_i \cdot z_{si}^2 \right) = \sum_{i=1}^{n} \left(E_i \cdot b_i \cdot d_i \cdot z_{si}^2 \right) \tag{4.39}$$

We have to remember that there are no shear deformations and the relative displacement of the lamellas due to the semi-rigid connection in part A; these are allocated to part B.

The shear stiffness is recorded with the shear modulus and thickness t of the parts, but the shear stiffness due to the semi-rigidity of the joint is noted by the k_{ser} (Slip modulus) of the fasteners in the joint between the lamellas.

Kreuzinger [30] noted the deformations of the lamellae but also noted that the top and bottom lamellae only had half of their cross-sections applied in the calculation.

The shear stiffness is:

$$S^B = G \cdot A_s + k_{ser} \tag{4.40}$$

Where G is the shear modulus and A_s is the shear area of the lamellas.

The displacement is:

$$u_i = \frac{\tau}{G_i} \cdot d_i = \frac{t}{G_i \cdot b_i} \cdot d_i; \quad u_{i,i+1} = \frac{\tau}{k_{i,i+1}} \approx \frac{t}{k_{i,i+1} \cdot b_i} \tag{4.41}$$

According to H. Kreuzinger's original article B11[31], if only the semi-rigidity of the joint is considered and the individual components themselves do not allow for shear deformations, equation (D7-14) can be simplified as follows:

$$\frac{1}{S^B} = \frac{1}{a^2} \cdot \sum_{i=1}^{n-1} \frac{1}{k_{i,i+1}} \tag{4.42}$$

To calculate the internal forces and moments in fictitious beams A and B, these are coupled to each other via infinitely rigid web members, to ensure they undergo the same deformation along their axis

Deformation due to bending and deformation due to shear are superimposed to obtain the same deflection for the coupled system.

4.5. Failure Modes in Multi-layered Timber Beams

4.5.1. Johansen's Yield Theory

Johansen's yield theory [25] provides a rigorous framework to estimate the maximum lateral load capacity of the dowelled connections considering potential failure modes such as the yield of the dowels and the embedment of wood. According to this theory, the ultimate load bearing capacity (F_v) is governed by one of several yield modes, which may include plastic deformations in the dowel or local crushing in the wood.

In the case of multilayered timber beams, shear failure can manifest itself through various mechanisms.

Dowel Yielding : Plastic deformation of the dowel.

Wood Crushing : Failure arising from embedding stresses that exceed the strength of the wood.

Inter-layer Slip : Excess slip between layers leads to a reduction in composite action.

Splitting : Fracture of the wood due to tension perpendicular to the grain.

Hilson [21] describes the use of mechanical models to determine characteristic load-bearing capacities based on joint geometry and material properties. The design equations in EC 5 [17]stem from Johansen's work [25], establishing that failure occurs when embedding strength limits are reached or plastic hinges develop in the fastener.

Extensive research [33, 5, 20] validates Johansen's yield theory in timber connections, showing strong correlation between theory and performance when frictional effects and tensile forces remain negligible [21].

As shown in Article E1 (equations (E1-1) to (E1-4)), determining joint capacity requires *embedment strength* f_h and *yield moment* M_y, along with geometric parameters like timber thickness $t_1/2$ and fastener diameter d.

The failure modes can happen at any joint as allocated by the the red dotes and can be governed by any possible failure. Möhler did conclude that failure could be any mechanism but to achieve ductile failure , failure mode f was desirable as shown in the diagram below;

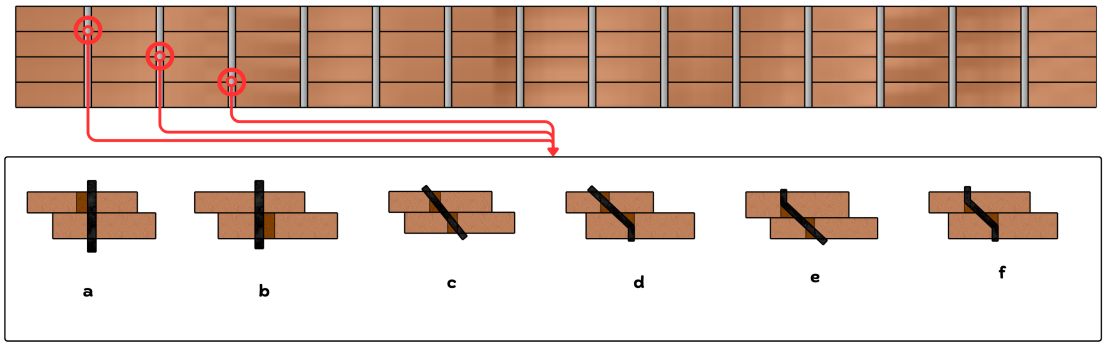

Figure 4.9: Illustration of the classic Johansen failure modes (a–f) for wood-wood connections, showing how dowels and wood elements can yield under different loading configurations

The equations that govern them become the failure modes described below whilst the min value of $F_{v,Rk}$

$$F_{v,Rk} = \min\big(F_{v,Rk,(a)},\, F_{v,Rk,(b)},\, F_{v,Rk,(c)},\, F_{v,Rk,(d)},\, F_{v,Rk,(e)},\, F_{v,Rk,(f)}\big). \tag{4.43}$$

Failure Mode (a): Embedment in the Side Member Only . This mode represents a case where the failure is governed solely by the crushing (embedment) of one of the members (the outer lamella) under the fastener. No plastic hinge forms in the fastener; the dowel simply penetrates until the local wood strength is exceeded. The characteristic load-carrying capacity is given by:

$$F_{v,Rk,(a)} = f_{h,1,k}\, d\, t_1 \tag{4.44}$$

where $f_{h,1,k}$ is the characteristic embedment strength of the side member, t_1 its thickness, d the fastener diameter

Failure Mode (b): Embedment in the Main Member Only . In this mode, the failure occurs because the main member (inner lamella) reaches its embedment capacity while the side member remains within its limit. The dowel penetrates preferentially into the main member. The governing capacity is expressed as:

$$F_{v,Rk,(b)} = f_{h,2,k}\, d\, t_2, \tag{4.45}$$

with $f_{h,2,k}$ and t_2 being the characteristic embedment strength and thickness of the inner member, respectively.

Failure Mode (c): Single Plastic Hinge Formation at the Side-Member End . This mode is characterized by the side member reaching its embedment limit while the fastener begins to yield by forming a plastic hinge on the side-member end. The failure is due to a combination of local crushing in the side member and bending of the fastener. The load-carrying capacity is given by:

$$F_{v,Rk,(c)} = \frac{f_{h,1,k}\, t\, d}{1+\beta}\left[\sqrt{\beta(-1+6\beta+\beta^2)}\right] \tag{4.46}$$

where $M_{y,Rk}$ is the characteristic yield moment of the fastener and β is

$$\beta = \frac{f_{h,2,k}\, t_2}{f_{h,1,k}\, t_1} \tag{4.47}$$

Failure Mode (d): Single Plastic Hinge Formation at the Main-Member End . Analogously to Mode (c), failure can also occur with a plastic hinge forming at the main-member end. In this mode the main member controls the embedment while the fastener yields by bending. The resulting capacity is:

$$F_{v,Rk,(d)} = 1,05\frac{f_{h,1,k} t d}{2+\beta}\left[\sqrt{2\beta(1+\beta)+\frac{4\beta(2+\beta)M_{y,Rk}}{f_{h,1,k} d\, t^2}}-\beta\right] \tag{4.48}$$

Failure Mode (e): Double Plastic Hinge Formation Favouring the Side-Member End . This failure mode involves the formation of two plastic hinges in the fastener with both hinges oriented toward the side member. The combined action of full embedment of the side member and significant plastic rotation in the fastener governs the capacity, which is given by:

$$F_{v,Rk,(e)} = 1,05\frac{f_{h,1,k} t d}{1+2\beta}\left[\sqrt{2\beta^2(1+\beta)+\frac{4\beta(1+2\beta)M_{y,Rk}}{f_{h,1,k} d\, t^2}}-\beta\right]. \tag{4.49}$$

Failure Mode (f): Double Plastic Hinge Formation in favour of the Main-Member End . Here, two plastic hinges form in the fastener, both on the main-member side. The failure mechanism is driven by the embedment in the main member coupled with ductile yielding of the fastener. The load capacity is expressed as:

$$F_{v,Rk,(f)} = 1,15\sqrt{\frac{2\beta}{1+\beta}}\sqrt{2M_{y,Rk} f_{h,1,k} d}. \tag{4.50}$$

4.5.2. Embedment Strength and Stiffness

Embedment strength ($f_{h,\alpha}$) refers to the capacity of the wood surrounding a dowel to resist deformation under load applied at an angle α to the grain [42]. It is critical for assessing the load-bearing capacity of dowelled connections, dictating joint strength and stability.

Embedment strength is influenced by; Wood Density: Higher density increases embedment strength. Dowel Diameter: Larger diameters distribute load over a greater area. Moisture Content: Increased moisture can reduce embedment strength. Load Orientation: Embedment strength varies with angle to the grain.

4.5.3. Relationship to Wood Density and Dowel Diameter

The embedment strength can be calculated using the formula [17]:

$$f_{h,0} = 0.082\,(1 - 0.01d)\,\rho_k \tag{4.51}$$

Where:

- $f_{h,0}$ is the embedment strength parallel to the grain (N/mm²).
- d is the dowel diameter (mm).
- ρ_k is the characteristic density of the wood (kg / m3).

5

RESEARCH METHOD

In this section, the research method for investigating the parameters that affect the strength and stiffness of dowelled multilayered azobe beams will be discussed. This research endeavour will evaluate the effective stiffness of the mechanical properties of these beams, with a focus on their strength and stiffness. To achieve this, a combination of laboratory assessments and analytical solutions is recommended following the European standard EN 1995 [17].

5.1. BENDING TESTS

To assess the parameters that affect the stiffness and the bending stiffness of the multi-layered dowelled beams, a laboratory test will be done. The considered parameters are dowel hole size, cross-section layer sizes.

The Nen-EN 408 ([43]) is used as a guide because it describes the experiments used in structural timber and those on glulam timber which closely resemble the setup of mechanically jointed beams as a combination of timber with individual structural members and a set of constructed joints but there was some deviation from it.

The primary objective of these tests was to characterize the structural behaviour of mechanically jointed azobe beams with varying configurations. By systematically altering the number and thickness of beam layers while maintaining constant overall dimensions, the study aimed to quantify variations in effective stiffness and identify failure mechanisms.

A four-point bending test, as recommended by [43], is used to measure the modulus of elasticity (MOE) and the effective stiffness of the built-up beams. The primary advantage of this test lies in the distribution of maximum stress over a broader region between the two loading points, leaving a pure bending region from which the local MOE can be used. This results in a larger area under uniform stress, significantly reducing the probability of premature failure caused by localised defects. Consequently, it offers a more accurate assessment of the flexural strength of the material.

Additionally, three-point bending tests were conducted after the dowel assembly to compare the stiffness results of the two testing approaches. Although the three-point bending test increases shear activation in the dowels, potentially causing stress concentrations and premature failure, the four-point test setup, despite its complexity, provided more comprehensive flexural behaviour data.

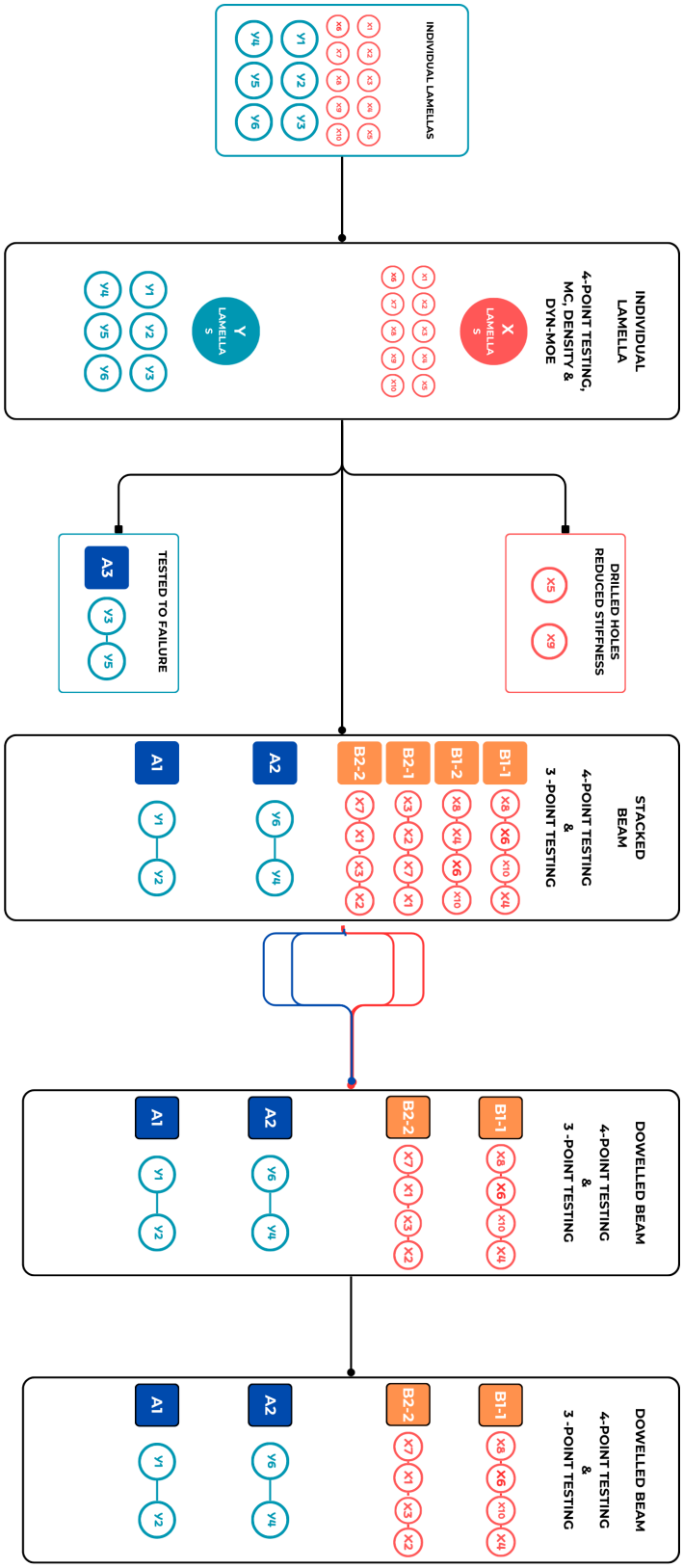

Figure 5.1: Experimental setup flow chart

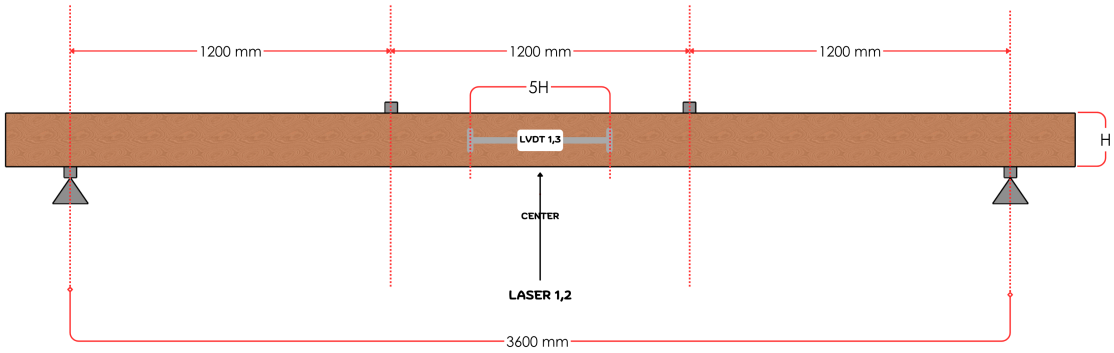

Figure 5.2: Experimental setup of 4 point bending for the individual lamellas, showing the positions of LVDT 1 and 3 either side of the midpoint of the lamella and the deflection laser measurement points located at the bottom.

5.2. EXPERIMENTAL PLAN

The experimental setup consisted of two steps. Initial testing and final testing

Initial Testing :

The initial testing was conducted in the Stevin Laboratory at TU Delft. Wijma Hupkes provided six samples of 140 mm in height and ten samples of 70 mm in height. All samples were approximately 4000 mm long and 140 mm wide. All lamellas underwent planing to ensure dimensional consistency and end waxing to prevent moisture exchange, with unique identifiers assigned (Y1 to Y6 for 140 mm lamellas, X1 to X10 for 70 mm lamellas). Each sample was subjected to a four-point bending test with a specific force to induce a certain deformation, from which the MOE could be calculated.

After the calculations, four samples of 140 mm height and eight samples of 70 mm height were selected based on their mechanical properties. Two samples of each size remained unused for control purposes.

Designing the Test Specimens :

The experimental plan included the following beam configurations:

Two-Layer Beams (Type A) consisting of two vertically stacked lamellas, each measuring 140 mm in height, creating a total beam height of 280 mm. Two beams are constructed in this configuration.

Four-Layer Beams (Type B) are built from four vertically stacked lamellas, each with a height of 70 mm, also achieving a total beam height of 280 mm. Two beams are similarly be assembled for this configuration.

Lamella specimens supplied by Wijma Hupkes were standardized in dimensions to widths of 140 mm and lengths approximately 4 m. Specifically, six lamellas of 140 mm height and ten lamellas of 70 mm height were prepared.

(a) Beam A layout with two layers of 140 mm each

(b) Beam B layout with four layers of 70 mm each

Figure 5.3: Comparison of Beam A and Beam B configurations

Determination of flexural MOE

Following the four-point bending procedure outlined in [43] and illustrated in the figure below, the global and local modulus of elasticity is calculated using the provided equation. The four-point bending test configuration involved equal spacing between loading and support points, specifically a distance of 1200 mm between the loading points and the supports. The total length of the tested beams was 3600 mm.

The standard outlined in NEN 408 specifies using a beam length equal to 18 times the beam height (18h) for testing. However, applying this criterion without adjustment would result in lamellas that are thin for our purposes. Additionally the available lamellas provided for the study were limited to about 4000 mm long. Under these constraints, utilising the 18h length would result in lamellas of a height of about 50mm, which was insufficient to capture the structural behaviour need to observe.

For deflection measurements, lasers positioned beneath the beam were adequately precise. Additionally, Linear Variable Differential Transformers (LVDTs) were installed on both sides of the beam within an apparatus designed with a gauge length equal to five times the beam's cross-sectional height, enabling the determination of the local modulus of elasticity.

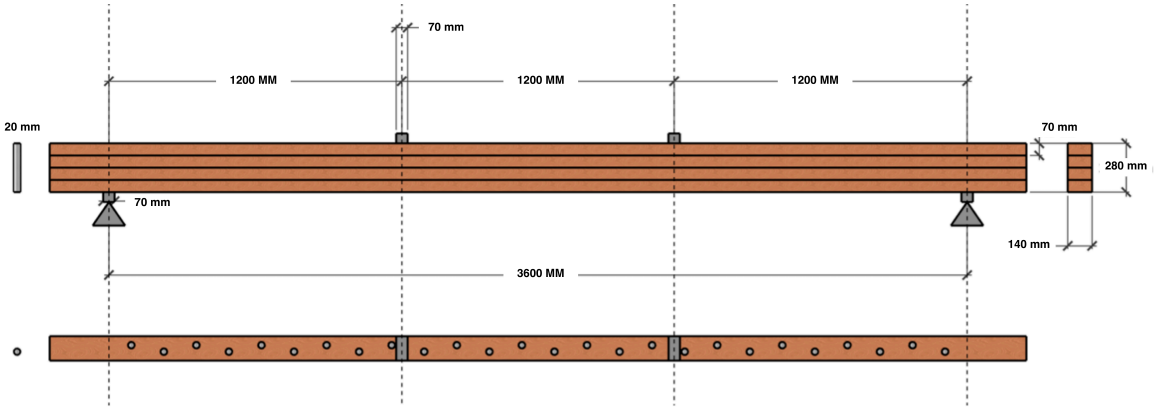

Figure 5.4: Four-point bending test setup as specified in EN 408 [43].

$$E_{\text{global}} = \frac{\frac{\Delta P}{\Delta w}\, a\, \left(3L^2 - 4a^2\right)}{48\, I} \tag{5.1}$$

where ;

- $\frac{\Delta P}{\Delta w}$: The slope of the load-deflection curve, calculated as the incremental change in applied load (ΔP) divided by the corresponding incremental change in deflection (Δw).
- a: The distance between the two loading points in the four-point bending test, which defines the constant moment region.
- L: The total span length of the beam, which is the distance between the two outer supports.
- I: The moment of inertia of the beam's cross-section. For a rectangular cross-section:

$$I = \frac{b \cdot h^3}{12}$$

where b is the width and h is the height of the beam.

As for the measurements with the lvdts and Dic the following figure shows distances of the measurement tools used

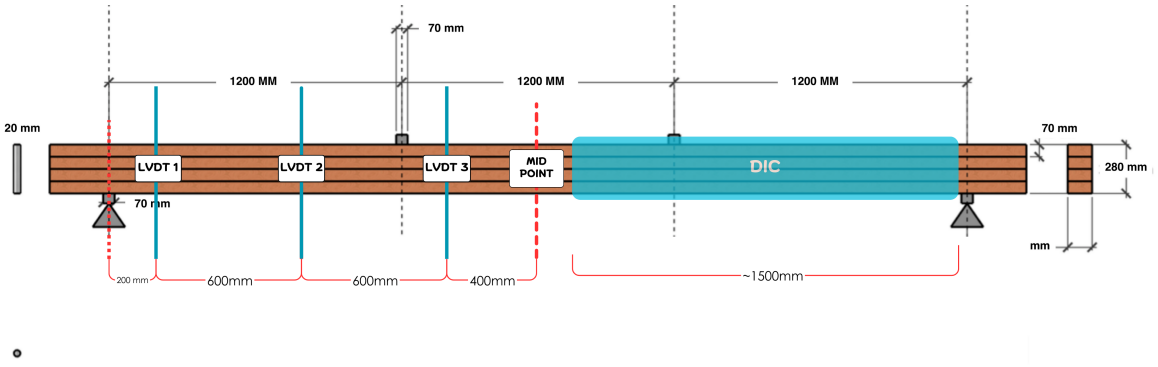

Figure 5.5: Schematic illustration of the dowelled beam assembly showing the positioning of the LVDT sensors (LVDT1, LVDT2) and the Digital Image Correlation (DIC) measurement region, along with key dimensions and reference points.LVDT3 not used in the 4 point bending

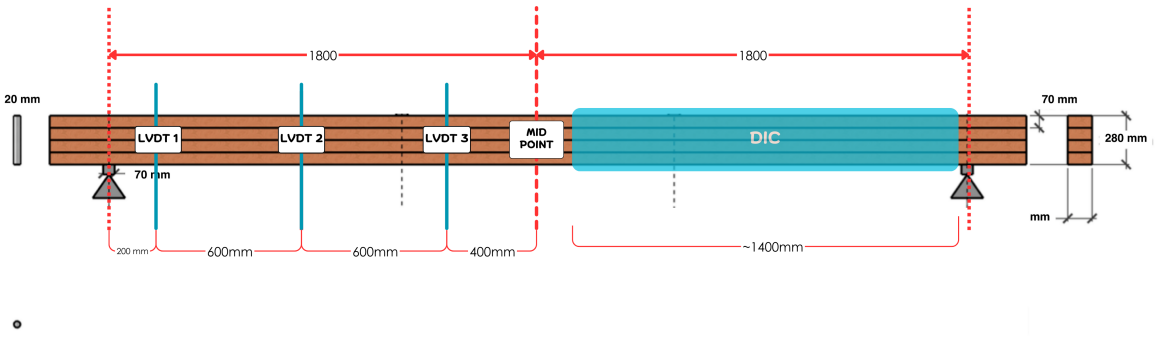

Figure 5.6: Schematic illustration of the dowelled beam assembly in 3point bending showing the positioning of the LVDT sensors (LVDT1, LVDT2, LVDT3) and the Digital Image Correlation (DIC) measurement region, along with key dimensions and reference points.

To find the Strength class of the individual azobe members, it would be important to classify the members, and this is done by determining the characteristic density values and mean

local MOE. There are correlations done by Geert [45] that correlate these values to the non-destructive methods of the dynamic MOE(MOE_{dyn}).

The MOE_{dyn} is found by supporting a timber piece 0.224 of the Length at either end and then using a hammer to impact one end while an accelerometer is placed at the other. The induced vibrational frequencies are recorded as a first and second frequencies. the second frequency should be twice the first and using the formula below:

$$E_{dyn} = 4\rho L^2 f^2 \tag{5.2}$$

Where:

ρ = density (kg/m^3)
L = specimen length (m)
f = fundamental longitudinal frequency (Hz)

The initial tests included measuring the dynamic modulus of elasticity (MOE) using a timber grading device (e.g., ultrasonic tester), which also provided preliminary density information. Subsequently, wet density measurements were taken by individually weighing the lamellas and determining their volumes. Post-testing, dry density and moisture content were evaluated from small cross-sectional samples extracted and oven-dried, providing data for comparative analysis with dynamic MOE values.

Using the values of characteristic density and local MOE to find out the MOE of the individual pieces and thus their correspondence in the strength class tables in the Eurocode 5 [1]. This can be used to non destructively grade the timer lamellas and estimate their strength.

The dimensions of the timber test pieces were determined based on the limitations of laboratory equipment and the requirement to achieve structural failure during testing. Beams with a cross-sectional dimension of 140 mm by 70 mm and a span length of 3.6 m between supports were used.

The moisture content of the timber was determined according to EN 13183 [38]. Samples were taken by cutting a full cross-sectional segment free from knots and resin pockets approximately 30 cm from either end or from the center of the structural beams after completion of the bending tests.

Density measurements were performed by individually weighing each lamella using electronic scales and measuring their dimensions at three distinct points to accurately determine volume. Density was calculated as the ratio of mass to volume. Although full conditioning was not conducted, the lamellas were left stationary in the same environment for over three weeks prior to weighing, ensuring a stable moisture equilibrium was reached before measurements.

Determining Optimal Dowel Placement for Enhanced Structural Capacity

The determination of minimum starting distances, along with specific edge and end distances and spacings for dowels, is in practice for maximising structural capacity. Ensuring these minimum distances are observed is fundamental to mitigating brittle failure modes, such as splitting, thereby facilitating more ductile behaviour in the materials used.

The critical parameters influencing these distances include the width and length of the member, fastener penetration depth, the susceptibility to splitting parallel to the grain, and the

overall member thickness. As outlined in the existing standards [1], these parameters are typically established through rigorous experimental investigations. The results of these studies are often consolidated into tables that provide clear guidelines based on empirical data and comprehensive experimental analysis.

These guidelines are essential for designing connections that are both safe and efficient, ensuring that the structural elements behave as intended under load conditions without premature failure

Table 5.1: Minimum spacings and edge and end distances for dowels[1]

Spacing and edge/end distances (see Figure 8.7)	**Angle**	**Minimum spacing or edge/end distance**
a_1 (parallel to grain)	$0° \leq \alpha \leq 360°$	$(3 + 2\cos\alpha)d$
a_2 (perpendicular to grain)	$0° \leq \alpha \leq 360°$	$3d$
a_3 (loaded end)	$-90° \leq \alpha \leq 90°$	$\max(7d; 80 \text{ mm})$
a_3 (unloaded end)	$90° < \alpha \leq 150°$	$\max(a_3 \cdot \sin\alpha; 3d)$
	$150° < \alpha \leq 210°$	$3d$
	$210° < \alpha \leq 270°$	$\max(a_3 \cdot \sin\alpha; 3d)$
a_4 (loaded edge)	$0° \leq \alpha \leq 180°$	$\max\{(2 + 2\sin\alpha)d, 3d\}$
a_4 (unloaded edge)	$180° < \alpha \leq 360°$	$3d$

The minimum loaded end distance is determined by the greater of either 7d or 80 mm. Given dowel diameters of 20 mm, the calculation yields a maximum of 140 mm adopted as the minimum edge distance. Consequently, an edge distance of 200 mm is ultimately selected to copy the company Hupkes Wijma's manufacturing style for this size of beams

The A configuration utilises dowels measuring 20 mm in diameter and of s355 steel grade and is dimensioned at 140 by 140 mm while the B configuration is dimensioned at 140 by 70mm.

Should the analysis indicate the feasibility of using drill sizes of 12 mm or 16 mm, these options should be revisited and evaluated for potential inclusion in the experimental setup.

Table 5.2: Experimental Design Parameters

Parameter	Value
Minimum Loaded End Distance	140 mm (greater of 7d or 80 mm)
Edge Distance	200 mm
Original Dimensions of wood cross sections	140 mm × 140 mm
Scaled Down Dimensions of wood cross sections	140 mm × 70 mm
Original Dowel Diameter	20 mm
Scaled Down Dowel Diameter	10 mm – 12 mm
Alternative Drill Sizes (for evaluation)	12 mm, 16 mm

Bolts

On top of transmitting tension, bolts have an increased factor of adding tension to hold the lamellas in place. It is in practice to replace certain dowels with bolts to ensure reduction of the gap between the wood members. As recommended by Sandhaas[47], at least two dowels should be replaced with bolts at either end. In this particular design, no bolts are utilised to minimise any external influences other than those exerted by the dowels.

The table below presents the minimum distance required in cases where bolts are added.

Table 5.3: Minimum bolt distances and spacings, d = bolt diameter in mm, $0° \leq \alpha \leq 90°$ = angle between force and grain directions. See also EN 1995-1-1:2010 Table 8.4.

Distances and spacings	Angle	Minimum values
Spacing a_1 (parallel to the grain)	-	$(4 + \cos\alpha) \cdot d$
Spacing a_2 (perpendicular to the grain)	-	$4 \cdot d$
Distance $a_{3,t}$ (loaded end)	-	$\max(7 \cdot d; 80 \text{ mm})$
Distance $a_{3,c}$ (unloaded end)	$\alpha < 30°$ $30° \leq \alpha \leq 90°$	$4 \cdot d$ $(1 + 6 \cdot \sin\alpha) \cdot d$
Distance $a_{4,t}$ (loaded edge)	-	$\max\{(2 + 2 \cdot \sin\alpha) \cdot d, 3 \cdot d\}$
Distance $a_{4,c}$ (unloaded edge)	-	$3 \cdot d$

Using the specifications given, the bolt distance at the loaded end, $a_{3,t}$, is calculated to be 140 mm. However, the minimum spacing with $\alpha = 90°$ is $5d$, which equates to 100 mm for the dowels. A distance of 200 mm will be maintained as it is with the dowels. The minimum distance from the both edges, $3d$, is 60 mm, and a distance of 100 mm has been chosen, which is sufficient to meet the requirements.

5.2.1. Testing Arrangement For Bending Strength In Parallel To Grain

The test piece shall be simply supported at the required span of 6m. and it shall be symmetrically loaded in bending at two points over a span 18x of its depth The maximum distance between the loading points will not be more than 6H±75cm for the 5 layered beam and 6H±60cm for the 4 layered beam according to the [43] Lateral restraint shall be placed as necessary to prevent lateral (torsional) buckling.

The bending strength is determined by:

$$f_m = \frac{3Fa}{bh^2}$$

F - load, in newtons

a - distance between a loading position and the nearest support, mm;

b - width of cross section in a bending test, or the smaller dimension of the cross section, mm

h - depth of cross section in bending test; mm

Preliminary Test Results for All Lamellae under 4-PBT

In the preliminary testing, individual lamellae were subjected to four-point bending tests (4-PBT). Based on an allowable bending stress of 28 N/mm^2, the corresponding force and deformations were calculated. The objective was to maintain the same stress in each lamella by allowing them to slide over each other without shear interaction; in such a scenario, the force can be scaled accordingly (doubled, quadrupled, etc.), while the theoretical deformation remains constant.

Lamellas with Drilled Holes: Preliminary 4-PBT The additional lamellae from the batch were first drilled at 400mm intervals (resulting in 9 holes) and later at 200mm intervals (resulting in 17 holes). After the initial test, the samples were re-tested following the drilling of 17 holes to determine if any reduction in bending stiffness occurred. The same testing procedures were used in both cases, and identical deflections were achieved.

The following tables present the initial test data for the lamellae and beams, including dimensions, forces, deflections, and loading speeds of the experiments.

Table 5.4: Preliminary test results for all lamellae under 4-PBT (within three minutes).

Sample ID	Type	Quantity	Height (mm)	Force (N)	Loading Speed (mm/s)	Expected Deflection (mm)	LVDT Placement Length (mm)
Y1, Y2, …	Lamella	6	140	19,208	0.18	32.45	700
X1, X2, …	Lamella	10	70	4,802	0.36	64.90	350

For each lamella, the Y type was to reach 19 kN, while the X type which has half the cross-sectional height of the Y lamella was required to reach 5 kN in order to remain in the elastic range.

Unjointed/ Stacked Beam Assembly 4-PBT for MOE

For the stacked (or unjointed) beams, where the cross-sectional width remains uniform at 280 mm, the Y beams were arranged in two lamellae (stacked on top of one another) and the X

beams in four lamellae. The force for the Y configuration was doubled to 38kN, while the force for the X configuration was quadrupled to 19kN. This adjustment ensures that the deflection and, therefore, the stress in each individual lamella remain consistent, with the underlying assumption that no composite action occurs via friction to redistribute the forces. the table below summarizes the test.

Table 5.5: Unjointed beam assembly (4-PBT) for MOE testing.

Beam ID	**Type**	**Layers**	**Heights (mm)**	**Force (N)**	**Speed (mm/s)**	**Deflection (mm)**
A1	Type A	2	140	38,416	0.18	32.45
A2	Type A	2	140	38,416	0.18	32.45
B1	Type B	4	70	19,208	0.36	64.90
B2	Type B	4	70	19,208	0.36	64.90

The testing procedure is discussed and expanded upon in the subsequent section.

6

RESULTS AND ANALYSIS

This section offers an overview of the testing outcomes. It examines the results in a way, discussing the testing procedures and the insights gained throughout the process. the results are split into two sections, results from the individual lamellas and results from the stacked beams without assembly and then results from the mechanically jointed beam tests. A final comparison with theory calculations then is discussed.

6.1. Moisture content, Density and mechanical properties

Moisture content in the pieces was determined after 3 weeks of the beams placed in the laboratory environment. control time in the . The testing wasn't done to the dot of the EN 13183 [38]. A piece was cut a distance 20 mm from the either waxed end of the lamella after cutting 10mm of the waxed end. all lamellas were tested the same way.

The cut piece was immediately measured and then placed in the oven. Once the weight was stable, that is, the moisture content had a difference of 0.1% between two consecutive weighings with a $>$ 2 hour interval, then the moisture content was determined as shown in Equation 6.1 below:

$$\mathrm{MC}(\%) = \frac{\text{Wet Weight} - \text{dry Weight}}{\text{dry Weight}} \times 100 \tag{6.1}$$

The average moisture content was then plotted. It can be noted that the average moisture content of Y1, Y2, Y4 and Y6 was higher than that of the X beams by more than 9% to a maximum of 18.6% water content. This is to show that the larger beams store more water on average than their counterparts.

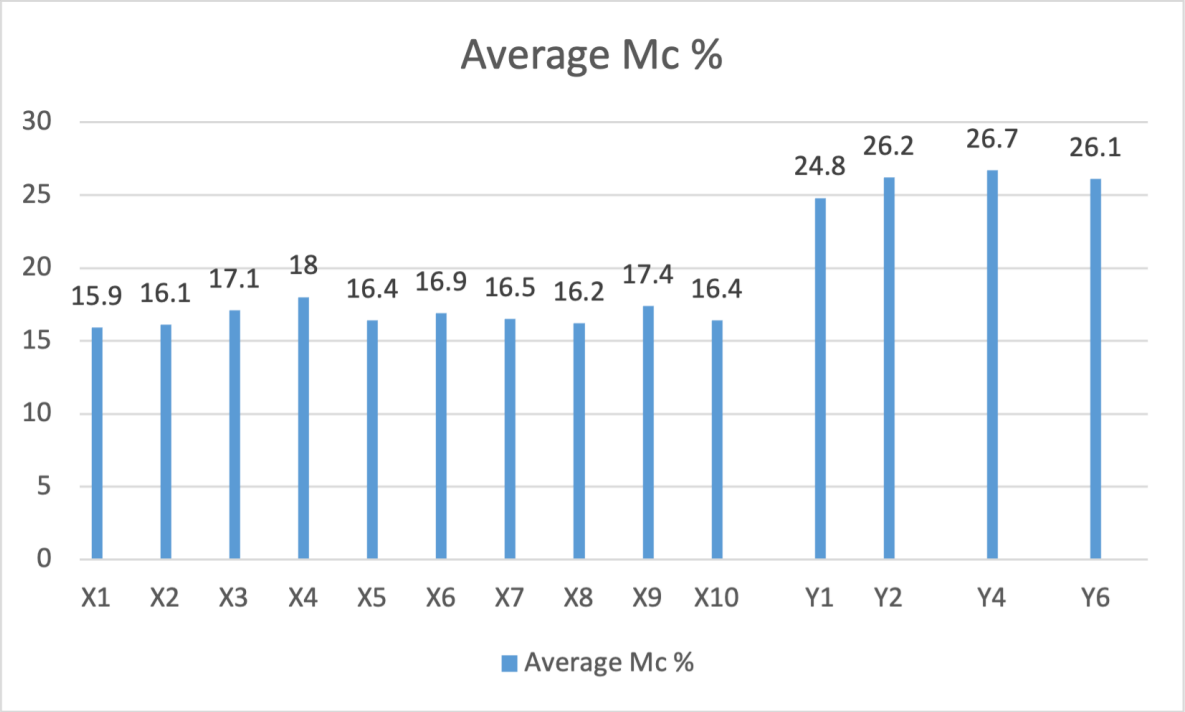

Figure 6.1: moisture content of the pieces

6.1.1. Density Adjustment for Reference Moisture Content (12%)

Material properties are typically referenced at 12% moisture content (MC) to ensure standardized design calculations. This necessitates the adjustment of density measurements taken at different moisture contents to this reference value. The adjustment process must account for both dimensional changes due to wood-water interactions and mass variations due to moisture content differences. This enables us to grade the timber sufficiently.

The density at any moisture content is defined as:

$$\rho_{mc} = \frac{V_{m.c}}{G_{m.c}} \tag{6.2}$$

where $G_{m.c}$ is mass and $V_{m.c}$ is volume at that moisture content.

Changes in moisture content affect both the mass and volume of timber. According to [45] The volume change (ΔV) is described by:

$$\Delta V = \beta v * (mc_{measured} - mc_{target}) \tag{6.3}$$

where βv is the volumetric shrinkage coefficient, combining radial (βr), tangential (βt), and longitudinal (βl) shrinkage:

$$\beta v = \beta r + \beta t + \beta l - 100 \beta l \beta h \tag{6.4}$$

The density adjustment equations differ based on the Fiber Saturation Point (FSP):

For MC $\leq$ 25% (Below FSP):

$$\rho_{target,mc} = \rho_{mc,measured} \frac{(1 + 0.01 * \beta v * (mc_{measured} - mc_{target}))}{(1 + 0.01 * (mc_{measured} - mc_{target}))} \tag{6.5}$$

For MC > 25% (Above FSP):

$$\rho_{target,mc} = \rho_{mc,measured} \frac{(1 + 0.01 * \beta_v * (mc_{FSP} - mc_{target}))}{(1 + 0.01 * (mc_{measured} - mc_{target}))} \tag{6.6}$$

For practical applications between 12% and 25% MC, an average value for $\beta v \approx 0.5\%$ per percent moisture content change can be used as a general approximation. This standardisation enables consistent comparison of material properties in different specimens of timber and environmental conditions. And a FSP of 25% is used.

Table 6.1: Adjusted Density values to MC 12%

Lamella Id	Density	MC%	Density at 12%MC
X1	1,115	15.9	1073.4
X2	1,074	16.1	1031.9
X3	1,163	17.1	1106.8
X4	1,153	18.0	1088.1
X5	1,160	16.4	1111.4
X6	1,139	16.9	1086.1
X7	1,109	16.5	1061.5
X8	1,090	16.2	1046.3
X9	1,097	17.4	1041.1
X10	1,081	16.4	1035.7
Y1	1,194	24.8	1059.2
Y2	1,185	26.2	1038.3
Y3	1,182	26.0	1038.0
Y4	1,188	26.7	1036.4
Y5	1,217	26.0	1068.7
Y6	1,209	26.1	1060.3

X Series

Average Original Density: 1118.1 kg/m^3
Average MC: 16.7%
Average Adjusted Density: 1068.2 kg/m^3
Range of Adjusted Density: 1031.9 – 1111.4 kg/m^3

Y Series

Average Original Density: 1195.8 kg/m^3
Average MC: 26.0%
Average Adjusted Density: 1050.1 kg/m^3
Range of Adjusted Density: 1036.4 – 1068.7 kg/m^3

6.2. Moisture Content Adjustment of Elastic Properties

6.2.1. Adjustment Methodology

To standardise comparisons between samples, all modulus of elasticity (MOE) values were adjusted to a reference moisture content of 12% using the adjustment equation found in a dissertation of Geert Ravenshorst in 2015.[45]

$$\mathrm{MOE}_{12\%} = \mathrm{MOE}_{mc} / \left(1 - k_{mc} \frac{\min(m.c.; 25.0) - 12}{13}\right) \tag{6.7}$$

Where:

- $\mathrm{MOE}_{12\%}$ is the adjusted modulus of elasticity at 12% moisture content
- MOE_{mc} is the measured modulus of elasticity at the test moisture content $m.c.$
- k_{mc} is the adjustment factor, with a value of 0.13 for samples
- $m.c.$ is the moisture content at testing (%)
- $\min(m.c.; 25.0)$ caps the maximum moisture content at 25.0%

This adjustment is necessary as moisture content significantly affects the elastic properties of wood materials. The k_{mc} value of 0.13 is therefore used as a conservative approach for adjusting dynamic, local, and MOE_{Global} values.

6.2.2. Results of MOE Adjustment

Table 6.2 shows the original and adjusted MOE values for all specimens. The adjustment reveals the differences in elastic properties when standardized to 12% moisture content.

Table 6.2: Original and Moisture-Adjusted MOE Values (12% Reference)

Lamella ID	MC (%)	DYN MOE Ratio	DYN MOE (MPa)	Adj. DYN MOE (MPa)	Global MOE (MPa)	Adj. Global MOE (MPa)	Local MOE (MPa)	Adj. Local MOE (MPa)
X1	15.9	1.13	17 400	19 700	14 400	16 300	16 100	18 200
X2	16.1	1.14	18 500	21 100	15 500	17 600	15 900	18 100
X3	17.1	1.17	22 000	25 800	19 200	22 500	20 200	23 700
X4	18.0	1.20	20 700	24 900	18 100	21 800	19 100	23 000
X5	16.4	1.15	19 300	22 100	16 000	18 400	17 500	20 100
X6	16.9	1.16	18 200	21 200	15 400	17 900	16 600	19 300
X7	16.5	1.15	18 100	20 800	15 300	17 600	15 800	18 200
X8	16.2	1.14	21 000	24 000	15 700	17 900	16 800	19 200
X9	17.4	1.18	19 000	22 400	15 700	18 500	14 700	17 400
X10	16.4	1.15	17 300	19 800	15 000	17 200	15 100	17 300
Y1	24.8	1.40	17 500	24 600	15 200	21 400	17 400	24 400
Y2	26.2	1.42	18 500	26 200	16 100	22 800	16 800	23 800
Y3	26.0	1.42	18 500	26 200	15 500	22 000	14 600	20 700
Y4	26.7	1.42	17 900	25 400	16 000	22 700	17 600	24 900
Y5	26.0	1.42	18 300	25 900	15 700	22 300	15 700	22 300
Y6	26.1	1.42	17 400	24 700	15 200	21 500	15 600	22 100

The true MOE values are much higher after adjustment to the 12 % moisture content, as shown in the table above. The X samples, with moisture contents ranging from 15.9% to 18.0%, show

moderate increases in MOE values when standardized to 12% MC, with DYN MOE Ratios ranging from 1.13 to 1.20.

For the Y samples, which have significantly higher moisture contents (24.8% to 26.7%), the DYN MOE Ratios are more substantial, ranging from 1.40 to 1.42. Due to the capping of moisture content at 25.0% in the adjustment equation, samples with moisture contents exceeding 25% have similar DYN MOE Ratios.

The relationship between the different MOE measurement methods remains consistent after adjustment, with the MOE_{Dyn} generally yielding higher values than the static measurements. The adjustments maintain the relative differences between measurement techniques while standardizing the basis for comparison.

With this adjustment as the last piece of the puzzle, the Lamellas can be graded based on MOE and density values.

6.3. The Dynamic, Global and Local MOE of the Individual Azobe Lamellas

MOE_{Dyn}, MOE_{Global} and MOE_{Local}

The analysis begins with an in-depth look at the initial phase, which involved four-point testing of individual lamellas. The global and MOE_{Local} was to be analysed so as to clearly grade the individual lamellas. For the four-point bending tests conducted in the lab, each lamella was carefully positioned into the setup at the Stevin lab. The members were balanced and supported 3600 mm apart and marked at midspan a the center distance of 350 mm for the x lamellas and 700mm for the y lamellas, which marked the required distance for the MOE_{Local}. the EN 408 testing procedure was not followed to the dot.([43]).

An LVDT was then positioned at the center of the beams. A piece of wood was glued at the bottom of each beam on either side. Two lasers positioned below measured the deformation midspan of the beams, while the LVDT inside the jack also measured its deformation from the force exerted.

A slight force was applied to the beam by the jack, and then was adjusted to keep it in a plane while ensuring that twisting convergence could be guaranteed. The lasers below helped measure the deformation on both sides of the center of the beam at a distance of approximately 5 cm. The load was applied to the beam using the jack, resulting in a displacement of 64.9 mm or a force of 4.8 kN. This was done in increments of 0.36 mm/s for approximately 3 minutes.

The Excel files attached in the Appendix contain data columns representing the applied force (F01(KN)), mid-span deformations measured by lasers LS01(mm) and LS02(mm), the deformation of the jack (S(mm)), and local deformations recorded by LVDTs LVDT1 and LVDT3 on either side of the lamella.

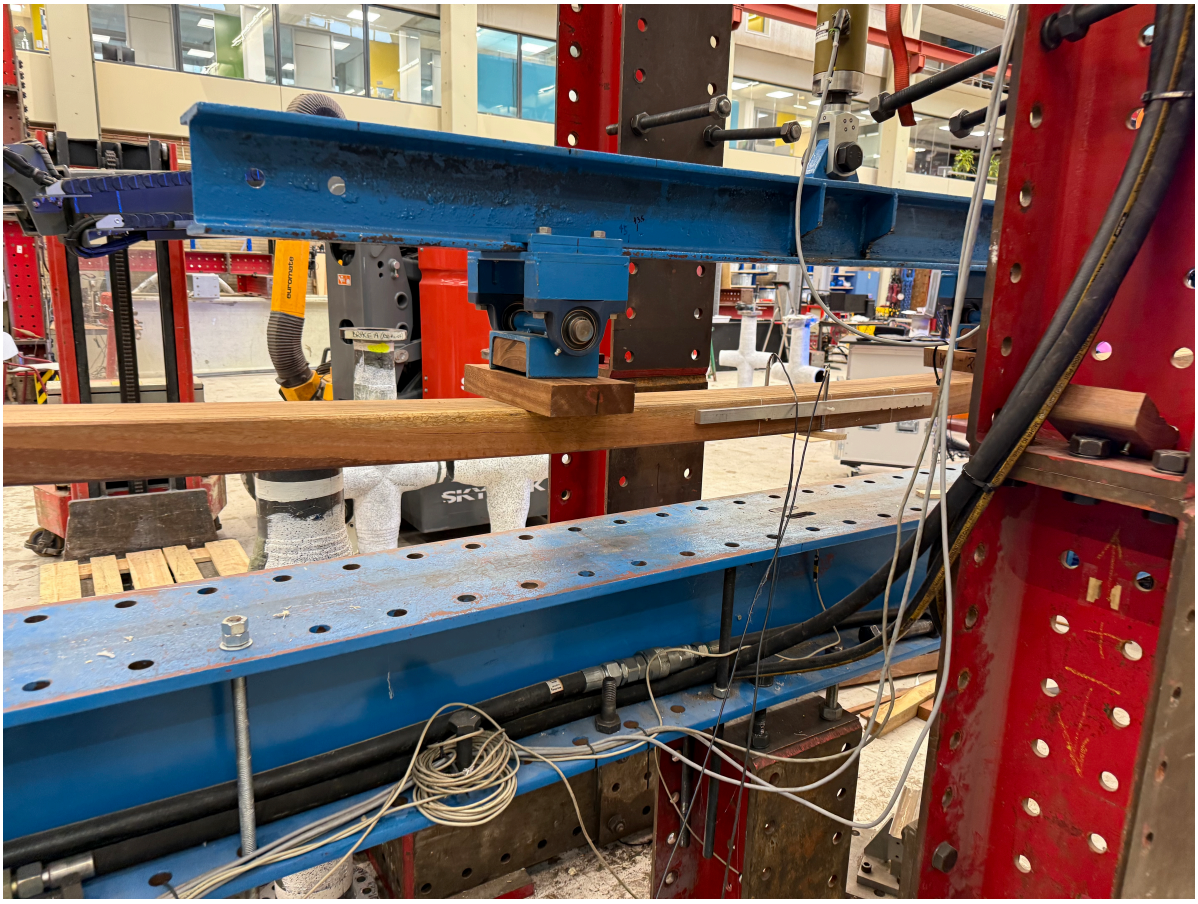

Figure 6.2: Four point bending test setup. Azobe lamella 70mm under testing

Using Python, the analysis compares deflection and force data by isolating the linear region for each deflection column (LS01, LS02, LVDT1, and LVDT3) between 10% and 90% of the maximum force, $F_{\max}$. Data below 0.1% of $F_{\max}$ and beyond the maximum force (e.g., 4.8 kN or higher) are excluded to remove irregularities and omit the offloading phase, allowing linear regression to accurately determine the slope and intercept for force estimation.

The Local and Global Modulus of Elasticity are calculated using specific formulas derived from the slope and intercept values. The value of shear according to the EN408 ([43])in the equation of the MOE_{Global} is taken as inifinity to isolate the aspect of the bending only.

MOE_{Local} equation

$$E_{\mathrm{m,l}} = \frac{al^2(F_2 - F_1)}{16I(w_2 - w_1)} \tag{6.8}$$

MOE_{global} equation with shear effects

$$E_{\mathrm{m,g}} = \frac{3al^2 - 4a^3}{2bh^3\left(2\frac{w_2 - w_1}{F_2 - F_1} - \frac{6a}{5Gbh}\right)} \tag{6.9}$$

Simplified MOE_{global} equation (with shear as infinity)

$$E_{\mathrm{m,g}} = \frac{(3al^2 - 4a^3)(F_2 - F_1)}{4bh^3(w_2 - w_1)} \tag{6.10}$$

where:

a = distance between loading point and nearest support

l = span length

$F_2 - F_1$ = load increment on the linear portion

$w_2 - w_1$ = corresponding displacement increment

b = beam width

I = second moment of area

G = shear modulus

These are the results of the data collected with the $MOE_{dyn}, MOE_{local}, MOE_{global}$ and percentage differences between the different values.

Table 6.3: Comparison of Different MOE Values and Physical Properties

Lamella ID	Mean Cross-sectional height	Wet Density ($kg\,m^{-3}$)	MOE Dyn (MPa)	MOE Global (MPa)	MOE Local (MPa)	% diff (L&G)	% diff (L&D)	% diff (G&D)
Y1	139.0	1190	17 500	15 200	17 400	12.6	0.6	13.1
Y2	138.7	1190	18 500	16 100	16 800	4.2	9.2	13.0
Y3	138.9	1180	18 500	15 500	14 600	−6.2	21.1	16.2
Y4	139.2	1190	17 900	16 000	17 600	9.1	1.7	10.6
Y5	139.1	1220	18 300	15 700	15 700	0.0	14.2	14.2
Y6	139.0	1210	17 400	15 200	15 600	2.6	10.3	12.6
X1	69.2	1120	17 400	14 400	16 100	10.6	7.5	17.2
X2	69.3	1070	18 500	15 500	15 900	2.5	14.1	16.2
X3	69.5	1160	22 000	19 200	20 200	5.0	8.2	12.7
X4	69.4	1150	20 700	18 100	19 100	5.2	7.7	12.6
X5	69.6	1160	19 300	16 000	17 500	8.6	9.3	17.1
X6	69.5	1140	18 200	15 400	16 600	7.2	8.8	15.4
X7	69.3	1110	18 100	15 300	15 800	3.2	12.7	15.5
X8	69.3	1100	21 000	15 700	16 800	6.5	20.0	25.2
X9	69.1	1100	19 000	15 700	14 700	−6.8	22.6	17.4
X10	69.7	1080	17 300	15 000	15 100	0.7	12.7	13.3

For the MOE_{Dyn}, the measured range was from 17 300 N/mm^2 to 22 000 N/mm^2, with a mean of approximately 19 100 N/mm^2. In these tests, lamella X3 exhibited the highest DYN MOE, indicating greater stiffness, while lamella X10 had the lowest.

In the case of the MOE_{Global}, the values ranged from 14 300 N/mm^2 to 19 200 N/mm^2, with a mean of roughly 16 200 N/mm^2. Here, lamellae X3 and X4 showed significantly higher values, whereas lamella X1 recorded the lowest.

For the MOE_{Local}, the measurements ranged from 14 700 N/mm^2 to 20 200 N/mm^2, with a mean of approximately 16 400 N/mm^2. Once again, lamella X3 demonstrated the highest value, confirming its superior localized and overall stiffness.

Additional observations include:

- Lamella X3 and X4 consistently showed high values across all MOE categories, suggesting these samples are the most robust and uniform.

- Lamella X9 had a MOE_{Local} that was 6.8% lower than its MOE_{Global}, which could be caused by imperfections within the lamella.
- One of the MOE_{Local} readings for lamella X5 was 3000 MPa lower in two separate experiments. This inconsistency, possibly due to twist or inhomogeneity in the wood, makes X5 a candidate for the drilling experiment rather than for the preparation of beams.

Table 6.4: Statistical Summary of MOE and Density Measurements

Parameter	Mean ± SD	CV (%)	Min	Max
Y Series (h = 139 mm, n = 6)				
MOE_{Dyn}	18016.7±485.6	2.7	17400.0	18500.0
MOE_{Global}	15616.7±367.1	2.4	15200.0	16100.0
MOE_{Local}	16283.3±1186.3	7.3	14600.0	17600.0
Density	1195.8±14.2	1.2	1182.0	1217.0
Height	139.0±0.2	0.1	138.7	139.2
X Series (h = 69 mm, n = 10)				
MOE_{Dyn}	19150.0±1524.4	8.0	17300.0	22000.0
MOE_{Global}	16030.0±1477.0	9.2	14400.0	19200.0
MOE_{Local}	16780.0±1678.3	10.0	14700.0	20200.0
Density	1118.1±31.4	2.8	1074.0	1163.0
Height	69.4±0.2	0.3	69.1	69.7

MOE values in MPa
Density in kg/m^3
Height in mm
SD = Standard Deviation
CV = Coefficient of Variation
n = number of specimens

The density values ranged differently for all the beams with a mean and max of 1070 and 1160. While the y series had a much higher min and max of 1180kg/m3 and 1220kg/m3. The standard deviation between the results for the y series was 14 and 33 for the x series around a mean of about 1200 and 1100 kg/m3 . A percentage difference of 8% between the 2 sets of beams. The smaller deviations in the density values of the Y series shows consistency between the values compared to the x series. The density results showed differences between the X(70mm) and Y(140mm)series beams. The X series had a wider density range (1074-1163 kg/m³) and higher standard deviation (33 kg/m³) compared to the Y series (range: 1182-1217 kg/m³, SD: 14 kg/m³). The Y series beams were, on average, 8% denser than the X series, with mean densities of 1200 kg/m³ and 1120 kg/m³, respectively. To quantify the relationship between density and cross sectional height, a linear regression analysis was performed as shown in the graph attached . The results indicated a significant positive correlation between density and height ($R^2 = 0.82$). This suggests that higher cross sectional azobe beams tend to have higher densities, which aligns with the observed higher mean density of the Y series compared to the X series.

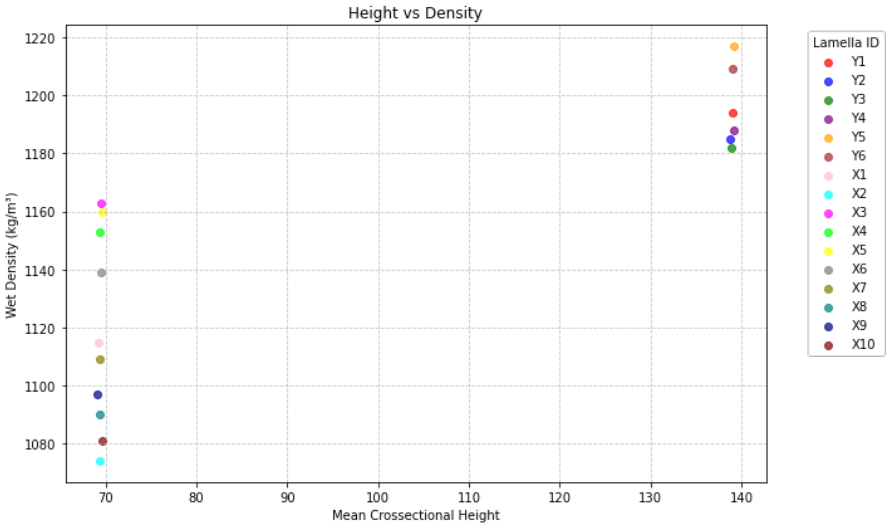

Figure 6.3: Graph showing the relationship between height and density: X beams (70 mm) on the left and Y beams (140 mm) on the right

Several factors could contribute to this density–height relationship. Higher beams may be sourced from older or slower-growing trees, which have had more time to develop denser wood. The greater cross-sectional area of taller beams may also allow for more consistent density distribution, as localized variations have less influence on the overall density.

Another explanation for this (the higher density of the Y series beams compared to the X series) could be partially attributed to differences in water retention. As the density measurements in this study were based on wet density rather than dry density, the moisture content of the beams may have played a role in the observed density variations. Considering that all beams in this study were approximately 4 m long and ∼140 mm wide, the X series beams (70 mm height) had a surface area to volume ratio of 0.086 m^2/m^3, while the Y series beams (140 mm height) had a ratio of 0.064 m^2/m^3. This means that the Y series beams had approximately 26% less surface area per unit volume compared to the X series beams, leading to the slower moisture loss and higher wet densities observed in the Y series.

The heartwood of azobe contains a high concentration of extractives, such as flavonoids and tannins, which contribute to its resistance to decay and moisture uptake, whereas the sapwood of azobe, which is more permeable, may allow for greater water retention, particularly in larger beams.

The observed relationship between density and height is based on a limited sample size and only two specific beam heights. Further research with a wider range of beam sizes would be necessary to establish a more robust understanding of this relationship and its potential implications for the mechanical properties of azobe timber.

6.4. Modulus of Elasticity

All three MOE measures (global, dynamic, and local) were assessed. The MOE_{Global} ranged from 14,400 to 19,200 MPa for the X series, with a mean of 16,000 MPa and a standard deviation of 1,500 MPa. The Y series had a narrower MOE_{Global} range (15,200–16,100 MPa), a lower mean (15,600 MPa), and a considerably smaller standard deviation (400 MPa).

MOE_{Dyn} values were consistently higher than MOE_{Global} for both series. The X series had a mean MOE_{Dyn} of 19,100 MPa (SD: 1,600 MPa), while the Y series averaged 18,000 MPa

(SD: 500 MPa). MOE_{Local} values fell between the global and dynamic measures, with means of 16,800 MPa (X series) and 16,300 MPa (Y series). Figure 6.4 presents boxplots comparing the MOE distributions between the two beam series.

Analysis of variance (ANOVA) tests were conducted to compare each MOE measure between the X and Y series. The results indicated no significant difference in mean MOE_{Global} ($F = 0.41$, $p = 0.53$) or MOE_{Local} ($F = 0.33$, $p = 0.58$). However, the Y series exhibited a significantly lower mean MOE_{Dyn} compared to the X series ($F = 5.42$, $p < 0.05$).

Figure 6.4: Boxplots comparing the MOE distributions between the X and Y series beams.

6.4.1. Relationships between Properties

Correlation analysis explored the relationships between density and the MOE parameters. Density showed significant positive correlations with all three MOE measures, suggesting that denser azobe beams generally exhibit higher stiffness. The strongest correlation was observed between density and MOE_{Global} (Pearson's $r = 0.74$, $p < 0.01$), followed by MOE_{Dyn} ($r = 0.68$, $p < 0.01$) and MOE_{Local} ($r = 0.52$, $p < 0.05$). Figure 6.5 presents scatter plots with trend lines illustrating these relationships.

Interestingly, the Y series beams demonstrated more consistent MOE values despite their higher average density. This suggests that factors beyond density, such as wood microstructure or processing methods, may influence the stiffness properties of azobe timber.

Figure 6.5: Scatterplots with trendlines illustrating the relationships between density and the MOE parameters.

MOE vs. Height, Density, and Inter-relationships

The elastic properties of timber beams can be characterised through three primary methods to determine the modulus of elasticity (MOE): global, local, and dynamic approaches. Each method provides mechanical behaviour of the material while presenting specific advantages and limitations in their application.

The (MOE_{Global}) combined the effects of bending and shear deformation within the beam structure. This parameter is determined through standardised four-point bending tests, where the total deflection is measured at the mid-span of the beam. The resulting (MOE_{Global}) value incorporates both pure bending deformation and shear effects, consequently yielding lower values compared to alternative measurement methods. The calculation follows the principles established in standards such as EN 408 [43], which provide standardised testing protocols and calculation procedures.

In contrast, the (MOE_{Local}) specifically quantifies the pure bending characteristics of the timber beam, deliberately excluding shear deformation effects. This measurement is obtained by recording deflection within the constant moment zone between loading points during four-point bending tests. Measurement of deformation over a gauge length within the force application where shear forces are theoretically zero provides us with a more direct representation of the elastic properties of the material. This method produces higher numerical values compared to global measurements, as it eliminates the influence of shear deformation.

The MOE_{Dyn} represents a nondestructive alternative to static testing methods. This approach derives elastic properties from the beam's vibrational characteristics, utilising either longitu-

dinal or transverse wave propagation principles. The calculation of MOE_{Dyn} is previously explained in chapter 5 . Dynamic testing offers several practical advantages, including rapid data acquisition and the possibility of repeated measurements on the same specimen. Although dynamic measurements generally demonstrate strong correlation with static values, the relationship may require calibration factors to account for systematic differences between dynamic and static behaviour and these relationships can be found in the literature [45].

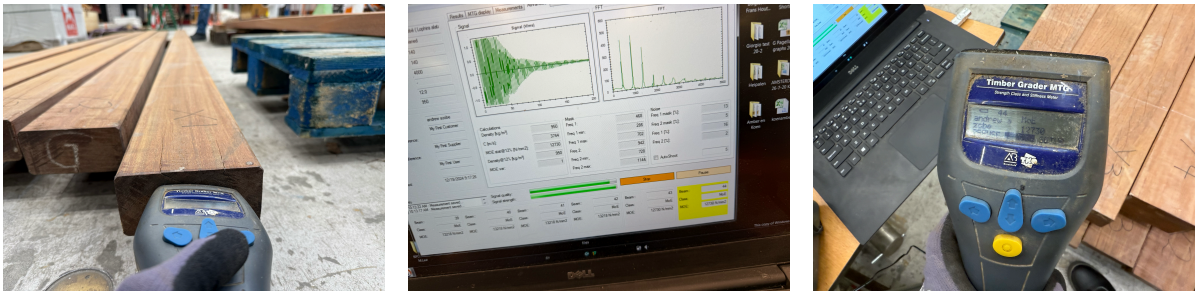

Figure 6.6: Shows measuring the dynamic Modulus of Elasticity (MOE) in timber using a handheld Timber Grader MFD, with the resulting acoustic data analysed in real time. From left to right:

1. Using a handheld Timber Grader MFD on a row of AZobe lamellas to measure MOE_{Dyn}.
2. Viewing the real-time acoustic analysis and data on the laptop.
3. A closer look at the grader's readout.

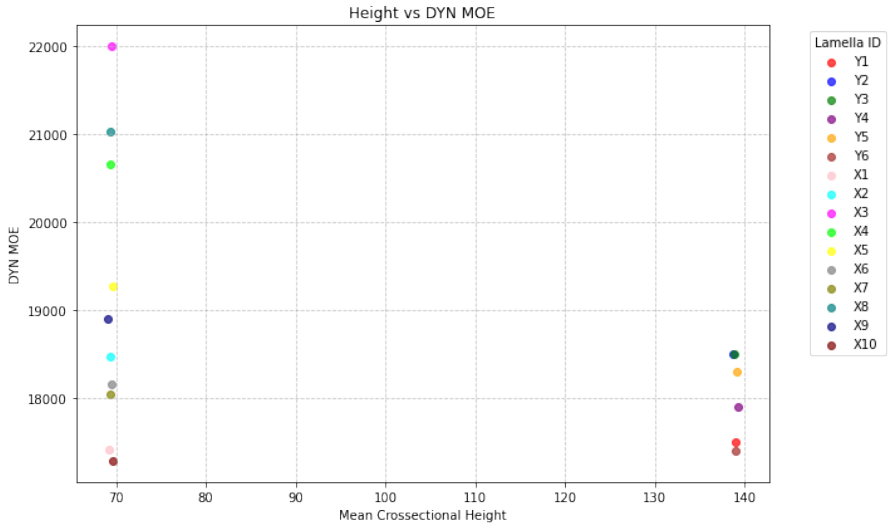

(a) Density vs. Dyn MOE

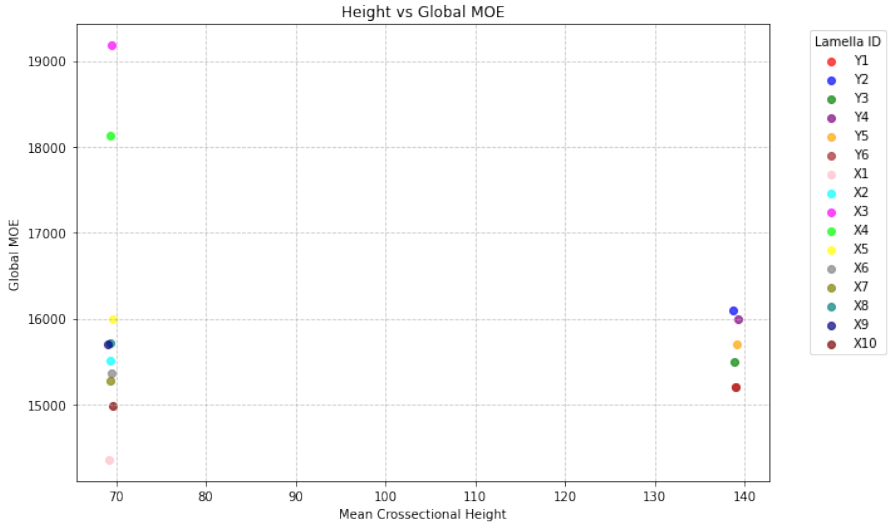

(b) Density vs. MOE_{Global}

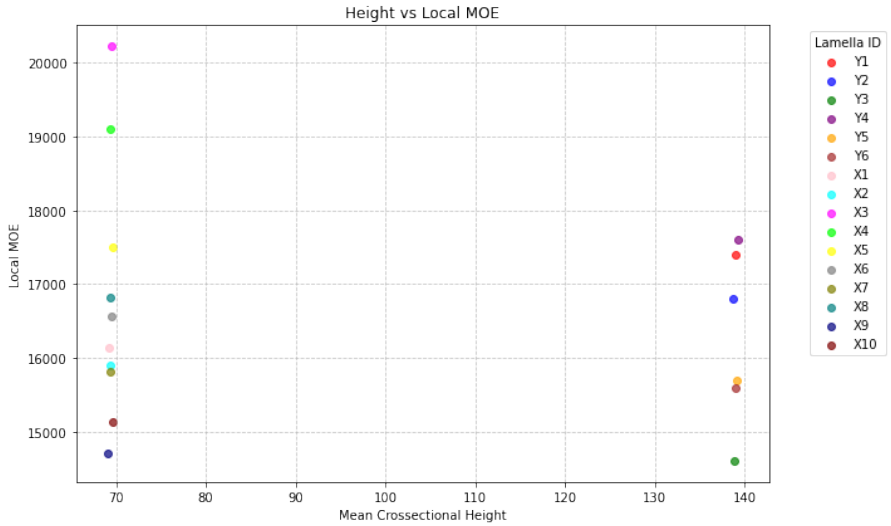

(c) Density vs. MOE_{Local}

Figure 6.7: Comparison of local, global, and MOE_{Dyn} values versus each lamella's mean cross-sectional height, shown separately for Y-lamellas (140mm) and X-lamellas (70mm).

The relationship between MOE and beam height is not well established and there is barely a correlation between the different heights of the beams cross sections. In this study, the Y series beams, with a height of 140 mm, generally exhibited lower mean values for all three MOE measures compared to the X series beams, which had a height of 70 mm.

We can note that the differences in MOE between the two beam series were not statistically significant for MOE_{Global} (F = 0.41, p = 0.53) and MOE_{Local} (F = 0.33, p = 0.58). The lack of a consistent and significant relationship between beam height and MOE in this study suggests that other factors, such as density and microstructural properties, may have a more dominant influence on the stiffness of azobe timber.

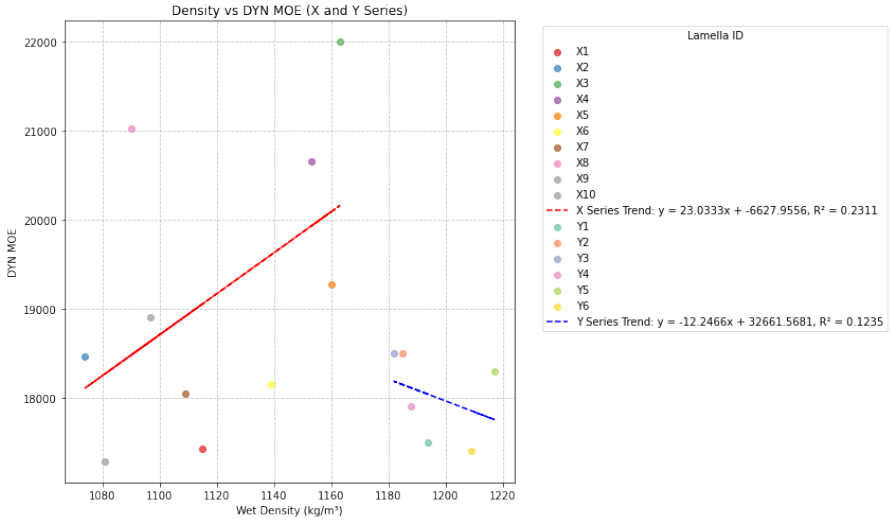

(a) Density vs. Dyn MOE

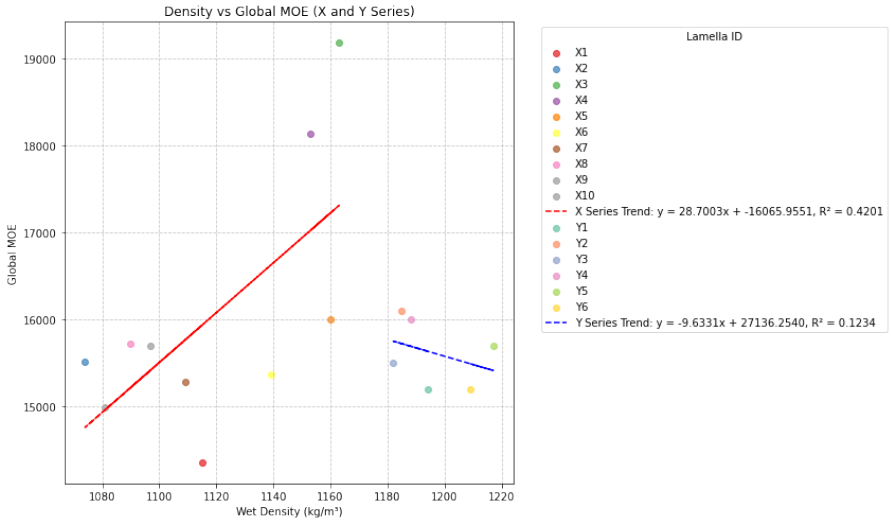

(b) Density vs. MOE_{Global}

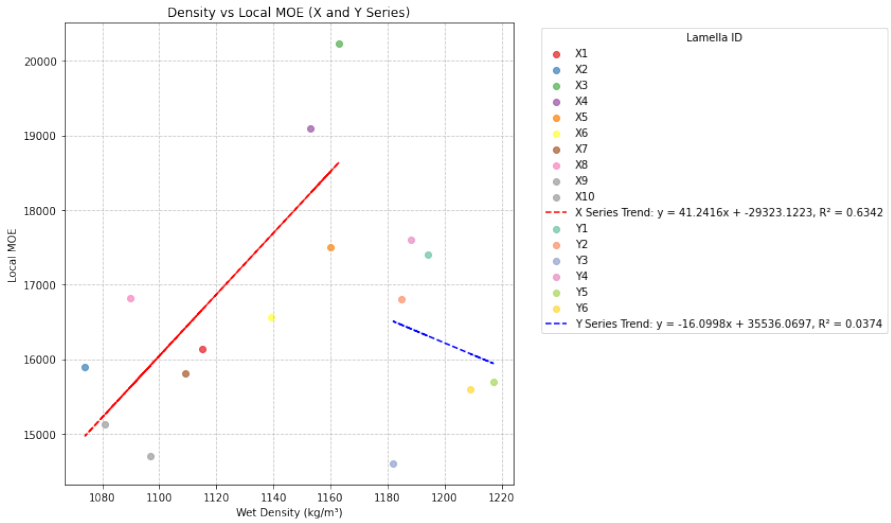

(c) Density vs. MOE_{Local}

Figure 6.8: Scatter plots of two lamella data sets (X-series in red, Y-series in blue), each with a best-fit linear trend line and corresponding R^2 value. Points represent individual lamella IDs (X1–X10 for the X-series, Y1–Y6 for the Y-series). Comparison of the wet density and different MOE VALUES.

6.5. Analysis of Density-Stiffness Correlations

The investigation of density-stiffness relationships in azobe lamellae revealed distinct behavioral patterns between X and Y series specimens. Statistical analysis demonstrated varying correlations across different Modulus of Elasticity (MOE) measurement methodologies.

6.5.1. X Series Correlations

The X series exhibited positive correlations across all measurement methods, with correlation strengths varying significantly:

- MOE_{Local} demonstrated the strongest correlation ($R^2 = 0.6342$) with density, following the relationship:

$$y = 41.2416x - 29323.1223 \tag{6.11}$$

- MOE_{Global} showed a moderate correlation ($R^2 = 0.4201$), expressed as:

$$y = 28.7003x - 16065.9551 \tag{6.12}$$

- MOE_{Dyn} exhibited the weakest correlation ($R^2 = 0.2311$):

$$y = 23.0333x - 6627.9556 \tag{6.13}$$

6.5.2. Y Series Correlations

In contrast, the Y series exhibited consistently weak negative correlations across all measurements ($R^2 \leq 0.1235$), with equations suggesting an inverse density-stiffness relationship:

- MOE_{Dyn}: $R^2 = 0.1235$

$$y = -12.2466x + 32661.5681 \tag{6.14}$$

- MOE_{Global}: $R^2 = 0.1234$

$$y = -9.6331x + 27136.2540 \tag{6.15}$$

- MOE_{Local}: $R^2 = 0.0374$

$$y = -16.0998x + 35536.0697 \tag{6.16}$$

These negative correlations, while statistically weak ($R^2 \leq 0.1235$), represent an anomalous behaviour that deviates from conventional density-stiffness relationships in wood materials. The extremely low values R^2 suggest that density may not be a reliable predictor of mechanical properties in Y-series samples. This observation is particularly significant considering the comparison of wet densities.

6.5.3. Discussion of Findings

Observations reveal the distinct difference in correlation patterns between the X and Y series. While the X series follows expected mechanical behaviour with positive density-stiffness correlations, the Y series exhibits weak negative correlations that contradict traditional wood mechanics principles. This divergence suggests the potential influence of other factors beyond density on the mechanical properties of the Y series specimens, such as moisture content.

6.5.4. Implications

The weak correlations between density and all MOE measures ($R^2 \leq 0.056$) suggest that wet density alone may not be a reliable predictor of stiffness properties in azobe timber. This finding contrasts with traditional assumptions about wood behaviour, where stronger density-stiffness correlations are typically expected.

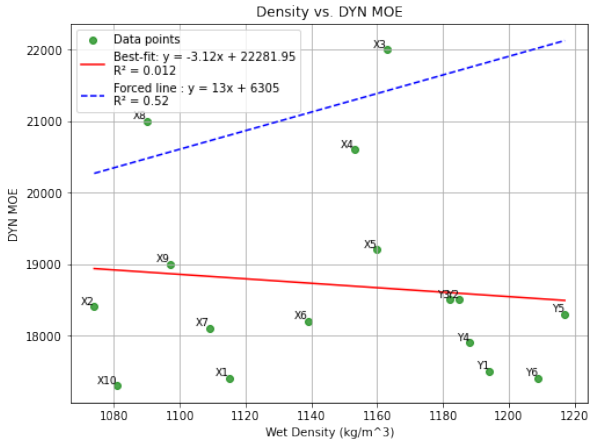

(a) Density vs. Dyn MOE

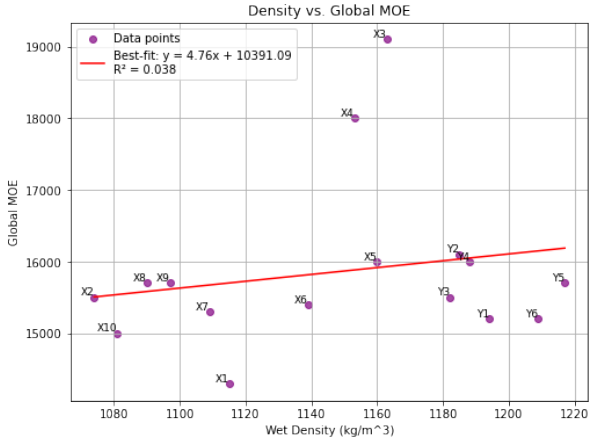

(b) Density vs. MOE_{Global}

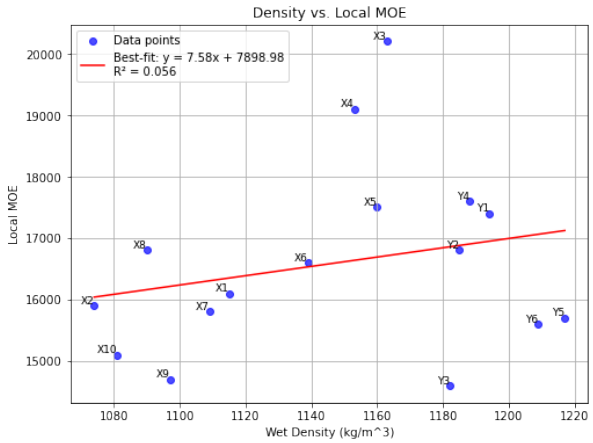

(c) Density vs. MOE_{Local}

Figure 6.9: Combined relation of the wet density and the MOE values. The top plot shows both a best-fit (red) and a forced (blue) regression line over the data points (green), along with their respective R^2 values. The middle plot illustrates the same data and best-fit line on a different scale, while the bottom plot presents a separate data set (purple) with its own best-fit line and R^2.

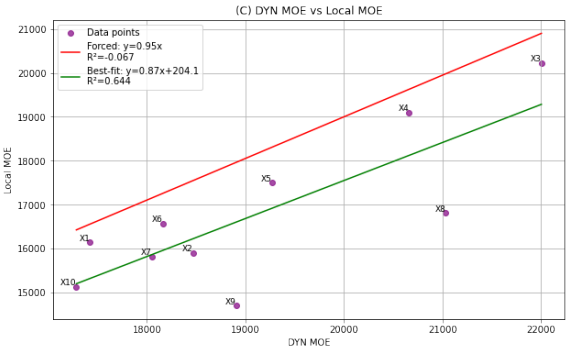

(a) (C) DYN MOE vs MOE_{Local}

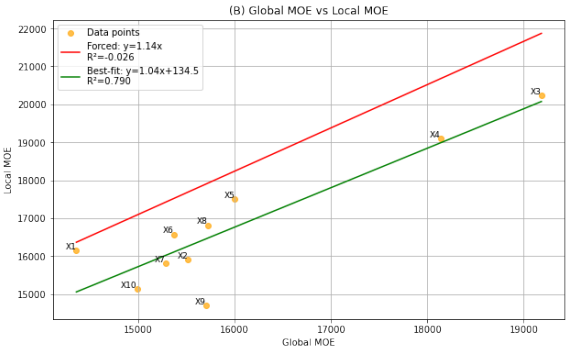

(b) DYN MOE vs MOE_{Global}

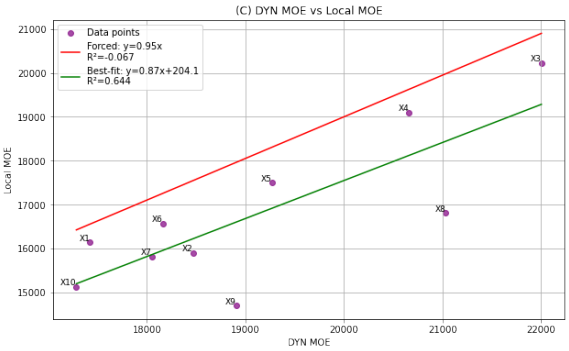

(c) MOE_{Global} vs MOE_{Local}

The relationship between the measured MOE values of only X lamellas with published data in red for tropical hardwoods found in the literature ([45]).

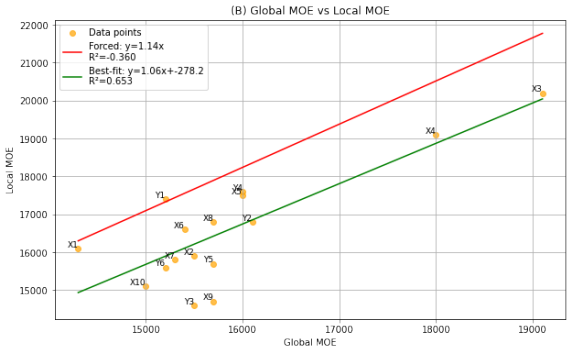

(d) (C) DYN MOE vs MOE_{Local}

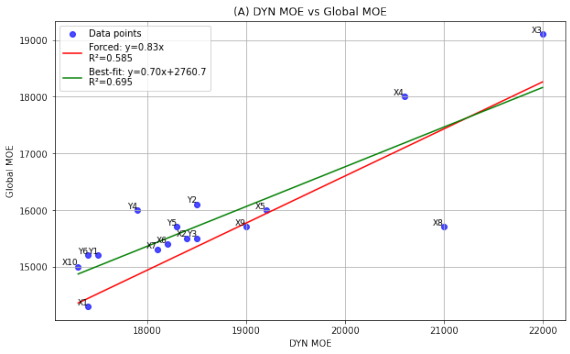

(e) (A) DYN MOE vs MOE_{Global}

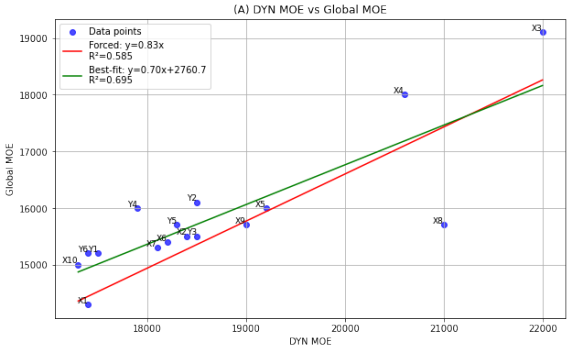

(f) (B) MOE_{Global} vs MOE_{Local}

The combined relationship between the measured MOE values of X and Y lamellas with published data in red for tropical hardwoods found in the literature ([45]).

6.6. Analysis of MOE Measurement Relationships

The relationship between different Modulus of Elasticity (MOE) measurement methods was investigated to establish reliable correlations for structural assessment of mechanically jointed azobe beams. Three primary relationships were analysed: MOE_{Global} versus MOE_{Local}, MOE_{Dyn} versus MOE_{Global}, and MOE_{Dyn} versus MOE_{Local}.

6.6.1. MOE_{Global} and MOE_{Local} Relationship

The relationship between Global and MOE_{Local} demonstrates a consistent positive correlation in all test specimens. Analysis revealed that MOE_{Local} values were generally higher than

MOE_{Global} measurements, with best-fit slopes ranging from 1.01× to 1.06×. This relationship exhibited varying degrees of correlation strength, with the highest coefficient of determination ($R^2 = 0.65 - 0.77$) observed in the final iteration of the test.

A forced linear regression from Geert [45] consistently showed lower R^2 values ($0.2 - 0.4$) compared to the best-fit analysis, suggesting that the relationship may not be linearly correlated with the tested data. It should also be noted that the forced linear regression was based on tropical woods of varying material properties and not only Azobe.

6.6.2. MOE_{Dyn} and MOE_{Global} Correlation

The most robust correlation was observed between the MOE_{Dyn} and MOE_{Global} measurements. This relationship demonstrated:

- Highest correlation coefficient of determination ($R^2 = 0.70 - 0.74$)
- Consistent best-fit slope of approximately ($0.70 \times -0.79\times$)
- Minimal scatter in data points compared to other relationships
- Strong agreement between forced and best-fit regression models at higher MOE values

The strength of this correlation suggests that MOE_{Dyn} measurements could serve as a reliable predictor of MOE_{Global} in mechanically jointed azobe beams, potentially offering a non-destructive assessment method for structural applications.

6.6.3. MOE_{Dyn} and MOE_{Local} Analysis

This relationship revealed a moderate correlation coefficient, with coefficient of determination (R^2) values ranging from 0.431 to 0.644 across the test series. The forced linear regression analysis from literature implemented a coefficient of 0.95 compared to the 0.75 and 0.86 which demonstrated an overestimation of the relationship compared to empirical observations.

Statistical analysis indicated significantly higher variance in the data distribution compared to the dynamic MOE_{Global} correlation, suggesting an increased sensitivity to local material properties and joint behaviour. Furthermore, the correlation strength exhibited notable variation across multiple test iterations, indicating potential influence of specimen-specific factors such as local material heterogeneity.

6.6.4. Conclusions

The analysis of the three MOE measurement relationships reveals several key findings:

- MOE_{Dyn} measurements provide the most reliable correlation with MOE_{Global}
- MOE_{Local} measurements show higher absolute values but greater variability
- Dynamic testing methods could be implemented for rapid, non-destructive assessment to quickly gauge the overall stiffness of the beam

It should be noted that acoustic methods are sensitive to the overall vibrational properties of the beam. In contrast, global and MOE_{Local} are based on static bending tests that directly measure the beam's deformation under load.

The positive correlations among all three MOE measures suggest that they capture related aspects of the beam's stiffness, but each method provides distinct information that can contribute to a more understanding of the elastic behaviour of azobe timber.

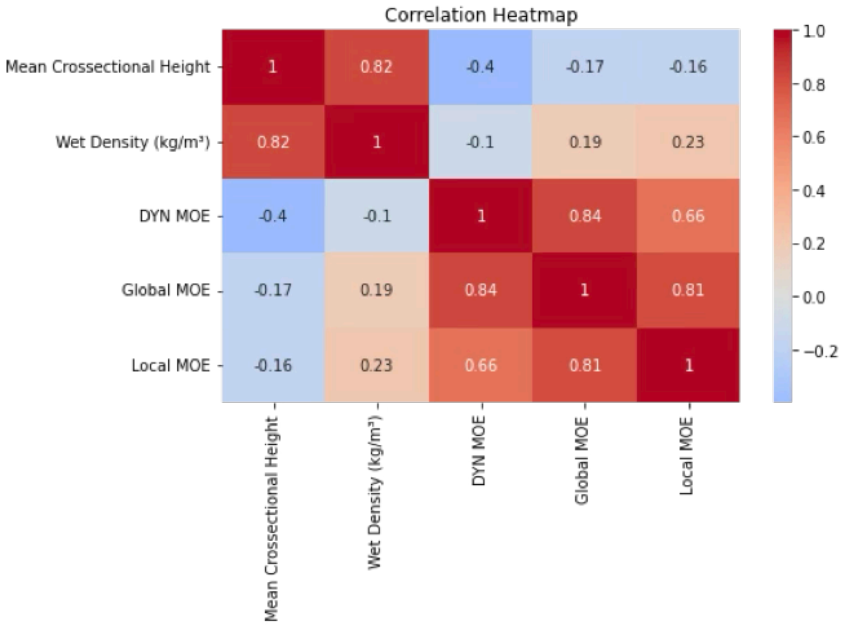

A correlation heat map relating all parameters affecting lamella stiffness

Figure 6.11: A correlation heat map relating all parameters affecting lamella stiffness

6.7. Effect of the drilling holes into the lamellas

20 mm hole drilled into the lamella

Figure 6.12: 20 mm hole drilled into the lamella

It was interesting to investigate the stiffness of the lamellas once they have been drilled. It was noted that there are changes in the structural stiffness in this lamella but by how much and what kind of relationship does it have with volume reduction . Is it a linear relationship or nonlinear one.

Table 6.5: MOE_{Global} and MOE_{Local} of X2, X5 and X9

ID	Wet Density (kg/m³)	TEST 1		TEST 2		% difference between values	
		MOE_{Global}	MOE_{Local}	MOE_{Global}	MOE_{Local}	MOE_{Global}	MOE_{Local}
X2	1074	15500	15100	15500	15100	0.0	0.0
X5	1160	16200	18000	16000	17500	1.2	2.8
X9	1097	15800	14700	15700	14700	0.6	0.0

Table 6.6: MOE_{Global} and MOE_{Local} of X5 and X9 when drilled

ID	Wet Density (kg/m³)	Before drilling holes		After drilling 9 holes		After drilling 17 holes	
		MOE_{Global}	MOE_{Local}	MOE_{Global}	MOE_{Local}	MOE_{Global}	MOE_{Local}
X5	1160	16000	17500	16000	16200	15300	15700
X9	1097	15700	14700	15200	14100	14700	13700

Table 6.7: MOE_{Global} and MOE_{Local} of X5 and X9 when drilled

ID	Wet Density (kg/m³)	% decrease After drilling 9 holes		% decrease After drilling 17 holes		% decrease After drilling 17 holes from 9 holes	
		MOE_{Global}	MOE_{Local}	MOE_{Global}	MOE_{Local}	MOE_{Global}	MOE_{Local}
X5	1160	0.0	7.4	4.4	10.3	4.4	3.1
X9	1097	3.2	4.1	6.4	6.8	3.3	2.8

The investigation focused on understanding the impact of drilling holes on the structural stiffness of *azobe* beam lamellas. Initial testing confirmed the consistency of stiffness measurements across randomly selected specimens (X2, X5, and X9), establishing a baseline for further analysis.

Specimens X5 and X9 were subjected to progressive drilling of 9 and 17 holes to evaluate the resulting changes in structural properties.

The preliminary testing showed good consistency in stiffness measurements, with variations typically below 3% between repeated tests. Specimen X5 showed some small variations of approximately 500 MPa, while X9 exhibited almost no significant change in both the global and MOE_{Local} after the second test.

The MOE_{Local} showed greater sensitivity to drilling, with higher reduction percentages across both specimens. The MOE_{Global} demonstrated more stability, particularly in X5's initial drilling phase.

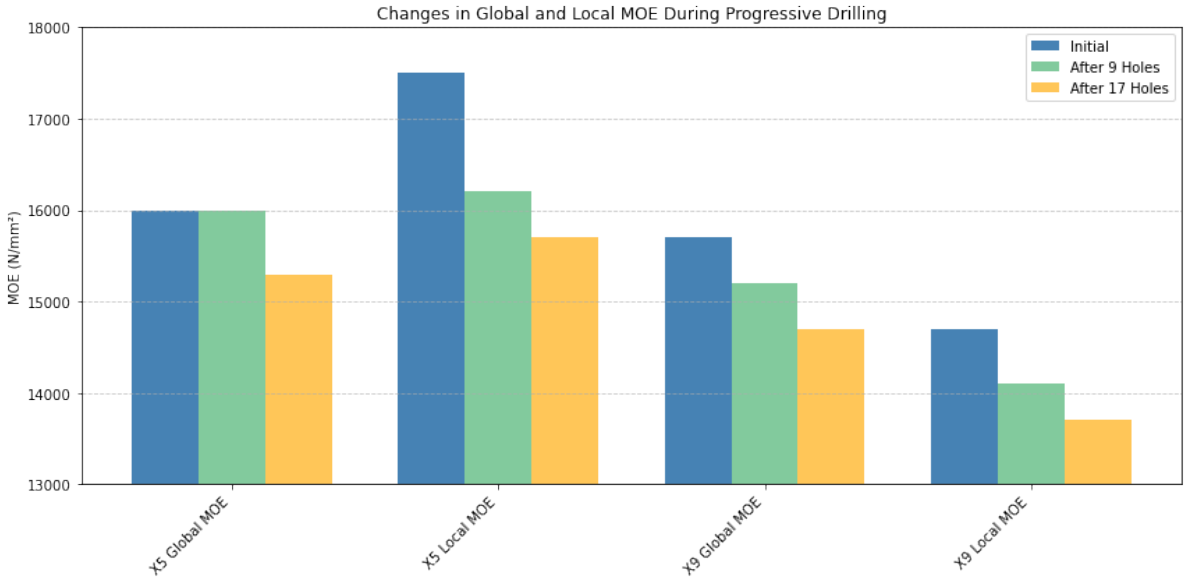

Figure 6.13: reduction of stiffness in the lamellas

6.7.1. Volume and Mass Reduction Analysis

The drilling process resulted in quantifiable reductions in both volume and mass of the specimens. The holes drilled are 20mm and through the thickness of the specimen. The calculations yielded a volume/ mass percentage reduction of approximately 22,000 mm³ per hole. With an Initial volume of 0.0392 m³. The Volume and mass reduction percentages were : - 9 holes: 0.50- 17 holes: 0.95

The MOE_{Local} measurements showed higher sensitivity to volume reduction in the higher density specimen X9 and the MOE_{Global} measurements demonstrated more consistent relationship with volume reduction across both specimens.

Unfortunately there were only two sample lamellas drilled and they showed a nonlinear relationship. The volume reduction between specimens varied by only 0.01% for both 9 and 17 holes. However, the stiffness reduction varies by up to 7.43%. This indicates that factors beyond simple material removal significantly influence stiffness changes.

6.7.2. Conclusion

It is consistent that there is reduction in the stiffness of the lamellas after drilling and even though its not properly quantifiable and needs further research.

6.8. Arrangement of the beams lamellas

To arrange the beam lamellas after choosing which lamellas will be used. X1, X2, X3, X4, X6, X7, X8, X10, and Y1, Y2, Y4 ,Y6 were decided on due to having less imperfections. Both a four point bending and three point bending were then done on the stacked beams to obtain results. The placement of the beam lamellas was made in such a way that the stiffness were varied. For instance by placing a stiffer beam at the bottom or placing it in the middle. It was to be found out if it matters where then beams are placed or does it have no influence on the results. For that matter, the beam setups were then made based on the MOE_{Global} values as the MOE_{Local} of a stacked beam is that of only an individual lamella.

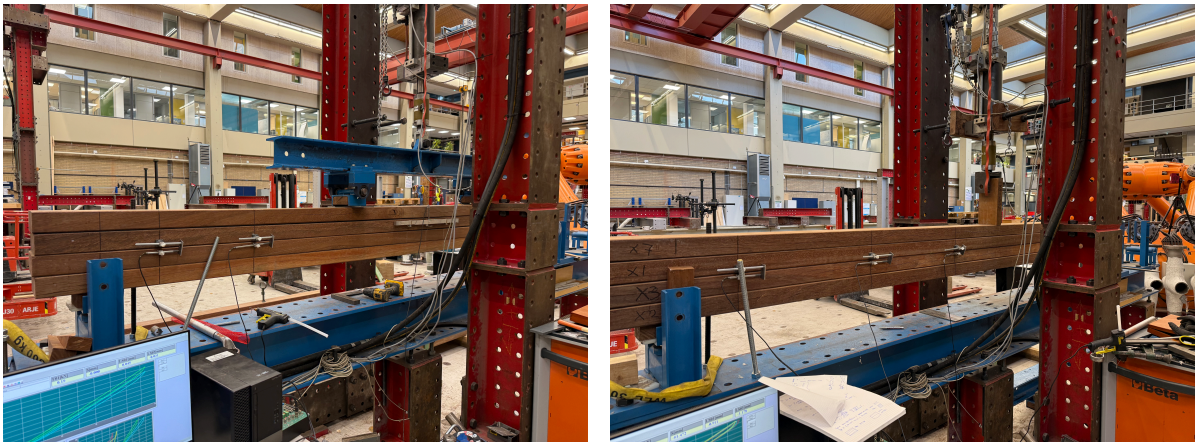

(a) Four-point bending test **(b)** Three-point bending test

Figure 6.14: *Side-by-side comparison of four-point bending (left) and three-point bending (right) test for X setups.*

(a) Four-point bending test **(b)** Three-point bending test

Figure 6.15: *Side-by-side comparison of four-point bending (left) and three-point bending (right) test for Y setups.*

To achieve a neutral axis (line of zero bending stress) in the middle of the arrangement for each beam, the stiffness distribution must be symmetric. This means the top and bottom layers of each beam should have similar stiffness properties, and the central layers should balance the arrangement. Given the MOE values (DYN MOE, MOE_{Global}, MOE_{Local}) and assuming lamellas have the same dimensions, we will calculate the neutral axis placement and arrange

them accordingly.Symmetric Pairs have been identified and ones with the highest stress are placed on the outside. Neutral Axis ensure the stiffness (MOE) distribution is symmetric about the center.

6.8.1. Beam Configurations

Beam A1

This arrangement had the stiffest lamella at the lower middle of the arrangement.

Top Layer:	Y1	(15200 N/mm^2)
Bottom Layer:	Y2	(16100 N/mm^2)

Figure 6.16: Beam A1

The neutral line will be found in the lower part.

Beam A2

This arrangement had the stiffest lamella at the lower middle of the arrangement.

Top Layer:	Y6	(15200 N/mm^2)
Bottom Layer:	Y4	(16000 N/mm^2)

Figure 6.17: Beam A2

The neutral line will be slightly in the lower half but closer to the center

Beam B1-1

This arrangement had the stiffest lamella at the very bottom of the arrangement.

Top Layer:	X8	(15700 N/mm^2)
Upper Middle Layer:	X6	(15400 N/mm^2)
Lower Middle Layer:	X10	(15000 N/mm^2)
Bottom Layer:	X4	(18100 N/mm^2)

Top MOE: X8 + X6 = 15700 + 15400 = 31100
Bottom MOE: X10 + X4 = 15000 + 18100 = 33100

the neutral line will be captured slightly in the lower half

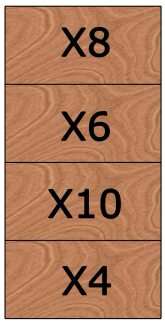

Figure 6.18: Beam B1-1

Beam B1-2

This arrangement had the stiffest lamella at the middle top of the arrangement.

Top Layer:	X8	(15700 N/mm^2)
Bottom Layer:	X4	(18100 N/mm^2)
Upper Middle Layer:	X6	(15400 N/mm^2)
Lower Middle Layer:	X10	(15000 N/mm^2)

Top MOE: X8 + X4 = 15700 + 18100 = 33800
Bottom MOE: X10 + X6 = 15000 + 15400 = 30400

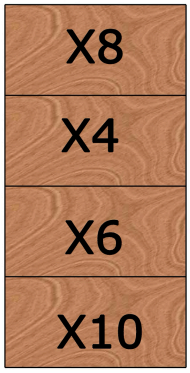

Figure 6.19: Beam 1-2

the neutral line will be above the central beam

Beam B2-1

This arrangement had the stiffest lamella at the top of the arrangement.

Top Layer:	X3	(19100 N/mm^2)
Upper Middle Layer:	X2	(15500 N/mm^2)
Lower Middle Layer:	X7	(15300 N/mm^2)
Bottom Layer:	X1	(14400 N/mm^2)

Top MOE: X7 + X9 = 19100 + 15500 = 34600
Bottom MOE: X3 + X2 = 15300 + 14400 = 29700

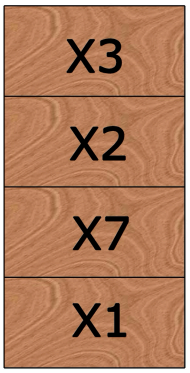

Figure 6.20: Beam B2-1

the neutral line will be in the upper half of the beam

Beam B2-2

This arrangement had the stiffest lamella at the lower middle of the arrangement.

Top Layer:	X7	(15300 N/mm^2)
Upper Middle Layer:	X1	(14400 N/mm^2)
Lower Middle Layer:	X3	(19100 N/mm^2)
Bottom Layer:	X2	(15500 N/mm^2)

Top MOE: X7 + X9 = 14400 + 15300 = 29700
Bottom MOE: X3 + X2 = 19100 + 15500 = 34600

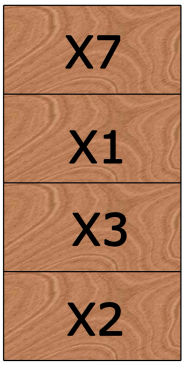

Figure 6.21: Beam B2-2

The stacked unjointed azobe beams were experimentally evaluated using both three-point and four-point bending tests in the elastic deformation range. The effective bending stiffness (EI_{eff}) was determined using the following formulae for each testing method.

For the four-point bending test, the effective bending stiffness (EI_{eff}) was calculated using the following equation:

$$EI_{\text{eff}} = \text{slope} \times \frac{(3aL^2 - 4a^3)}{48} \quad (\text{N mm}^2) \tag{6.17}$$

where a represents the distance from the support to the nearest load point, L is the span length, and slope is the linear relationship between applied load and deflection.

For the three-point bending test, the effective bending stiffness (EI_{eff}) was determined using:

$$EI_{\text{eff}} = \frac{\text{slope} \cdot L^3}{48} \quad (\text{N mm}^2) \tag{6.18}$$

where L is the span length, and slope represents the load-deflection relationship in the elastic region.

The experimental results from both testing methods were compared with analytical predictions to evaluate the structural performance of the stacked unjointed azobe beam configurations.

Table 6.8: Comparison of Analytical and Four-Point Bending Test Results for Stacked Unjointed Beams

Beam	Setup	Analytical stiffness (EI_{eff}) $\times 10^{11}$ (Nmm^2)	Four-point stiffness (EI_{eff}) $\times 10^{11}$ (Nmm^2)	% difference
A1	Y1-Y2	10.05	10.31	−2.57
A2	Y6-Y4	9.99	10.18	−1.92
B1-1	X8-X6-X10-X4	2.58	2.77	−7.46
B1-2	X8-X4-X6-X10	2.58	2.85	−10.43
B2-1	X3-X2-X7-X1	2.58	2.72	−5.59
B2-2	X7-X1-X3-X2	2.58	2.71	−4.97

Only a slight or negligible difference in effective stiffness was observed when the lamellae were placed in different positions. Specifically, beams B2-1 and B2-2 exhibited a percentage difference of merely 0.4%, whereas B1-1 and B1-2 showed a higher discrepancy of 4.6%. These results suggest that the placement of the stiffest lamella in the beams may indeed influence the overall stiffness, despite current Eurocode 5 [17] calculations disregarding this factor. However, further investigation is required to fully understand the implications of lamella positioning on beam performance.

In the four-point bending tests, the discrepancy between the analytical predictions and the experimentally measured bending stiffness reached 10.4% in one of the tests but was overall higher in all arrangements. This outcome indicates the presence of an additional parameter influencing the combined stiffness of the stacked beams. A plausible explanation involves friction between the lamellas, which creates a shear interaction effect. However, further research is required to thoroughly investigate and quantify this phenomenon.

Table 6.9: Comparison of Analytical and Three-Point Tested Stiffness for Beams

Beam	Setup	Analytical stiffness (EI_{eff}) $\times 10^{11}$ (Nmm^2)	Three-point stiffness (EI_{eff}) $\times 10^{11}$ (Nmm^2)	% diff.
A1	Y1-Y2	10.05	10.44	−3.84
A2	Y6-Y4	9.99	9.48	5.13
B1-1	X8-X6-X10-X4	2.56	2.63	−2.50
B2-2	X7-X1-X3-X2	2.58	2.56	0.62

After selecting the stiffest configurations, three-point bending tests were performed on the remaining specimens. The results indicated that all bending stiffness values, calculated using different methods, fell within a ±6% margin of each other. Specifically, two of the beam arrangements exhibited greater stiffness than the analytical prediction, while two were slightly less stiff, one of which measured 5% below the analytical value.

Table 6.10: Comparison of Analytical, 4-point and 3-point Bending Stiffness for Beams

Beam	Setup	Analytical bending (EI_{eff}) x10^{11} Nmm^2	4-point bending (EI_{eff}) x10^{11} Nmm^2	3-point bending (EI_{eff}) x10^{11} Nmm^2	%difference 4-point and 3-point
Beam A1	Y1 Y2	10.05	10.31	10.44	-1.25
Beam A2	Y6 Y4	9.99	10.18	9.48	6.92
Beam B1-1	X8X6X10X4	2.56	2.77	2.63	5.20
Beam B2-2	X7X1X3X2	2.58	2.71	2.56	5.50

Overall there is very close agreement between the analytical and experimental values. For each beam, the analytical stiffness is within a few percent of the experimental results (both 4- and 3-point). Beam A1 has its differences are on the order of 2–4%. Beam A2 has its differences in the 2–5% range. Beams B1-1 and B2-2 have their differences range from about 3–8%.

When comparing three-point and four-point bending tests, it is evident that the four-point configuration typically produces a higher estimated effective stiffness. This occurs because, in the three-point bending test, shear stiffness acts along the entire beam, leading to a slightly lower stiffness estimate. In contrast, the four-point bending test minimizes the influence of shear, thus resulting in a higher measurement. Nonetheless, the difference between three-point and four-point bending results is relatively small—usually less than about 7%. This indicates that both methods provide reasonably consistent stiffness values, although local effects (e.g., the concentrated load in three-point bending) can cause minor shifts in the measured results.

The analytical predictions appear reasonably accurate, matching the experimental data (both 3- and 4-point bending) within a small percentage. This lends confidence that the theoretical model used to calculate EI_{analytic} is sound.

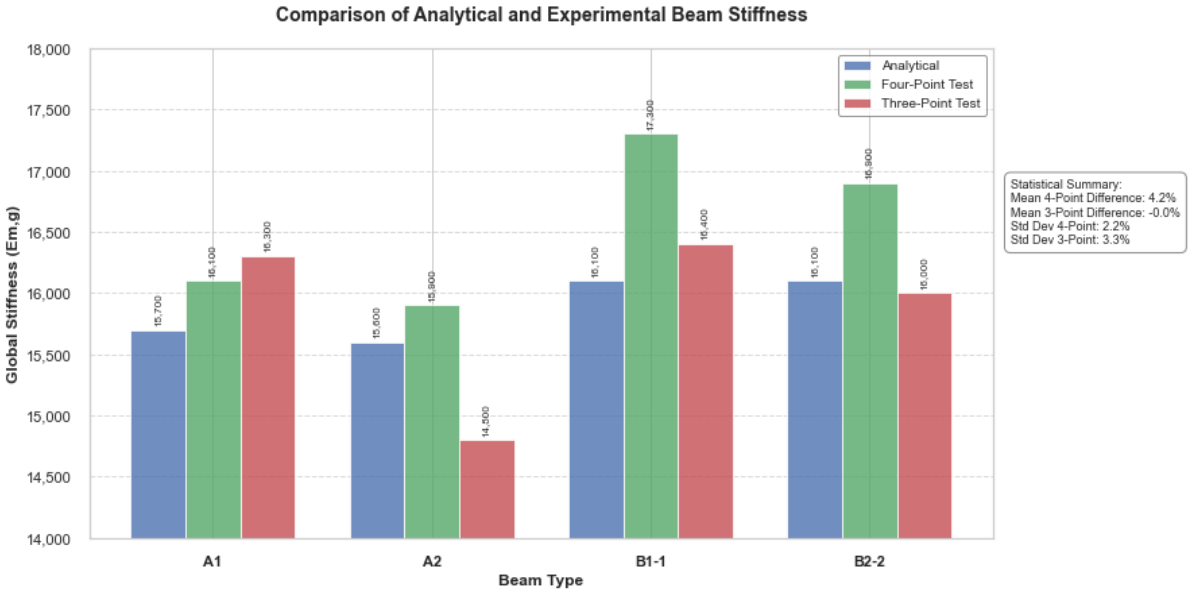

Beam	Four-Point Diff (%)	Three-Point Diff (%)
A1	2.5%	3.8%
A2	Percentage Differences from Analytical Values	-5.1%
B1-1	7.5%	1.9%
B2-2	5.0%	-0.6%

Figure 6.22: Global stiffness(analytical vs experimental)

In three of the cases, the 3-point stiffness is consistently lower than the 4-point stiffness with the exception of the first case, which can be attributed to experimental error. The difference between 3-point and 4-point bending test results is relatively small, typically less than about 7%. That suggests that both testing methods yield fairly consistent stiffness values, although local effects (e.g., load concentration in 3-point bending) can shift the measured results slightly.

6.9. Grading of the Timber Lamellas

6.9.1. Characteristic Density Determination

Characteristic density (ρ_k) is a key parameter for timber grading according to EN 384[18] and NEN-EN 14358 [40]standards. It is defined as the 5% fractile of the density distribution, representing the value that 95% of the population is expected to exceed. For moderate sample sizes, the characteristic density can be approximated using:

$$\rho_k \approx \bar{\rho} - k \times s \tag{6.19}$$

where:

- $\bar{\rho}$ = sample mean density,
- s = sample standard deviation (unbiased),
- k = fractile factor (typically $\sim$1.645 for 5% fractile with sufficiently large n; for smaller sample sizes, EN 14358[40] prescribes specific factors).

Based on the density values adjusted to 12% moisture content from our specimens, we obtain:

Mean density at 12% MC = 1061.4 kg/m^3

Standard deviation = 25.8 kg/m^3

5%-fractile $\rho_k = 1019.1\ kg/m^3$

The characteristic density at 12% MC is approximately 1,020–1,040 kg/m^3, which is exceptionally high compared to the density requirements in EN 338's hardwood strength classes. In the EN 338 of strength classes [2] qualifies all the timber for beyond D80 requirement as this requires requires a characteristic density of 900 kg/m^3, while our specimens significantly exceed this threshold.

6.9.2. Local MOE Values at 12% Moisture Content

The local modulus of elasticity (MOE) values adjusted to 12% moisture content provide another important parameter for strength class assignment. Table 6.2 presents the adjusted MOE_{Local} values for all specimens. the adjusted value at the MC 12% value can be directly used as the mean MOE in the strength class tables in the EN 338[2]

Statistical analysis of the adjusted MOE_{Local} values yields:

Mean MOE_{Local} (all samples)= 20,794 MPa

Mean MOE_{Local} (X samples)= 19,446 MPa

Mean MOE_{Local} (Y samples) = 23,042 MPa

taking the mean value of the local moe , the memebr sare then assigned a D70

6.9.3. Strength Class Assignment

According to EN 338[2], the strength classes of the wood are defined by a combination of characteristic values of the properties of strength, stiffness, and density. Table 6.11 shows how our specimens compare to the EN 338 hardwood strength classes in terms of both density and mean modulus of elasticity requirements.

Table 6.11: Comparison of Specimen Properties with EN 338 Hardwood Strength Classes

Strength Class	**Characteristic Density** ρ_k (kg/m^3)	**Mean Density** ρ_{mean} (kg/m^3)	**Mean MOE** $E_{0,mean}$ (MPa)	**Comparison**
D80	900	1080	24,000	
D70	800	960	20,000	Specimens exceed most
D60	700	840	17,000	requirements with
D50	620	740	14,000	$\rho_k \approx 1019\,\mathrm{kg/m^3}$,
D40	550	660	13,000	$\rho_{\mathrm{mean}} = 1061\,\mathrm{kg/m^3}$,
D35	540	650	12,000	$E_{0,\mathrm{mean}} = 20\,794\,\mathrm{MPa}$
D30	530	640	11,000	

The characteristic density ($\rho_k \approx 1019$ kg/m^3) is approximately 13% higher than the D70 requirement (900 kg/m^3). The mean MOE_{Local} at 12% MC (20,794 MPa) is approximately 4% higher than the D70 requirement (20,000 MPa).

The Y samples exhibit particularly high stiffness, with a mean MOE_{Local} of 23,042 MPa, exceeding the D75 of 22,000 Mpa requirement

The X samples, while still exhibiting high stiffness properties with a mean MOE_{Local} of 19,446 MPa, fall just below the D70 threshold but well above the D65 requirement of 18,500 MPa.

The analysis shows that the samples substantially exceed the EN338 [2] requirements for hardwood class D70 in terms of both density and modulus of elasticity. Unfortunately, the bending strength properties could not be readily determined.

These mechanical properties measured more than the given indicate that the Eurocode 338 [3] should revise the strength classes of the D sector upward, thereby enabling these woods to be appropriately graded and utilised by the industry.

7

Results and Discussions on Experiments on Mechanically Jointed Beams

The mechanically jointed beams were evaluated using both four-point and three-point bending tests, with the focus on the elastic behaviour of the dowelled beams. The experimental campaign commenced with a four-point bending test, during which two LVDTs were installed on the left side at 200 mm and 800 mm from a reference point. The test results confirmed that the beams remained within the elastic range, as predicted by theoretical analyses.

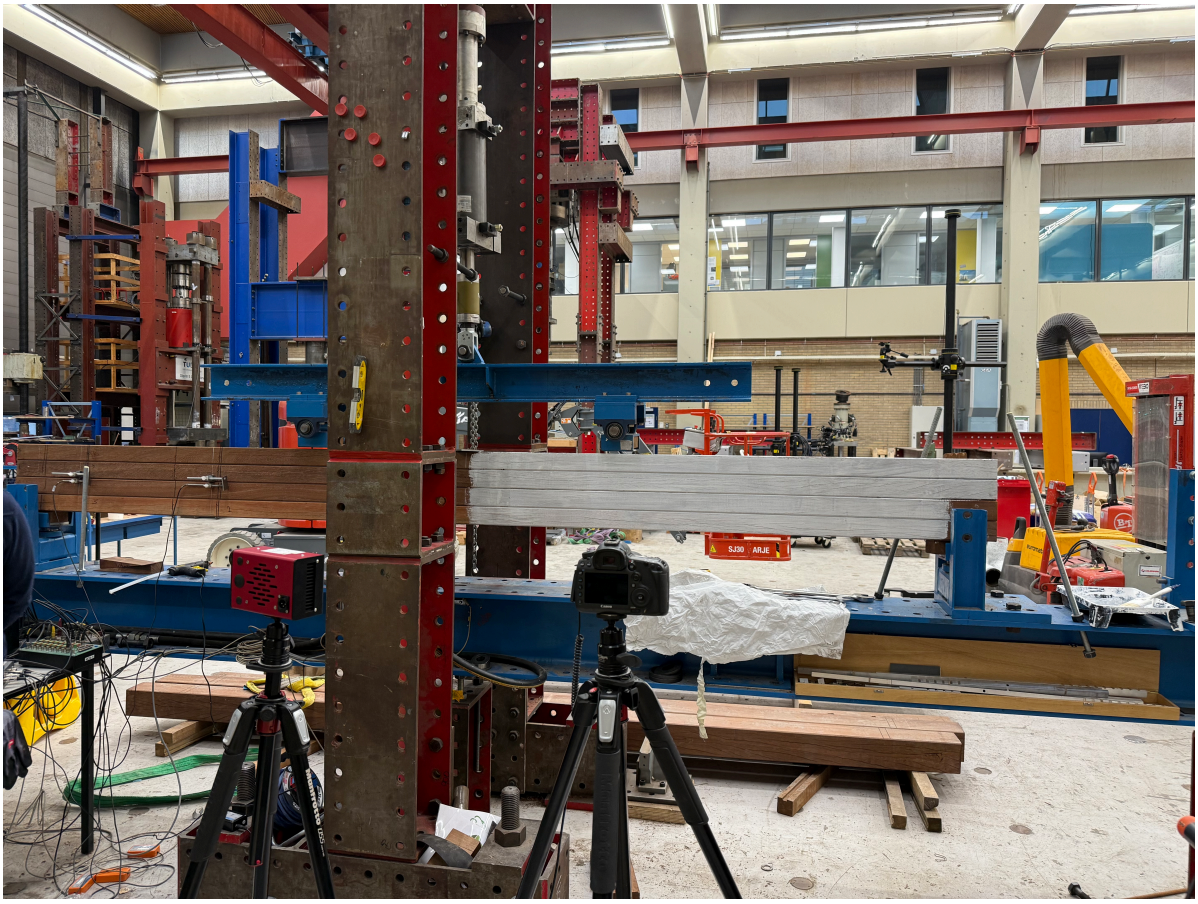

Figure 7.1: 4 point bending of dowelled beam B1-1

7.1. Four-Point Testing of Dowelled Beams in the Elastic Range

The deformation we predicted was quite off compared to the force we predicted. The beams were tested with a speed of 0.4 mm/s. And theEI_{eff}stiffness was calculated from the same formula we used for the individual beams

Table 7.1: Beam Test Results

Beam	**Max Force (kN)**	**Max Deflection (mm)**	**Loading Speed (mm/s)**	**Effective Stiffness ($\times 10^{12}$ Nmm^2)**
Beam A1	51.40	19.55	0.10	2.16
Beam A2	50.94	18.55	0.10	2.27
Beam B1-1	39.87	23.80	0.13	1.54
Beam B2-2	34.84	24.00	0.13	1.13

Its to note that in the post processing all the graphs remained in the elastic region but beam B1-1 showed slight plasticity for the given load and displacement

The loading speeds were in such away to have the test finished within a 3 - 5 minutes and the loading speed was calculated by dividing the expected displacement by 180s. The offloading stage was abit faster in all cases but increasing the speed by 1.5 times.

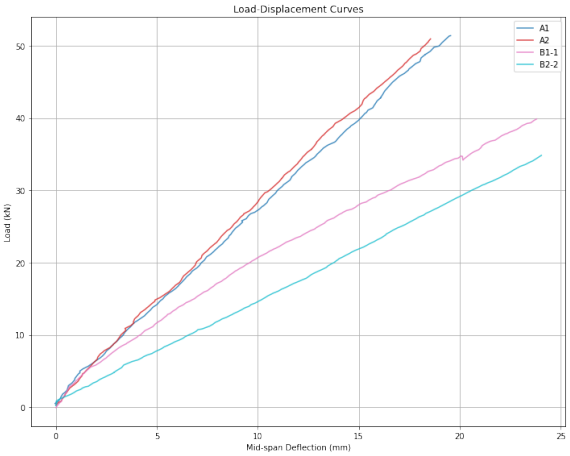

(a) 4-point bending stiffness of the dowelled beams (A1, A2, B1-1, B2-2).

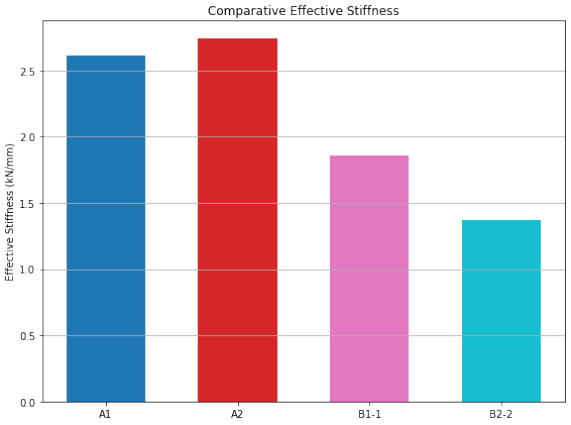

(b) Comparative stiffness of the dowelled beams in 4-point bending.

Figure 7.2: Comparison of stiffness characteristics of dowelled beams under 4-point bending.

As anticipated, beams A1 and A2 exhibited substantially higher effective stiffness compared to B1-1 and B2-2. This outcome corresponds to the expected decrease in stiffness that results from further bisecting cross sections, as was done with the stacked configurations. Additionally, the greater effective stiffness observed relative to the stacked beams confirms that composite action is taking place.

Beam B1-1 began to exhibit plastic behaviour at an early stage, despite having a higher stiffness than B2-2. Upon visual inspection, a crack was identified running along the grain between two staggered dowels, which may explain the onset of plastic behaviour. Although the nearest dowel was located 400 mm away—significantly more than the recommended minimum spacing of 7d (i.e., 140 mm)—the crack still formed. The staggered positioning of the dowels probably mitigated a more extensive split by restricting the propagation of the crack across the beam. The damage appears to have originated before testing, possibly during the hammering of dowels into the lamellas, showing the importance of thorough inspections of such defects immediately after fabrication. The edge distances are indeed correct / verified, but during manufacturing care has to be placed so as not to induce cracks.

Figure 7.3: dowelled beam B1-1 with running cracks from the dowel holes

7.1.1. Interlayer Slip at the Interface

Interlayer slip between the composite beam's layers was monitored using LVDTs at the interface. Transducers were placed at distances of 200 mm, 800 mm, and 1400 mm from the support along the beam length (corresponding to near one support, mid-span, and near the other support, respectively). These gauges captured the relative displacement (slip) between the top and bottom layers at those locations.

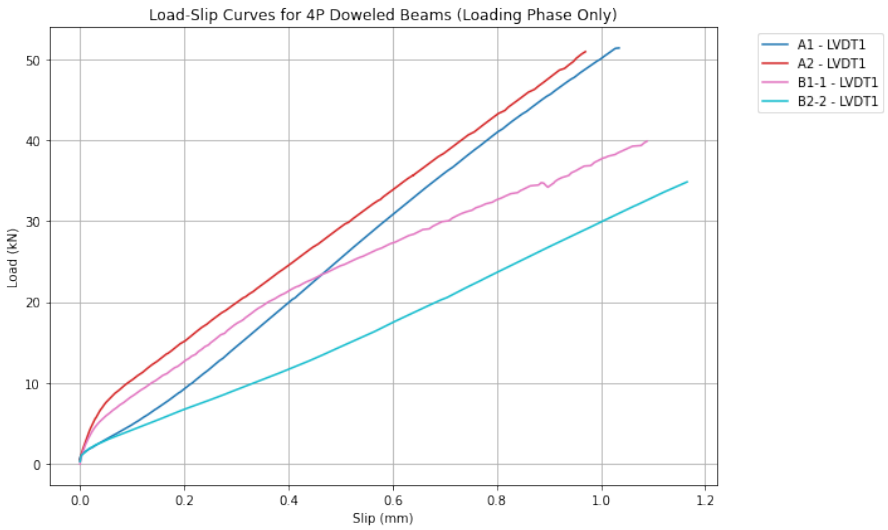

Figure 7.4: The load-slip displacement curve from LVDT1 (located at 200 mm from the support) for various beams.

Beams A1 (blue line) and A2 (red line) both demonstrate much higher stiffness and composite action, reaching higher loads for the same slip values. However, beam A2 initially shows a steeper linear slope, indicating a higher initial stiffness and greater composite action compared to A1. *(Investigate the cause of this initial resistance.)*

Beam A1 exhibits a more linear trend from the start and eventually catches up with A2 at higher loads.

Beam B1-1 (pink line) Displays a trend similar to beam A2, but with a gradual change in slope, indicating moderate performance compared to the two-lamella beams. A small irregularity in the curve is attributed to a brief stop during the experiment.

Beam B2-2 (cyan line) Demonstrates the lowest stiffness with a nearly linear load-slip relationship after initial settling, similar in trend to beam A1.

All beams exhibit initial nonlinear behaviour in the 0–10 kN range, representing the initial engagement of the mechanical connections. Beyond this range, the curves become more linear, reflecting effective composite action.

The differences between the curves are more pronounced at higher loads, suggesting that the efficiency of load transfer mechanisms becomes increasingly critical as the loading increases. The two-lamella beams (A1 and A2) outperform the four-lamella beams (B1-1 and B2-2) in terms of absolute stiffness, although all beams show good structural performance.

The graph indicates that the dowelled connections facilitate significant load transfer while permitting controlled slip at the interfaces.

It should be noted that the observed slip is of the order of only 1 mm, even at high forces, showing the excellent composite action of the beams.

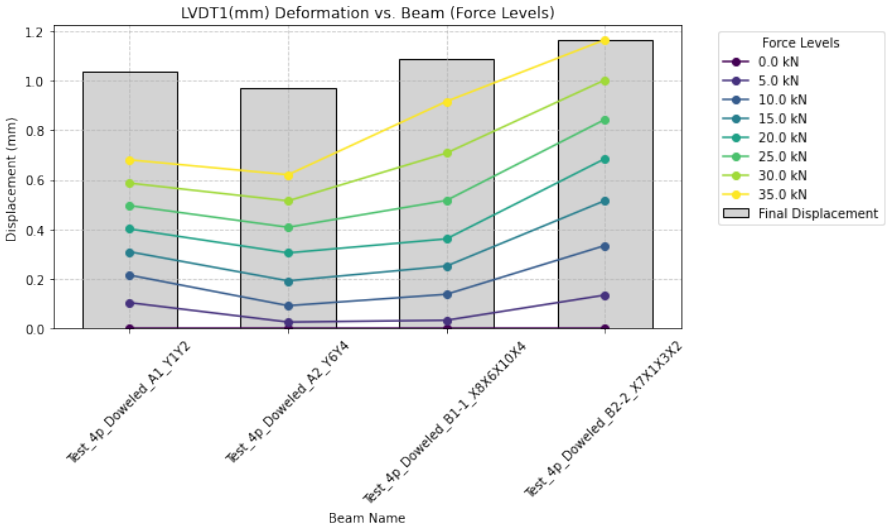

Figure 7.5: Enter Caption

When a bar chart depicting the deformation measured by LVDT1 under various applied forces is examined, the differences in displacement among the beams become more apparent. It is crucial to note that a positive slip denotes relative sliding between the layers when loaded, and its magnitude reflects the strength of the shear interaction within the beams. However, other factors—such as the stiffness of individual beam layers—also influence these measurements, so any direct comparison should take these variables into account.

Overall, the least stiff beam (B2-2) exhibited the highest rate of slip between its center lamella. In fact, the slip in the B-type beams was approximately 41% greater than that observed in the A-type beams. Moreover, the slip in beam B2-2 developed much more rapidly at different force levels compared to the other beams. This behaviour raises questions about whether the observed deformation can be attributed solely to the applied force and beam properties or whether additional factors also play a significant role.

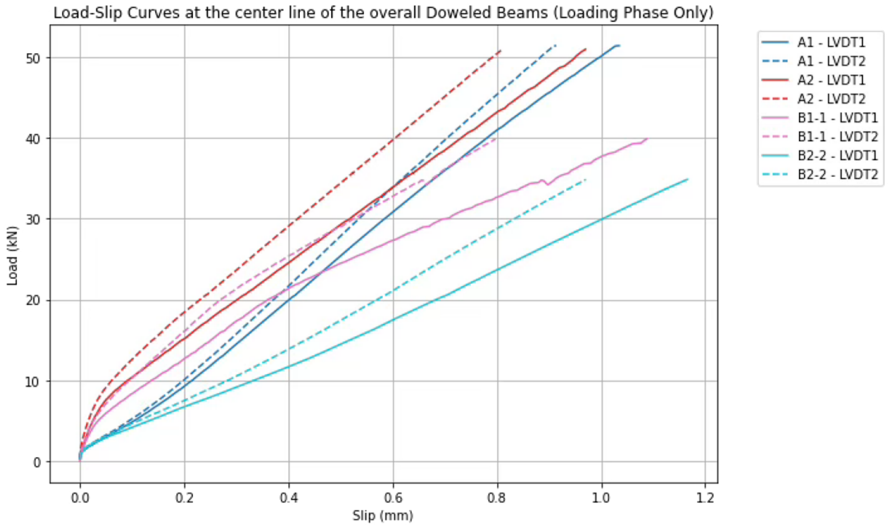

Figure 7.6: Comparison of LVDT1 and LVDT2 displacement measurements for beams A1, A2, B1-1, and B2-2 under varying load levels

When examining the LVDT2 measurements, a similar overall trend is observed. Although the displacement slopes appear somewhat higher, this can be attributed to the increased resistance encountered near the beam's center, where zero slip is expected.

7.2. Three point testing of the dowelled beams in elastic range

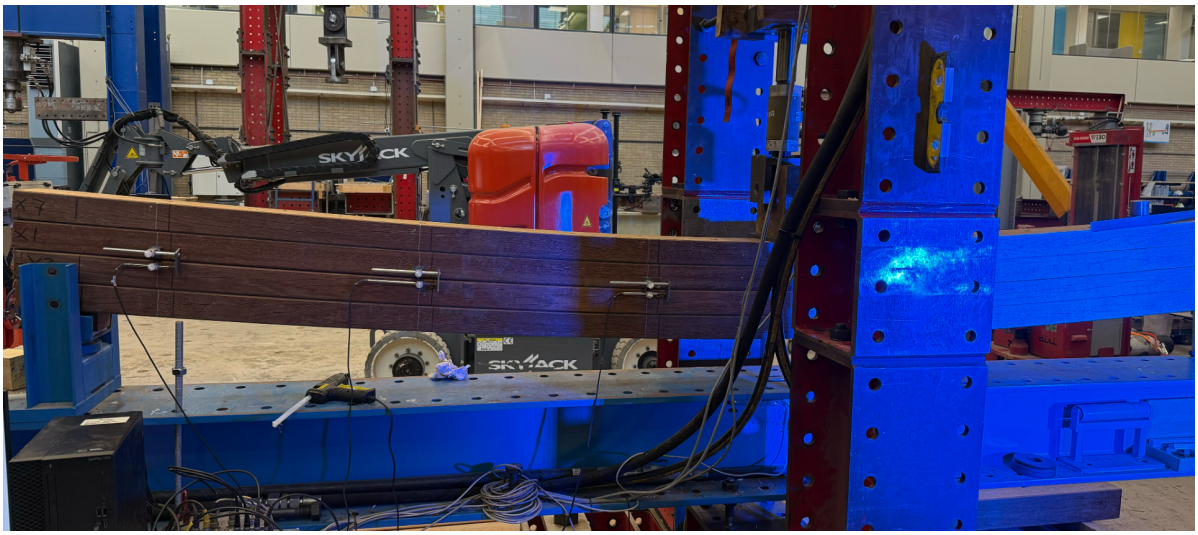

Figure 7.7: Experimental setup for a multi-layer composite beam test. LVDT sensors are attached at various layers to measure displacement and slip under loading, allowing assessment of shear interaction and overall bending response.

The test setup was arranged similarly to the four-point bending configuration, but with the addition of a third LVDT positioned 140,mm from the nearest support. Digital Image Correlation (DIC) was performed on the opposite side of the beams to capture full-field strain measurements. The beams were tested at speeds comparable to the four-point bending tests, ensuring the deformation rates remained consistent.

Table 7.2: Summary of Beam Test Results

Beam	**Max Force Reached (kN)**	**Max Deflection Reached (mm)**	**Loading Speed (mm/s)**	**Effective Stiffness EI_{eff} ($\times 10^{12}$ Nmm^2)**
A1	26.77	11.94	0.1	1.81
A2	34.08	14.46	0.1	2.17
B1-1	21.82	16.84	0.1	1.15
B2-2	20.20	17.40	0.1	1.07

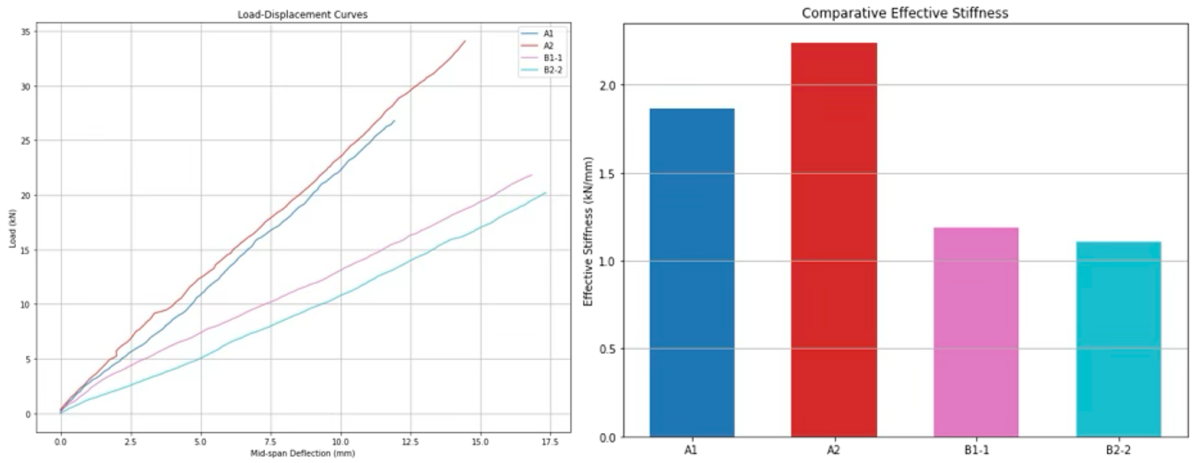

Figure 7.8: (Left) Load–displacement responses for beams A1, A2, B1-1, and B2-2 in 3 point bending, illustrating the varying stiffness and deformation behaviour.(Right) Comparison of effective stiffness among the same beams in bar-chart form.

Just as observed under four-point bending, the three-point load–displacement curves exhibit similar slopes among all tested beams, including a slight plastic response in beam B1-1. Beams A1 and A2 demonstrate substantially higher stiffness compared to B1-1 and B2-2: their initial load–deflection slopes (effective bending stiffness) are approximately an order of magnitude greater than those of the B-series beams. The Table and bar graph above summarize these stiffness values for comparative purposes.

The graph belowillustrates the load–slip relationships for four mechanically jointed azobe beams (A1, A2, B1-1, and B2-2) measured at the beam neutral axis during 3 point bending. Displacements were recorded 200,mm, 800,mm, and 1400,mm from the nearest support, thereby capturing the progression of slip between lamella interfaces: specifically, between the two lamellas in A1 and A2, and between the second and third lamella in B1-1 and B2-2.

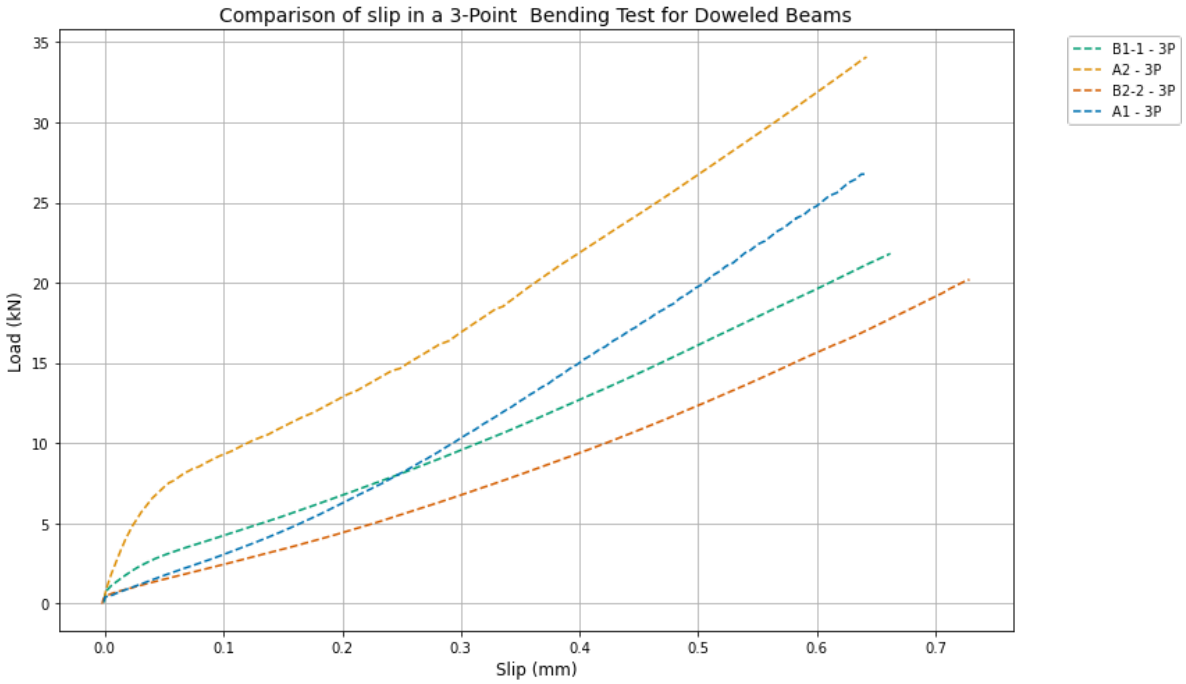

Figure 7.9: The load-slip displacement curve from LVDT1 in 3 point bending (located at 200 mm from the support) for various beams

Beam A2 (red line) exhibits the highest initial slip resistance, transitioning to a nearly linear trend over most of the load range. This behaviour mirrors the results from the four-point tests, showing both the beam's superior stiffness and its higher load-carrying capacity compared to the other beams.

Beam A1 (blue line):Displays an initially linear load–slip relationship, rapidly increasing in resistance to slip and eventually surpassing the slope of B1-1. This indicates early engagement of the dowels and enhanced composite action. After the initial non-linear phase, A1 attains a slope comparable to A2, albeit with greater overall slip.

Beam B1-1 (pink line) Shows a relatively high initial resistance to slip, then transitions to a more gradual stiffness increase as loading progresses. This response suggests that significant composite action occurs once the dowels reach a certain engagement force, thereby elevating slip resistance.

Beam B2-2 (cyan line) Possesses the lowest stiffness and slip resistance of all tested beams. Nonetheless, its slip response remains consistent, implying that composite action was present from the outset—likely reflecting a well-fitted dowel assembly.

All beams display some degree of non-linear behaviour, particularly noticeable in the initial loading phase. This non-linearity is likely due to initial settlement of the mechanical joints and engagement of the dowels. After this initial phase, the curves become more linear, indicating that the interface connections are fully engaged.

The significant differences between the two-lamella beams (A1, A2) and the four-lamella beams (B1-1, B2-2) suggest that the composite action is more effective in the simpler two-lamella configuration. This might be related to the efficiency of the mechanical connections and load transfer mechanisms between multiple interfaces in the four-lamella beam .

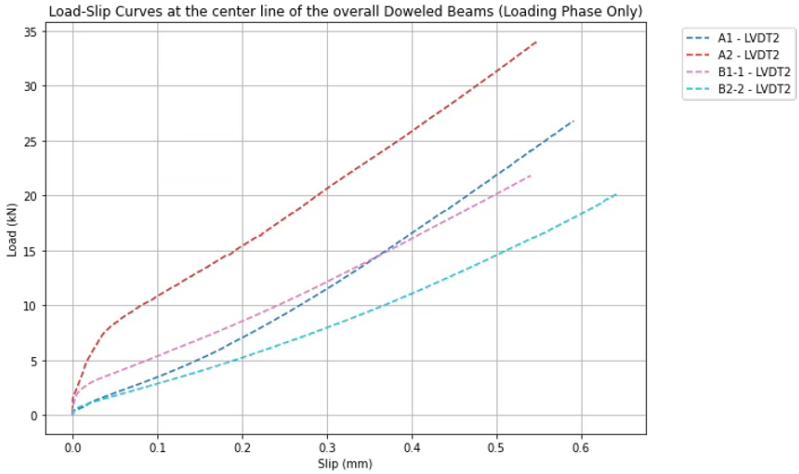

(a) The load-slip displacement curve from LVDT 2 (located at 800 mm from the support) for various beams

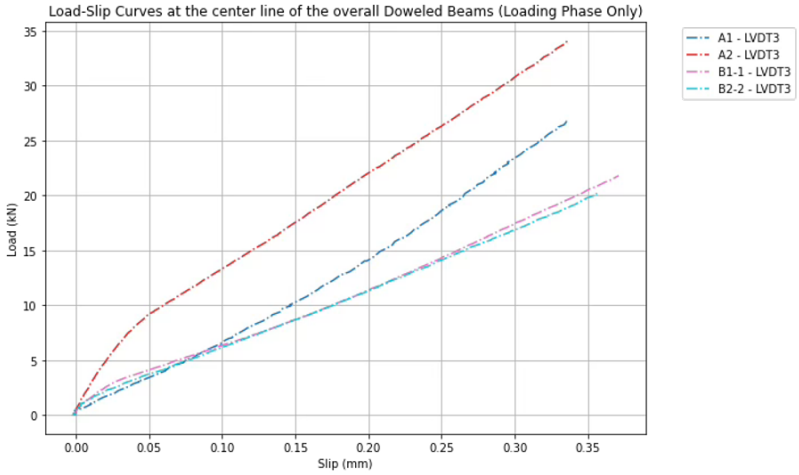

(b) The load-slip displacement curve from LVDT 3 (located at 1400 mm from the support) for various beams

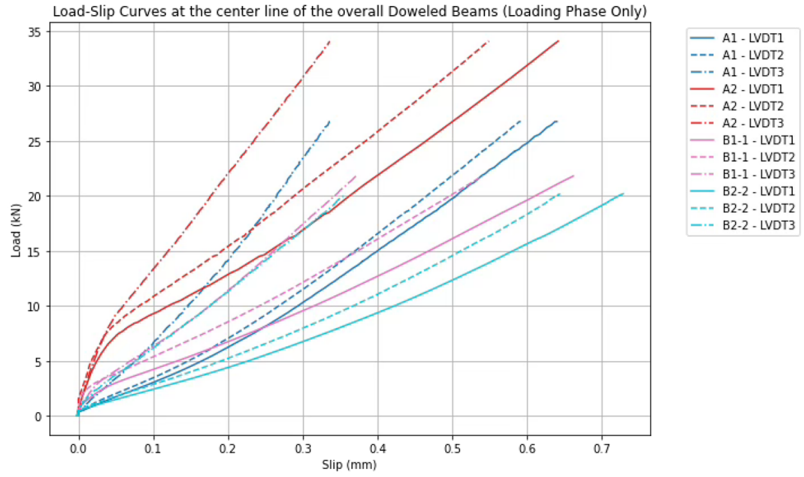

Figure 7.10: The load-slip displacement curve from LVDT 1,2 and 3 (located at 200, 800 and 1400 mm from the support) for various beams

When the slip is observed in the different areas LVDT1, LVDT2, and LVDT3, it is worth noting that the trends are quite similar and follow the same pattern. This confirms the action

explained along the beam.

7.2.1. Comparison of the 3-point and 4-Point Bending test Results in the elastic range

As expected, the beams exhibited higher stiffness under four-point bending than under three-point bending. As shown by the dotted lines in the plot, all of the beams were effectively stiffer when the load was applied at two points rather than one. In a four-point test, the mid-span experiences a constant moment region without shear, so the beam is less influenced by shear forces and behaves closer to a fully composite section over a larger portion of its length. This confirms that loading conditions do affect the overall stiffness of the beam.

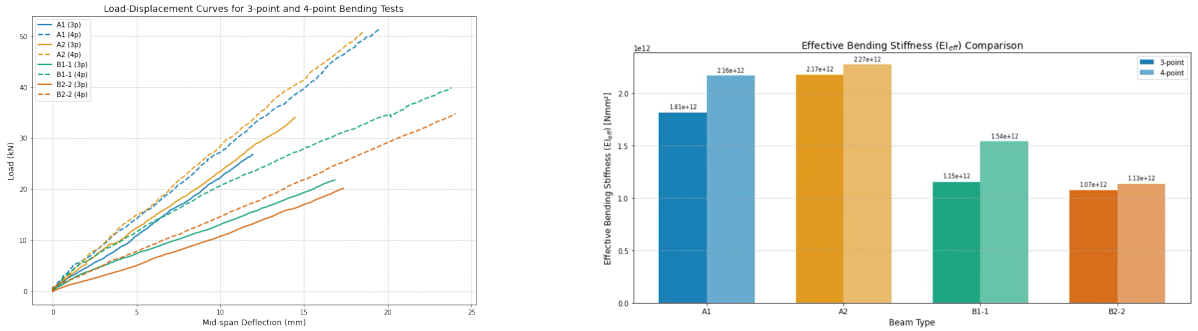

(a) Slip Distribution Under 3-Point Bending

(b) Slip Distribution Under 4-Point Bending

Figure 7.11: Comparison of Slip Distribution Under 3-Point and 4-Point Bending

The four-point tests reached higher load levels compared to the three-point tests. For example, the initial stiffness of beam A1 rose from 1.81 $\times$ 10^{12}Nmm^2 in the three-point test to 2.16 $\times$ 10^{12}Nmm^2 under four-point loading, as shown in the bar graph. Even the more flexible beam B2-2 showed an increase from 1.07 $\times$ 10^{12}Nmm^2 to 1.13 $\times$ 10^{12}Nmm^2. Among all beams tested, the percentage increase ranged from 4.4% (A2) up to 25% (B1-1). Beam A1 and B2-2 showed 16% and 5% increases, respectively, while A1 and B1-1 exhibited the largest overall changes.

7.2.2. Slip comparisons in the dowelled beams between the 4points and 3points bending tests

A quick look at the load–displacement graphs reveals a striking contrast in slip behaviour when the beams are tested under 3-point versus 4-point bending. In the 3-point setup, the shear force extends throughout half the beam's length, causing the slip to accumulate steadily from the supports toward the middle of the span and resulting in greater slip magnitudes near the centre. In contrast, the four-point configuration features a constant moment region between the load points, which means there is minimal shear through the middle of the beam. Consequently, slip develops primarily near the supports, with little additional movement between layers beyond the loading points. These observations underscore how loading conditions shape stress distributions in mechanically doweled beams: 3-point bending concentrates slip in the mid-span, while 4-point bending confines it to the outer spans, leading to more uniform behaviour in the centre.

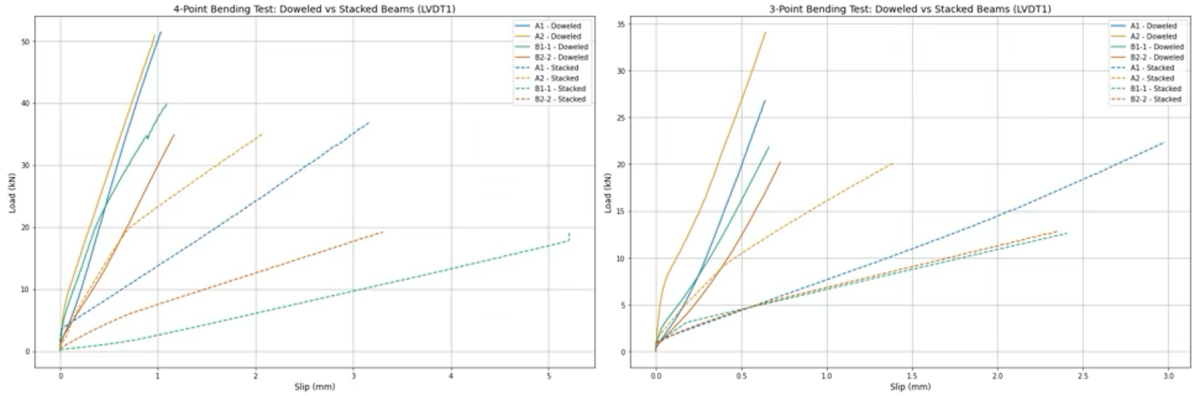

Figure 7.12: slip comparisons between dowelled and stacked beams at four point and 3 point loading in the LVDT 1 position

Comparisons among stacked beams reveal intriguing behaviour in specimens A1 and A2, with A1 in particular exhibiting a pronounced stick–slip pattern. The dowels appear to amplify the slip response at lower loads but delay more significant displacement until relatively high load levels. In most cases, this indicates that the mechanical action of the dowels enhances load transfer by limiting the movement of the interlayer until the beam is subjected to higher forces.

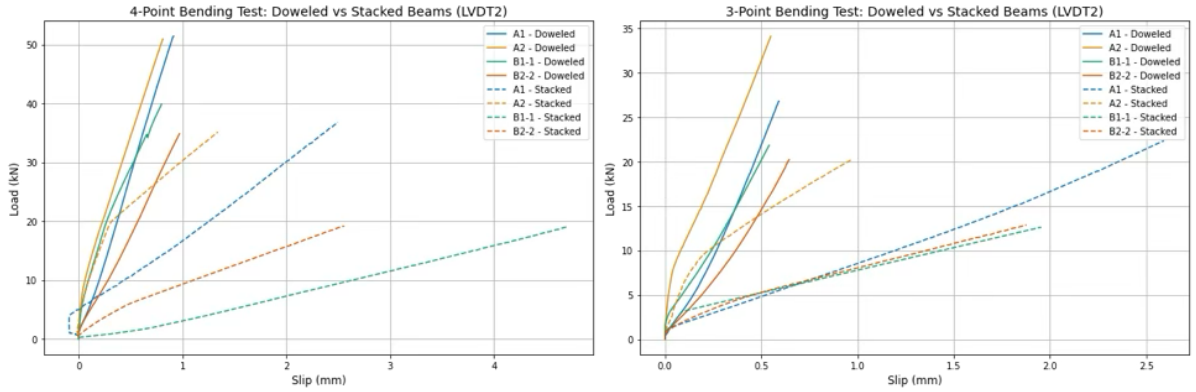

Figure 7.13: slip comparisons between dowelled and stacked beams at four point and 3 point loading in the LVDT 2 position

When examining the LVDT2 results, the trend line for the A2 stacked beam aligns closely with that of the doweled beam at lower load levels. However, as the applied force increases, the response of the stacked beam changes to a more distinct and linear slope. This behaviour is potentially influenced by friction at the interfaces, which can dominate in the initial stages of loading. A similar pattern is also observed in other stacked beam specimens, reinforcing the hypothesis that friction significantly affects the early load-transfer mechanism in stacked configurations.

Conclusions

The A beams consistently show smaller deflections and slip at a given load compared to the B beam, in both loading configurations. Meanwhile, for a given beam, 4-point bending tends to produce slightly smaller deflections and slips than 3-point bending at the same total load, because the load is distributed (reducing shear and deflection in the centre).

These trends can be visualised by comparing load–deflection curves or load–slip curves for the different tests. For instance, if we plot load vs. mid-span deflection for all beams, the curves for A1 and A2 would lie much steeper (stiffer) than B1 and B2. Likewise, plotting load vs. end-slip would show B beams accumulating slip much faster with load than A beams. At around 20–25 kN, B-type beams already have a slip on the order of 5–10 mm slip, whereas A-type might only be 1 mm.

7.3. Loading to 100 KN in 3-Point Bending

In these tests, all four dowelled beams, A1, A2, B1-1 and B2-2, were loaded to approximately 97-100kN using a 3-point bending set-up. Although failure was not anticipated, the beams did not reach full collapse at that load level. Two principal failure mechanisms were considered: 1. Brittle Failure Occurs when the lowest lamella ruptures due to tensile stresses that exceed the bending strength of the wood. 2. Ductile Failure Involves the steel dowels yielding in shear and allowing significant interlayer slip, indicating extensive plastic deformation within the connection

To push a beam to its ultimate bending failure, it must first reach a sufficiently high load level. As predicted by analytical estimates, this was still insufficient to achieve ultimate failure, although each beam displayed subtle differences in behaviour.

For most of the loading range (up to around 80 kN), the two A series beams performed very similarly, which shows the consistency in their manufacture and assembly. The beams of the B series also exhibited comparable load-deflection characteristics, except for a noticeable quirk in beam B1-1 (discussed further on). In general, the flexural strength of the timber governed the ultimate capacity in this 3-point setup, rather than the dowels themselves. Even the more flexible and slip-prone B series achieved the full potential of the timber section predicted by the gamma factors, indicating that the dowel connections effectively transferred shear between layers.

The larger deflections observed in the B series did not decrease the maximum load. Instead, these beams simply reached the same maximum capacity with greater deformation, a testament to their partial composite action, where sufficient connectors were present to develop nearly full bending strength.

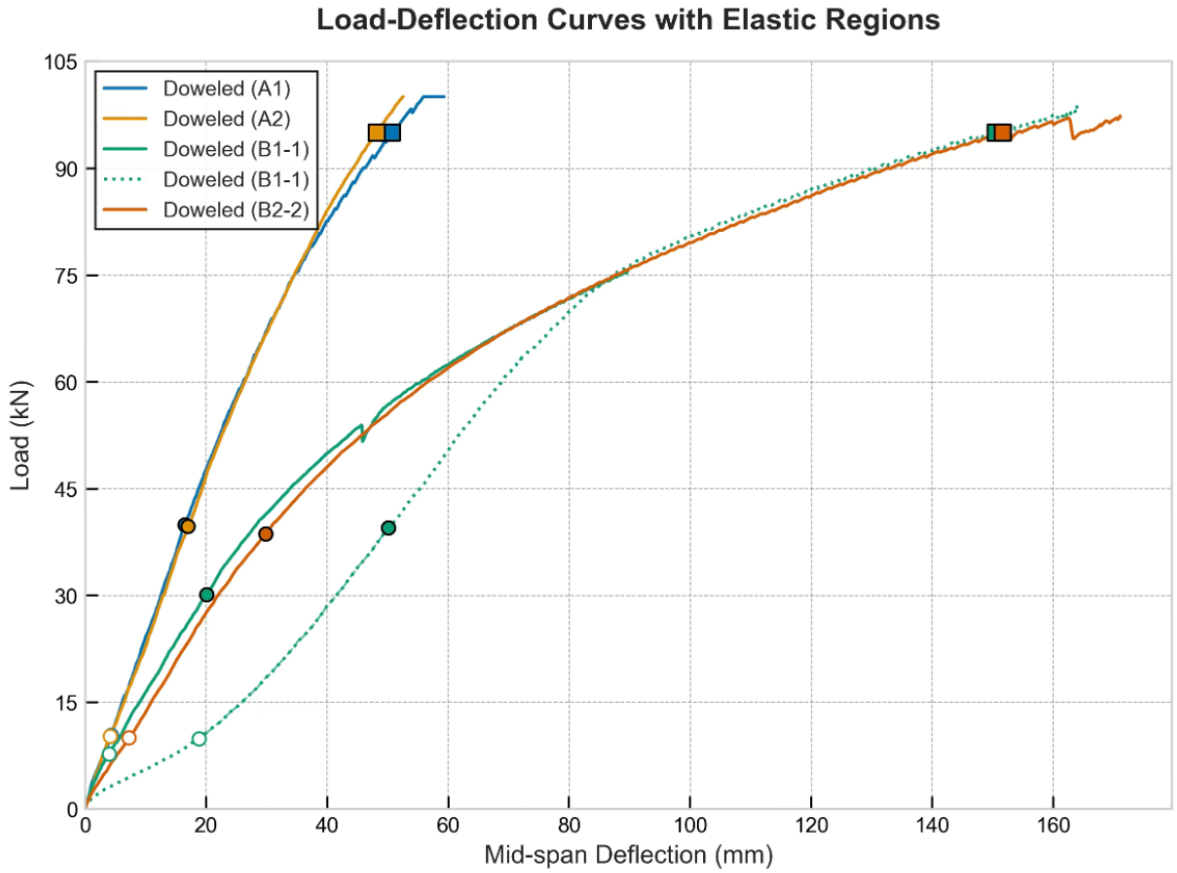

Figure 7.14: Load deflection curve to the 100KN mark

Beam A1 began to show early signs of distress around 80kN, but managed to carry loads beyond 100kN. The primary failure mechanism involved a tensile crack in the bottom lamella, running perpendicular to the grain. In contrast, A2 reached approximately 100.1 kN without any visible signs of impending failure - its test was simply limited by the available load capacity.

Both B1-1 and B2-2 reached around 97–98kN. Although B2-2 showed an angled fracture that followed the grain in the bottom lamella, the beam did not fully fail; instead, its stiffness briefly rebounded once the jack reached its maximum stroke. These observations suggest that, under 3-point bending, the dowel connections were sufficiently robust that none of the beams experienced connector failure. Instead, tensile stresses in the laminations governed the ultimate capacity.

Significantly, a multilayer beam (for example, B2-2) can reach the same peak load as a stiffer configuration (e.g., A2) despite exhibiting larger deflections and therefore poorer serviceability performance. Monitoring the evolution of the stiffness confirmed a gradual reduction with increasing deformation, forming a non-linear trend that approached near-zero slope at higher loads. However, in beam A1, the near-flat slope after 100 kN reflected the force limit of the test equipment rather than the true zero stiffness.

A similar anomaly occurred in B1-1, whose initial test used a jack with insufficient travel. Once repeated with a longer stroke jack (shown by a dotted line), the beam displayed a lower initial stiffness but converged with the original stiffness trend near 75 kN, then matching the slope of B2-2.

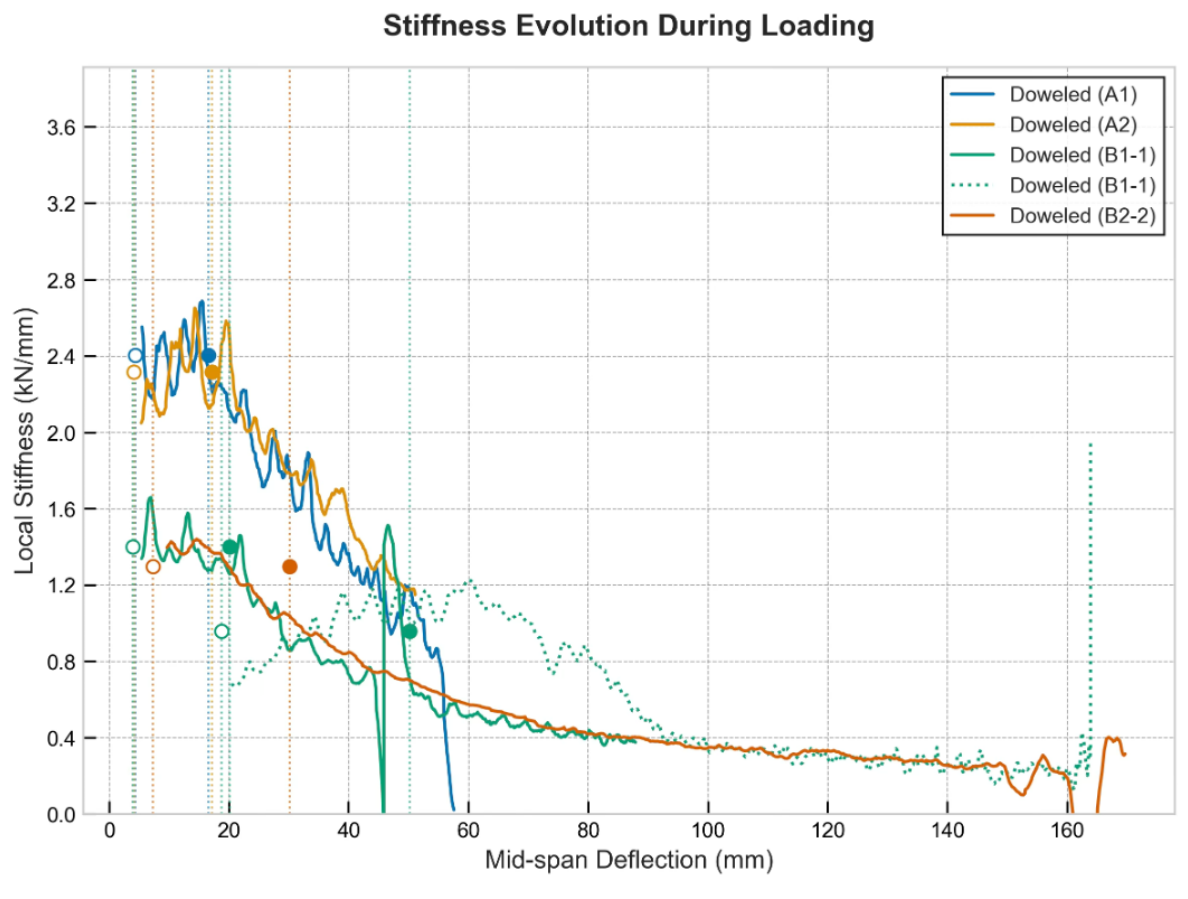

Figure 7.15: Stiffness evolution of the beams

By plotting the local slope of the load-deflection curve (that is, stiffness) against mid-span deflection, it can be visualised how the beam's capacity to resist additional deformation diminishes as it nears failure. Initially, the slope remains relatively high, reflecting stiffer behaviour. However, as failure accumulates under increasing loads, the slope steadily declines, indicating a progressive loss of stiffness until it approaches near zero at the ultimate failure. Once local failure occurs, it can regain a bit of its stiffness as this graph is based on a simple slope and is not a true predictor of failure.

7.4. DIC Technology

The DIC (Digital Image Correlation) technology was also used to compare the results from the lvdts because it could give more information on not just horizontal deformations but vertical ones as well. Unlike LVDTs, which are typically installed with a slight vertical offset from the metal reference surface and provide only linear measurements, DIC allowed measurements at points located closer to the interface between the lamellas. This proximity can reduce errors that arise as the beam curvature changes and LVDT readings become less accurate. Essentially, while LVDTs only capture linear displacements, there is a lot of advantages of setting up a DIC to track the movements of a random speckle pattern on the beam's surface through sequential images taken before and after deformation, thereby offering full-field displacement and strain data.

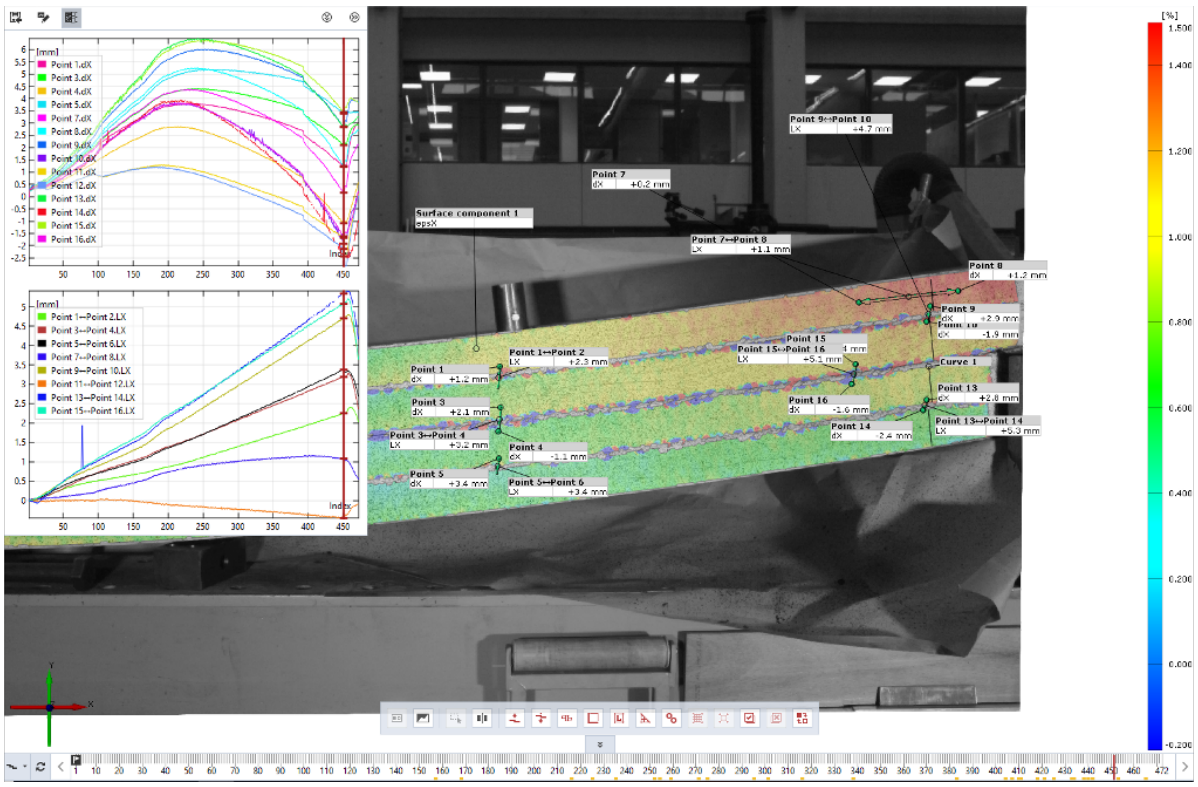

Figure 7.16: Horizontal strain fields captured via Digital Image Correlation (DIC) in the tested beam, illustrating the localized deformation in the x-direction at multiple points along the lamella interface.

The color-coded strainlike distribution map and its accompanying plots provide a comprehensive depiction of the deformation behaviour of the beam and its multiple layers under load. This approach offers improved accuracy compared to traditional LVDT (Linear Variable Differential Transformer) measurements by capturing full-field displacement and strain responses rather than merely recording linear displacements.

The analysis was done in the Zeiss Correlate software. Points were selected on each lamella along a vertical line—approximately 250mm and 1000mm from the support and at additional distances like at 300mm. The relative distances between these points were recorded and compared at various time intervals. The top graph illustrates the relative displacement of these points from their original positions. In the graph below, relative movement between the adjacent points are recorded. This is usually a difference calculation of the values recorded by the points.

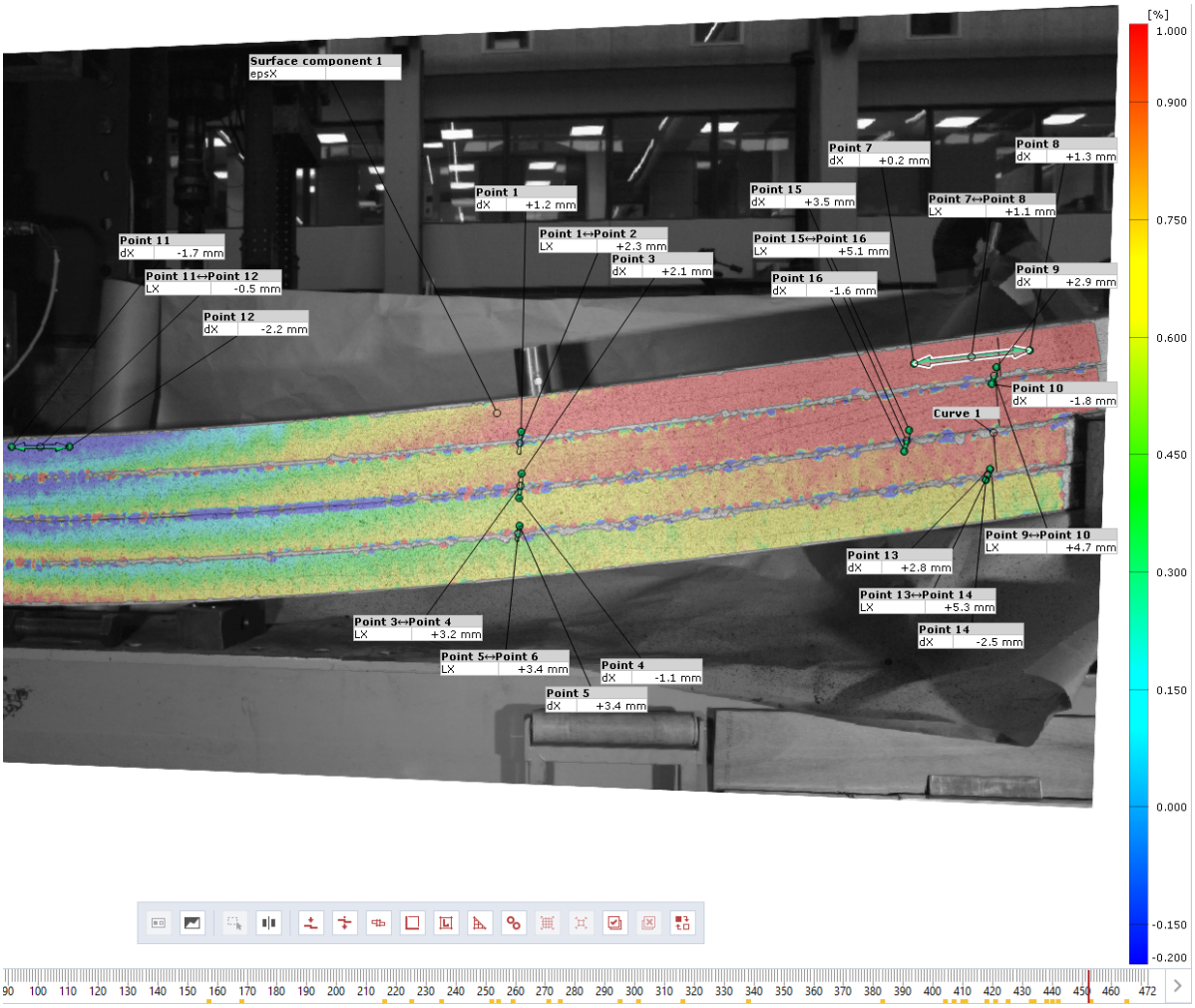

Figure 7.17: Illustration of the x-direction displacement field obtained using DIC software, showing the relative movement of selected points along the beam surface

Ideally, the displacement should increase linearly till the maximum load, as observed in the initial portion of the top graph. However, the latter half of the graph reveals diminished deformation, indicating the presence of rigid-body movement. This effect causes the points located further back to move in the opposite direction, thereby introducing inconsistencies in the readings provided by the LVDTs. as the beam moves downwards with the deformation and all parts rotate differently as well.

Specifically, points 15 and 16 in the figure above, located approximately 300mm from the support, exhibited a relative movement of 5.1mm and points while points 3 and 4 located 1000mm from the support recorded a maximum value of 3.2mm . In contrast, LVDT 1, located roughly 200mm from the support, measured a relative inter-layer displacement of 8.456mm and LVDT 2, positioned about 800mm from the support—recorded a displacement of 7.17mm. Both showing higher values than those indicated by the DIC. While the locations of the measurement points for the DIC and LVDTs aren't exactly identical (with the DIC points being at 300mm and 1000mm and the LVDTs at 200mm and 800mm, respectively), these values show that the DIC system underestimates the displacement by approximately 40–55% compared to the LVDTs

The table below presents the maximum slip values recorded by the LVDTs during the peak

load conditions. The sensors are positioned at specific distances from the support: LVDT1 is located 200 mm from the support, LVDT2 at 800 mm, and LVDT3 at 1400 mm.

Table 7.3: LVDT Slip Measurements for the Jointed Azobe Beams

	A-Series (Large Cross-Section)		**B-Series (Small Cross-Section)**	
	A1	**A2**	**B1-1**	**B2-2**
Max Load (kN)	100	100	99	97
LVDT1 Max Slip (mm)	3.49	3.16	8.46	8.44
LVDT2 Max Slip (mm)	3.81	2.69	7.17	7.15
LVDT3 Max Slip (mm)	1.94	1.51	4.08	4.02

In summary, the DIC analysis using Zeiss Correlate effectively captures the beam's relative horizontal movement but falls short in accurately quantifying the deformation values along that axis. The displacement values obtained at specific points do not fully match the LVDT measurements, likely due to distortions introduced by rigid body motion. On the other hand, the software may consistently capture the vertical displacement at the beam's center as only rigid body movement should be recorded there indicating that while DIC offers more data to work with, it may need further calibration for the stacked beam analysis or complementary methods to match the precision of traditional LVDT measurements.

7.5. Revisit of the bending strength of the beam lamellas

Figure 7.18: Beam A3 after failure

Initially, it was hypothesized that if the classification were solely based on density, all lamellas would exceed D80, and the mean modulus of elasticity (MOE) would be the decisive factor. Fortunately, a third pair of y lamellas, y5 and y3, were stacked to construct stacked beam A3, which was subjected to failure testing. Subsequently, using this equation, the bending strength of beam A3 was determined through a three-point bending test.

$$f_m = \frac{3\left(\frac{F_{\max}}{2}\right)L}{2\,b\,h^2} = \frac{3\,F_{\max}\,L}{4\,b\,h^2}. \tag{7.1}$$

It was discovered that the bending strength of each lamella is 86 MPa. However, unfortunately, without using more samples which were not readily available, thus the characteristic bending strength of lamellas Y5 and Y6 could not be deduced in order to grade their bending strength.

In comparison to the stacked beams of A1 and A2, which were subjected to elastic range testing in the same three-point test, it was observed that the slopes were remarkably similar. This observation suggests that the bending strength of the stacked beam may be comparable but often this isnt the case.

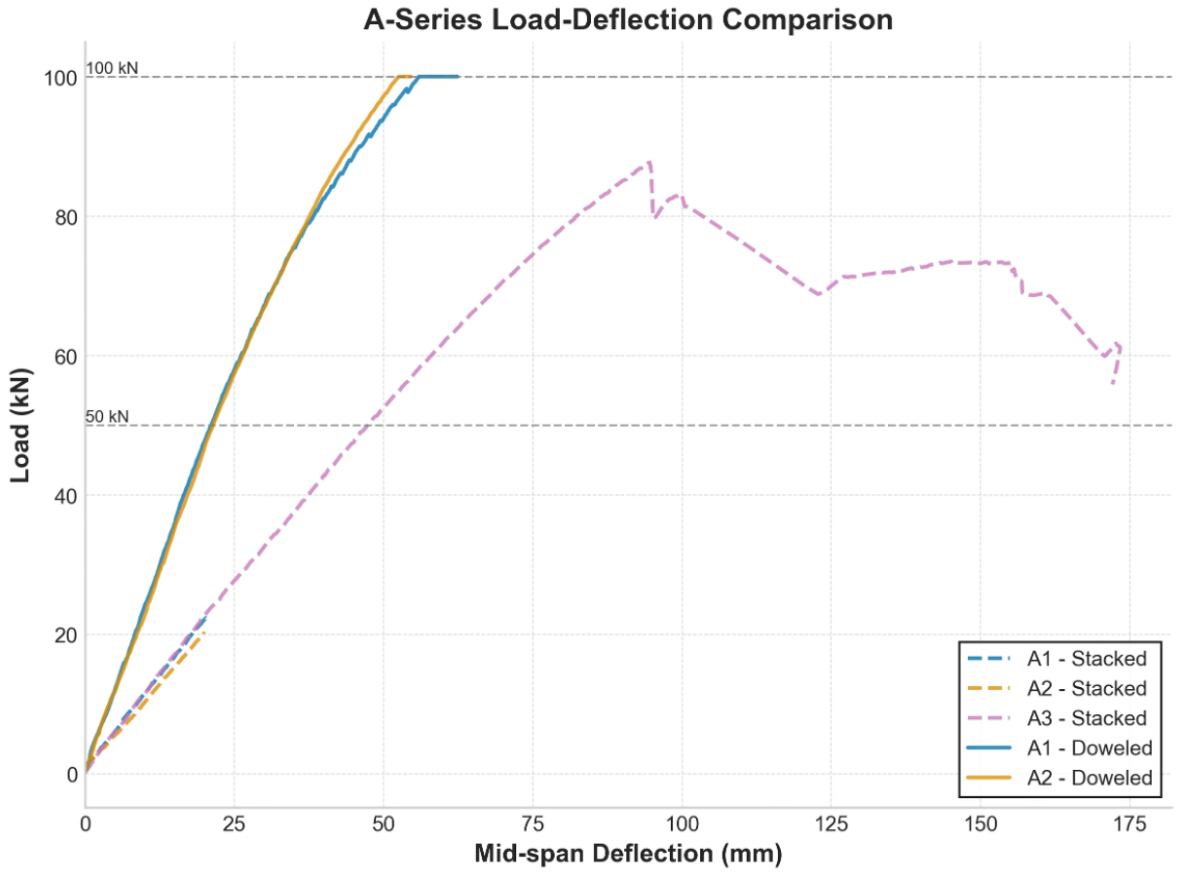

Figure 7.19: A series load deflection comparison

The stacked beam A3 also showed lower slope and breaking stress than the dowelled beams with composite action.

A final word on the failure Modes seen in 3-Point Bending Tests on all the mechanically jointed Beams

Tensile rupture of wood - Three of the beams ultimately exhibited or approached tensile failure in the wood (bottom fibre cracking) once the bending moment capacity was reached. This is the natural failure mode for a bending lamella at 100kN. The final drop in load in B1-1 and B2-2 also suggests a possible timber fracture. However, because of the dowel connectors, timber rupture was not sudden – the beams did not snap immediately when the first crack formed. Instead, other mechanisms kicked in to provide reserve capacity, and often times there was hope of regaining the lost stiffness.

Figure 7.20: Beam B2-2 exhibiting cracks in failure, with rupture at the bottom

Interlayer Slip – Beams B1-1 and B2-2 showed extensive interlayer slip throughout loading. This slip is evidenced by their low stiffness and extremely large deflections (over 180mm at peak load). Such slip means the layers were sliding relative to each other due to partial composite action. While interlayer slip is not a "failure" in itself, excessive slip contributed to the failure process by altering how the load was shared. In B-series beams, long before the wood ruptured, the lamellas were essentially acting in partial union, connected by yielding dowels. This mechanism absorbed energy and deformation by damaging the bearing strength of the azobe timber or yielding the dowels. By the time these beams failed, the connections had already significantly yielded (and possibly some began to fail in shear), but the slip allowed a slow progression of failure instead of a single catastrophic break.

Figure 7.21: Azobé lamellas exhibiting minor embedment failure, characterized by localized splitting and slight stress-induced deformations.

Dowel Yielding (Connector Plasticity) – A major failure mechanism was yielding of the steel dowels in shear. this doesnot lead to the failure of the beam persay but ot leads to excessive slip that increases the midspan deformation. The load–deflection curves for B1-1 and B2-2 sustained 98kN through very large deflection increments. These plateaus indicate the dowels had yielded, turning the connection into a plastic hinge that could deform further at roughly constant load. In other words the connections reached their yield strength and started deforming plastically, which delayed the final failure. This is characteristic of a ductile failure mode – the connectors yielded before the wood completely fractured. this also led to the embedment failure of the wood as to accommodate The benefit is that the beams could tolerate additional deflection and redistribute forces. By contrast, if the wood had cracked first (a brittle failure), we would see an abrupt drop in the load at peak with little plateau . The experiment showed dowel yielding provided considerable ductility, allowing the beams to maintain high load even as cracks developed.

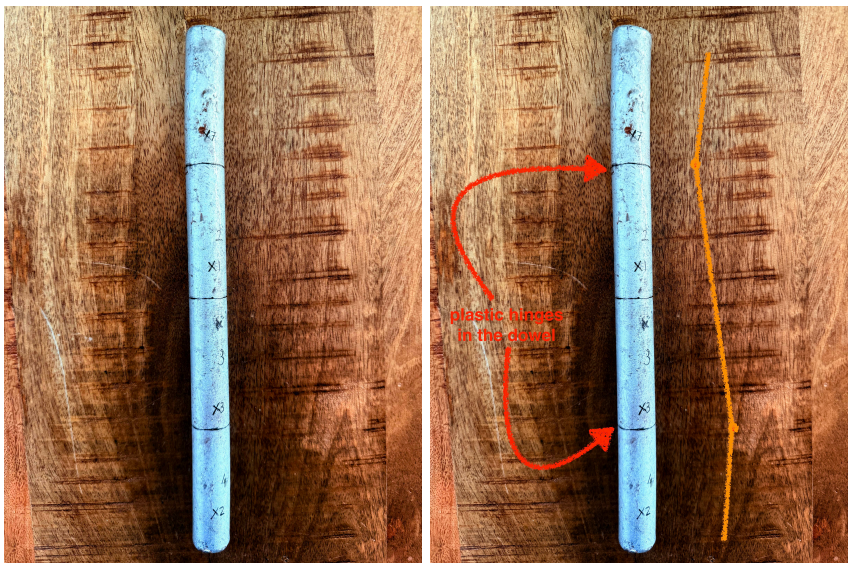

Figure 7.22: Left: Dowel extracted from the edge position of the beam B2-2 after slight failure with markings of the lamellas' position. Right: Plastic hinges line drawn to show the shape of the dowel after tensile rupture of beam B2-2.

In conclusion, the 3-point bending failures were ductile. All beams exhibited significant yielding and slip at the higher loads. Beam A2, never had a sudden drop and still had more than sufficient capacity to reach failure even at the 100KN loading. Beam A1 had a similar behaviour until a tensile crack formed at the bottom which led to a further investigation of the true bending strength of the individual lamellas, and this was achieved with the A3 beam. From the bending failure of beam A3 was deduced a bending strength of approximately 86Mpa per lamella in the Y category. Beams B1-1 and B2-2 failed in a two-stage manner: first extensive slip and dowel yielding (larger deformations) and eventually rupture in the lower most tensile fibers of the individual lamellas, but by then the structure had given ample warning (gradual load decrease). These modes can be described as tensile rupture of the wood preceded by interlayer slip and dowel yielding. The observed ductility is a direct result of the steel dowels performing in shear before the brittle capacity of the wood was exceeded - a desirable failure pattern for safety.

7.6. Comparisons between EI_{eff}, K_{ser} values and γ values

Effective Stiffness EI_{eff} and Gamma γ-values

The effective flexural rigidity, EI_{eff}, is derived from the slope of the load-deflection curve, while the γ values are obtained from the stiffness measured during the 3-point bending test up to 100 kN. Both A and B beams exhibit uniform effective stiffness within their respective groups, indicating a similar load-carrying capacity.

Table 7.4: Stiffness Measurements and Gamma Factors for Various Beam Configurations

Parameter	**A-Series (Large Cross Section)**		**B-Series (Small Cross Section)**	
	A1	**A2**	**B1-1**	**B2-2**
Stiffness Values $EI_{eff}(\text{Nmm}^2 \times 10^{12})$				
Analytical stiffness	2.24	2.24	1.924	1.924
3-point bending stiffness (Test to 100KN)	2.33	2.26	1.35	1.36
3-point bending stiffness	2.17	2.17	1.15	1.07
4-point bending stiffness	2.160	2.270	1.540	1.13
Full composite stiffness (EI_{full})	4.100	4.100	4.100	4.100
Gamma Factors (γ)				
Experimental γ_1 and γ_4	0.421	0.397	0.291	0.294
Theoretical γ_1 and γ_4	0.391	0.391	0.435	0.441
Deviation from theory (%)	+7.7%	+1.5%	-33.1%	-33.3%
Experimental γ_2 and γ_3	0.421	0.397	0.194	0.196
Theoretical γ_2 and γ_3	0.391	0.391	0.344	0.350
Deviation from theory (%)	+7.7%	+1.5%	-43.6%	-44.0%

The γ values revealed that the A beams - with their larger cross sections -exhibited a higher composite behaviour than the smaller B beams. In contrast, Möhler's experiments conclude having achieved near full composite action, a result that may be attributed to the fact that his beams had an additional bolt connections at each end and used four lamellas with a 150 $\times$ 150 mm cross section. These tests suggest that possibly, larger members tend to develop a more pronounced composite action, which could explain the discrepancies observed between our results and Möhler's findings.

7.6.1. Effective Stiffness EI_{eff} and the Slip Modulus Values K_{ser}

K_{ser}: When reverse-engineered to determine the K_{ser} values, the table below summarizes the experimentally observed and Eurocode-derived values, explaining the discrepancies. For beams consisting of two layers with differing elastic moduli, it is generally expected to encounter one shear plane, thus yielding a single K_{ser} value. However, variations in the modulus of elasticity (MOE), even for beams with similar geometric characteristics, causes a shift in the neutral axis position. If the neutral axis is assumed to lie in the middle of the beam precisely between the members to avoid complications, the formulas for K_{ser} become for a two-layered beam:

$$k_{\text{ser}} = \frac{\pi^2 s}{L^2} \cdot \frac{E_1 A_1 \cdot E_2 A_2}{E_1 A_1 + E_2 A_2} \left(\frac{1}{\frac{1}{\gamma_{1,2}} - 1} \right). \tag{7.2}$$

For a four-layered beam, there are three shear planes (between layers 1–2, 2–3, and 3–4), and

thus three values of k_{ser}. Based on Schelling's method, the K value was defined in Section 3, and the shear stiffness values are calculated accordingly.

$$k_{\text{ser}_{1,2}} = \frac{\pi^2 E_{1,2} A_{1,2} s}{2 l^2 \left(K-1\right)} \tag{7.3}$$

$$k_{\text{ser}_{2,3}} = \frac{\pi^2 E_{2,3} A_{2,3} s}{2 l^2 \left(K-1\right)} \tag{7.4}$$

Table 7.5: Comparison of slip modulus k_{ser} values

Beam Type	Configuration	Dimensions per Layer (mm×mm)	k_{ser} from EC5 (N/mm)	k_{ser} derived from 3-point test (N/mm)	% Difference
A1	2-layer	140 × 140	30 864	14 854	−108
A2	2-layer	140 × 140	30 864	14 082	−119
B1-1	4-layer	140 × 70	30 864	12 581	−145
B2-2	4-layer	140 × 70	30 864	19 133	−61

Table 7.6: % difference is computed as $\frac{(\text{Derived})-(\text{Eurocode})}{(\text{Derived})} \times 100\%$

When Kser values are derived for the four lamella beams, to obtain similar results using the Schelling method. The values obtained are several percentage points lower in all four cases by a factor of around 2. This discrepancy needs further investigation into why the values came short but as the EUROCODE 5 'kser value is only dependent on dowel size and wood density.

8

CONCLUSIONS AND RECOMMENDATIONS

The thesis was guided by two central research questions:

What is the actual effective stiffness of mechanically jointed Azobé beams?

Which factors affect the load-bearing capacity and structural behaviour of these beams?

The effective stiffness of the beams is dependent on the composite action parameters, particularly the γ-value, which itself is based on the shear stiffness or slip modulusK_{ser}. This modulus is directly influenced by the quality of the connection between the dowels and the lamellas. By working backwards from the determined effective stiffness (EI_{eff}) to obtain the corresponding γ-values, a comparative table was produced to compare experimental findings with the analytical predictions. as in section 7.3.

Reverse-calculated γ values closely match the analytical predictions with deviations below 10% in two-layered beams (favouring experimental results). In contrast, four-layered beams show deviations up to 40% (favoring analytical results). These discrepancies require further investigation.

For the four-lamella beams, K_{ser} values determined via the Schelling method (based on effective stiffness) are lower by several percentage points in all cases, approximately a factor of 2 lower. This discrepancy merits further examination, particularly given that the EUROCODE 5 K_{ser} depends solely on dowel size and wood density.

Industry implications - Practitioners should exercise caution when directly applying Möhler or Schelling models. Current observations indicate that the Schelling method tends to slightly overestimate composite action, while findings for the Möhler's (γ) model vary; one experiment suggested a slight underestimation, and other a slight overestimation. More research is needed to clarify the source of these discrepancies.

Analysis of MOE and density values of the Azobe lamellas showed that the samples substantially exceed the requirements of EN338 [2] for the D70 class of hardwood in terms of both density and modulus of elasticity. Unfortunately, the bending strength properties could not be readily determined. These mechanical properties indicate that the Eurocode should revise the strength classes of the D sector upward, allowing these woods to be properly graded and used by the industry.

There is a reduction in the bending stiffness of the lamellas of around 7% for a 0.01% reduction in volume when the holes are drilled in a lamella, and this needs further investigation to find out what the new value of MOE is when the holes are filled with steel or any other material. The implication being that the MOE values we use to calculate are overestimated.

Further research is required to investigate the friction within the beam lamellas. The initial load displacement diagrams exhibited a stack slip behaviour, characterised by a high initial stiffness and a subsequent constant linear slope.

The alternating of the higher-grade lamellas into positions of maximum stress (outer layers) could potentially enhance the overall stiffness of the beam. The most significant failure mechanism observed in the tests was tensile failure in the lowest fibre of the individual lamellas in the position of high tensile stress. According to the results, the stiffness values were 2.9% higher when the most stiff lamella was placed in the middle compared to other beam B2 lamella combinations. Further research is necessary to explore this phenomenon. However, by understanding the stresses of the beam and having observed the failure mechanisms, it can be recommended to align the higher stiffness lamellas in the lower and higher posts. In industry, non destructive methods can be used to measure the MOE_{Dyn}.

DIC technology was used to monitor the slip deformations of beam lamellas over time. However, its measurements did not align with those of the LVDT due to an inability to clearly separate the slip of individual lamellas from the overall rigid body movement. Although relative distances were used to indicate slip, the program did not distinctly define the difference between rigid body movement and slip, leading to overestimated absolute values. In contrast, DIC captures well vertical displacements primarily reflecting rigid body movement so those magnitudes can be trusted. Therefore, when measuring slip, it is required that the relative movement is properly isolated from any global beam movement.

Although dowel failure was defined by failure mode a or b from calculations, the retrieved dowel exhibited yielding. This observation warrants further investigation into the overall force redistribution within the beam for even when a dowel yields, the beam retains its load-carrying capacity as forces transfer to the stiffer dowels located near the center.

In conclusion, the experiments confirm that the effective stiffness of mechanically jointed Azobé beams hinges on the slip modulus, friction, connection quality, lamella arrangement, and real modulus of elasticity, all of which influence the composite action. Larger cross sections generally show improved composite behaviour, while strategic placement of higher-grade lamellas in areas of maximum stress may further increase the effective stiffness. Although analytical models such as those by Möhler and Schelling offer useful approximations, they may over- or underestimate composite action. Investigations indicated that Azobé lamellas exceed the EN338 D70 hardwood classification in both density and stiffness. However, drilling holes in dowels can reduce bending stiffness, and testing also revealed that the yielding of one dowel does not lead to abrupt failure, as forces are redistributed to other dowels. These findings show the need for ongoing research to use DIC technology for measurements, to account for friction and potential stiffness reductions, and optimise lamella placement for maximum structural efficiency.

A

LOAD DEFLECTION DIAGRAMS

A.1. LOAD DEFLECTION DIAGRAMS FOR THE INDIVIDUAL LAMELLAE MOE-GLOBAL

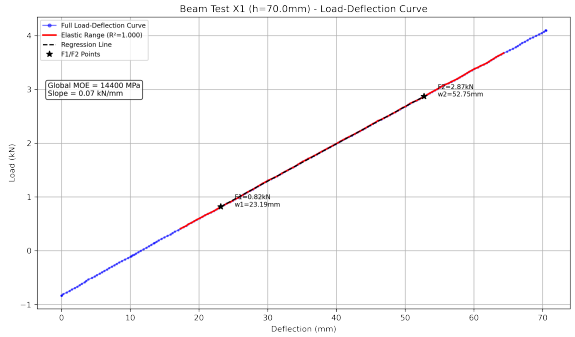

(a) X1

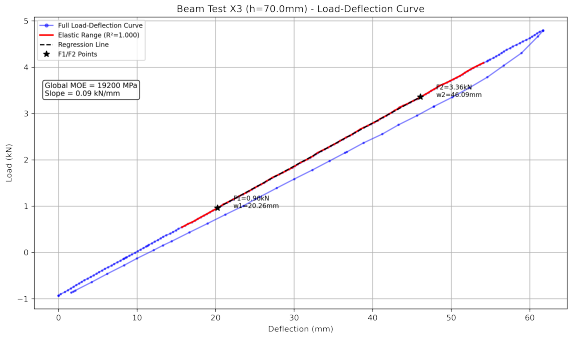

(d) X3

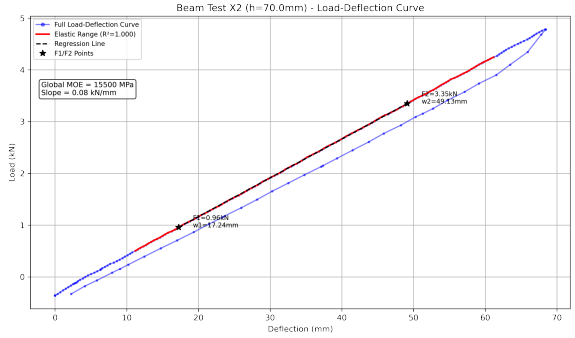

(b) X2

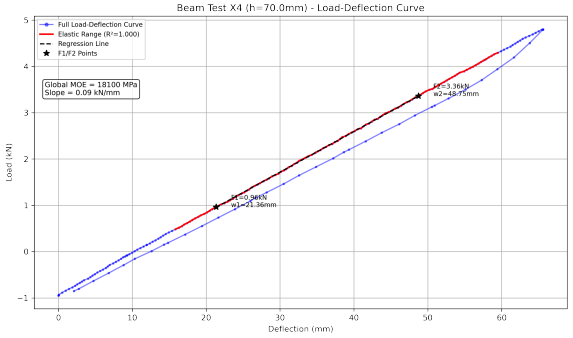

(e) X4

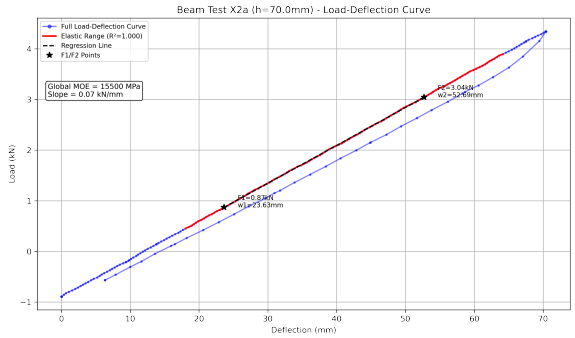

(c) X2a

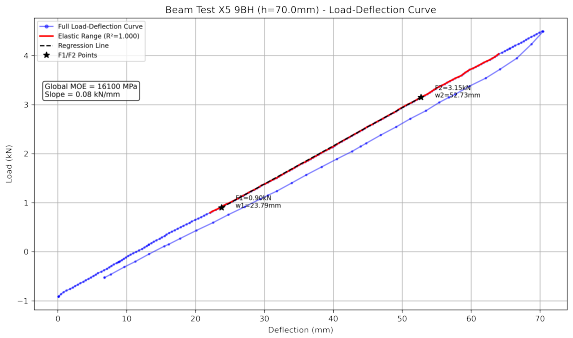

(f) X5 (9BH)

Figure A.1: Load-deflection diagrams (Global MOE).

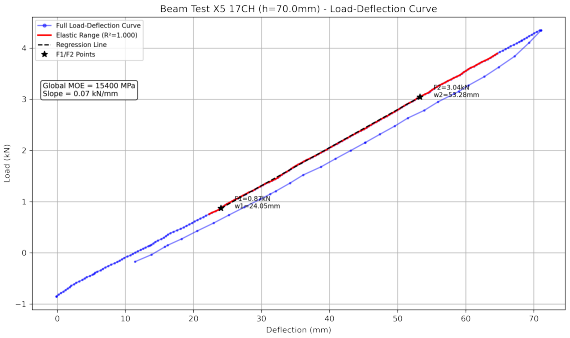

(a) X5 (17CH)

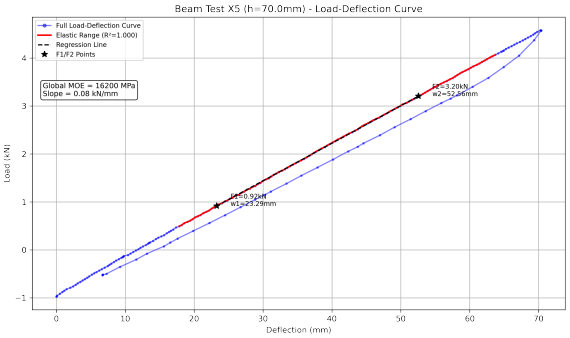

(b) X5

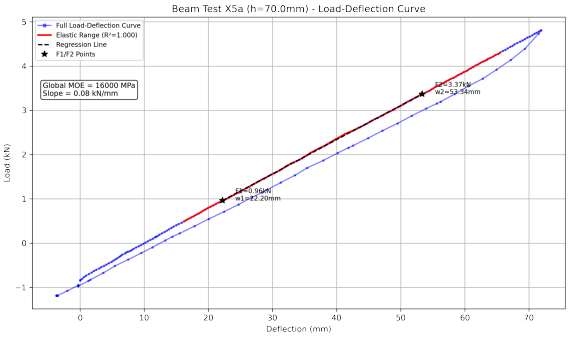

(c) X5a

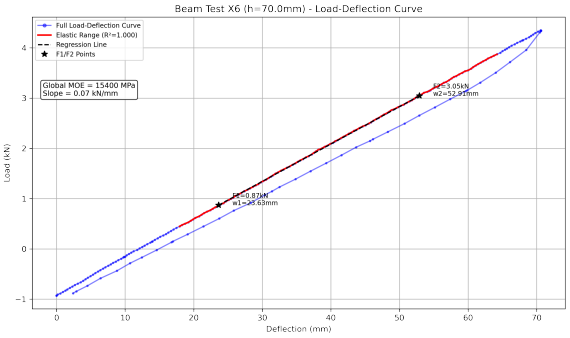

(d) X6

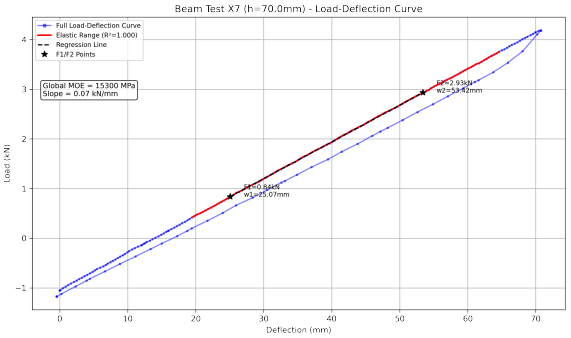

(e) X7

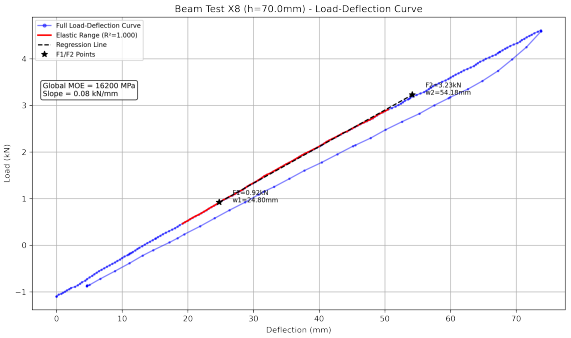

(f) X8

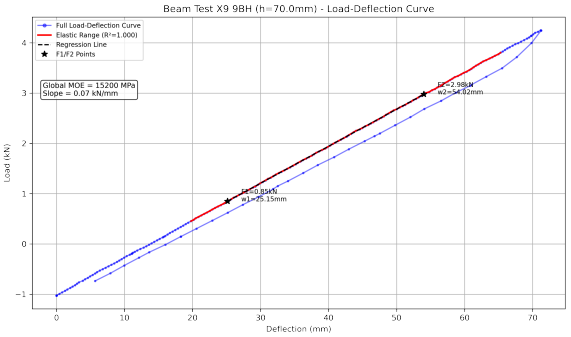

(g) X9 (9BH)

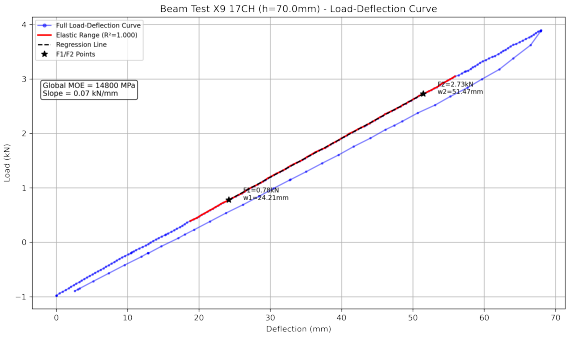

(h) X9 (17CH)

Figure A.2: Load-deflection diagrams (Global MOE).

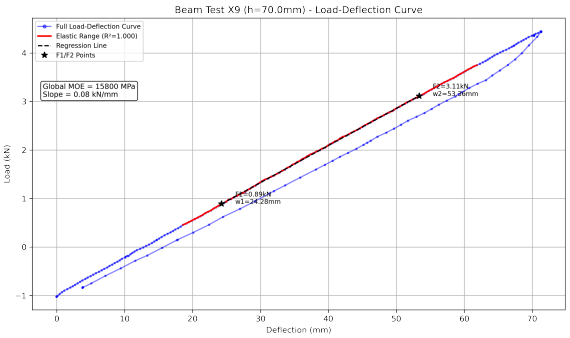

(a) X9

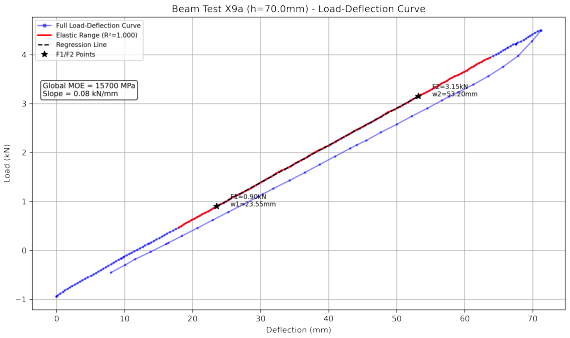

(b) X9a

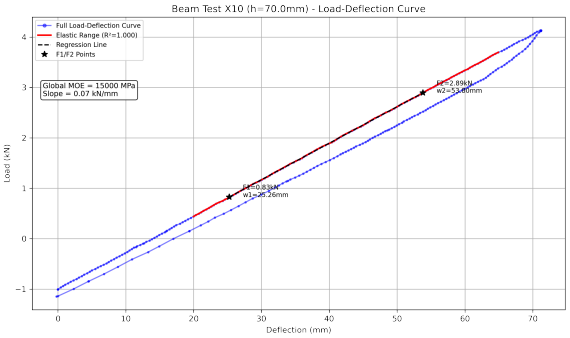

(c) X10

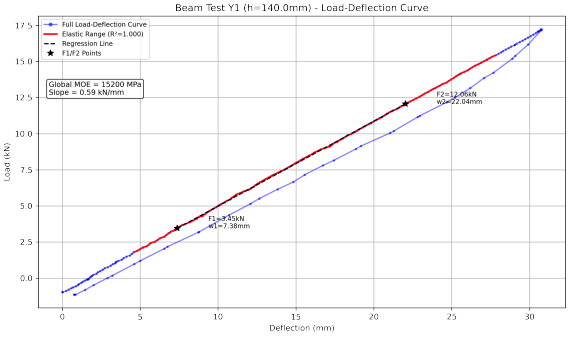

(d) Y1

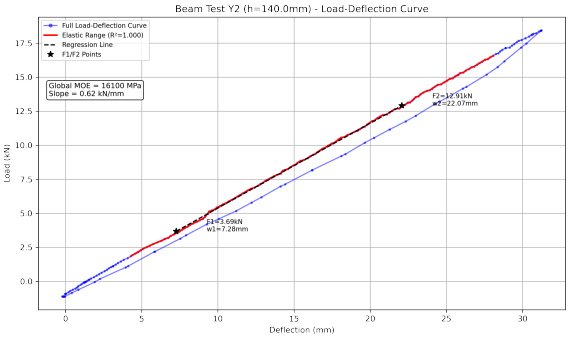

(e) Y2

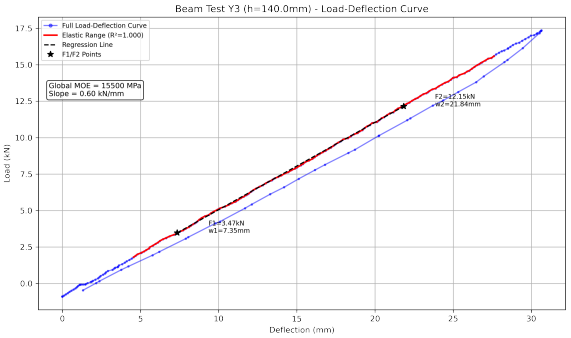

(f) Y3

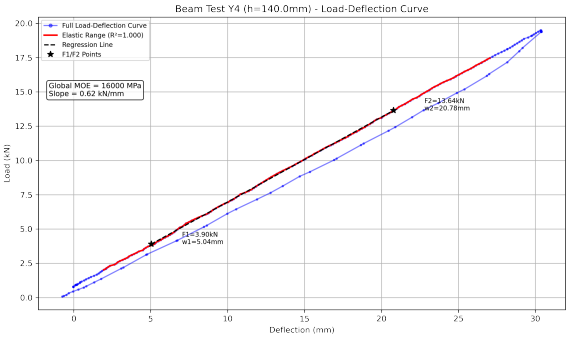

(g) Y4

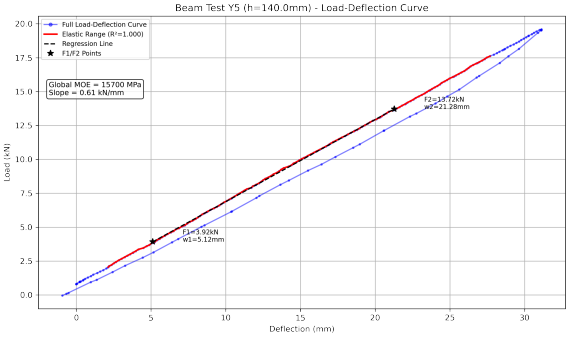

(h) Y5

Figure A.3: Load-deflection diagrams (Global MOE)

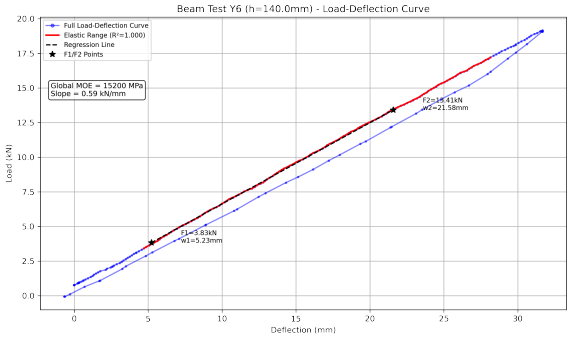

Figure A.4: Load-deflection diagram (Global MOE).

A.2. LOAD DEFLECTION DIAGRAMS FOR THE INDIVIDUAL LAMELLAE MOE-LOCAL

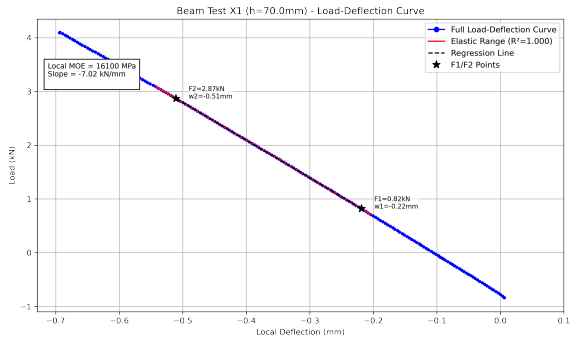

(a) X1

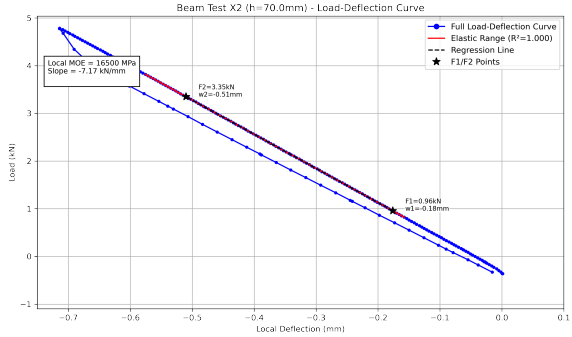

(b) X2

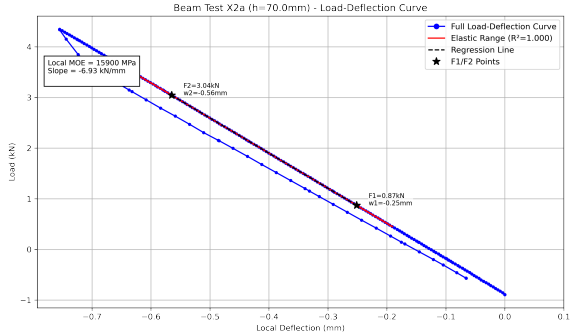

(c) X2a

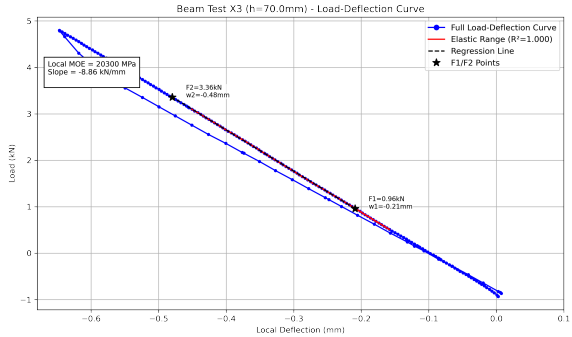

(d) X3

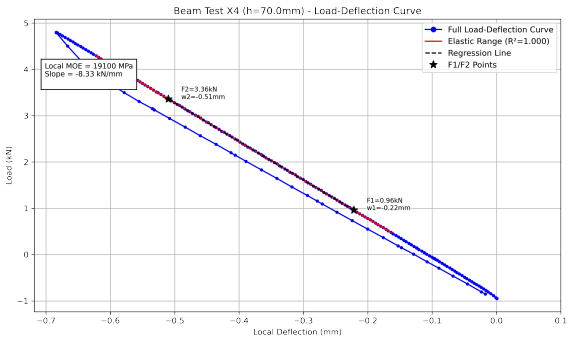

(e) X4

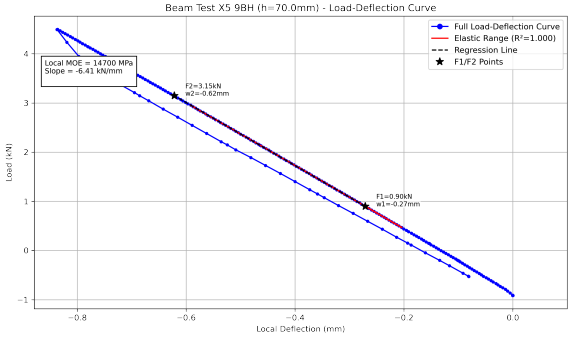

(f) X5 (9BH)

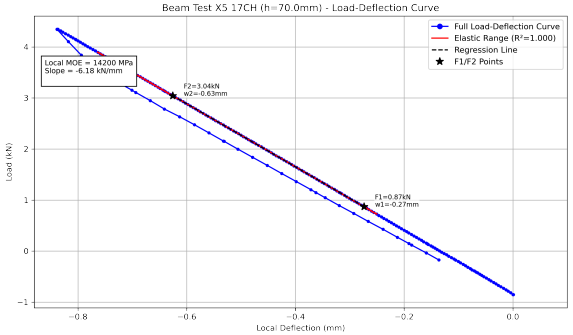

(g) X5 (17CH)

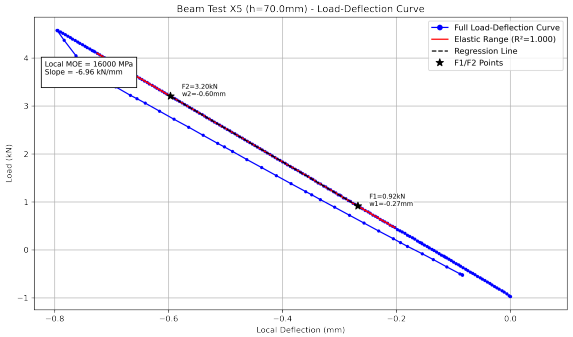

(h) X5

Figure A.5: Load-deflection diagrams (LOCAL-MOE).

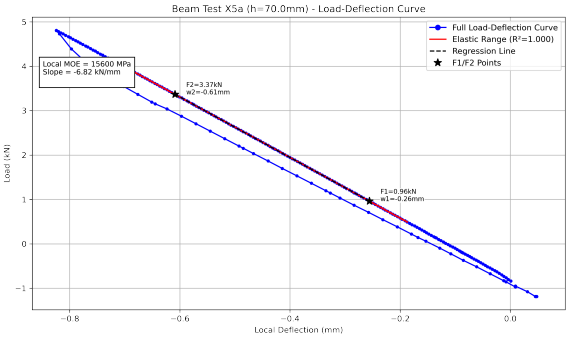

(a) X5a

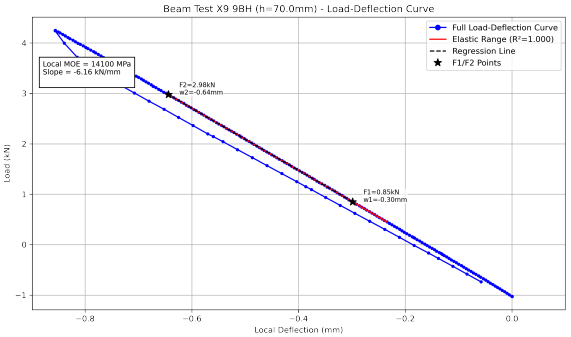

(e) X9 (9BH)

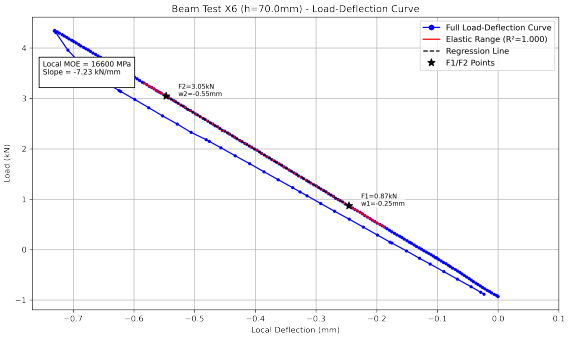

(b) X6

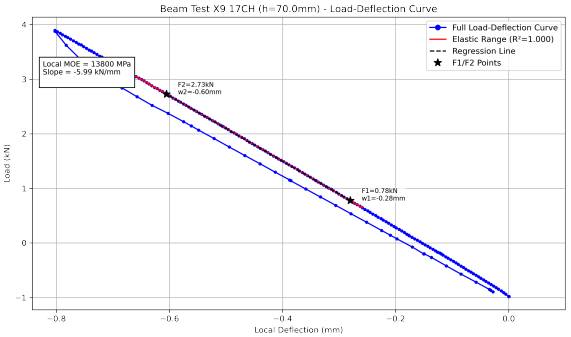

(f) X9 (17CH)

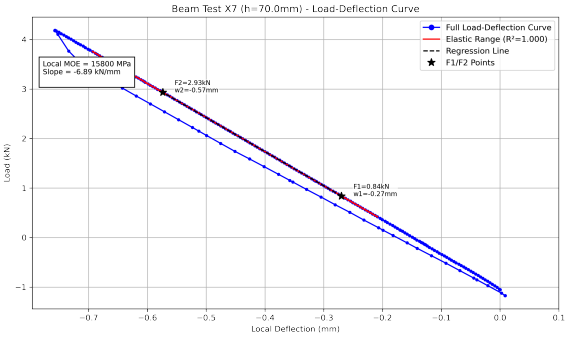

(c) X7

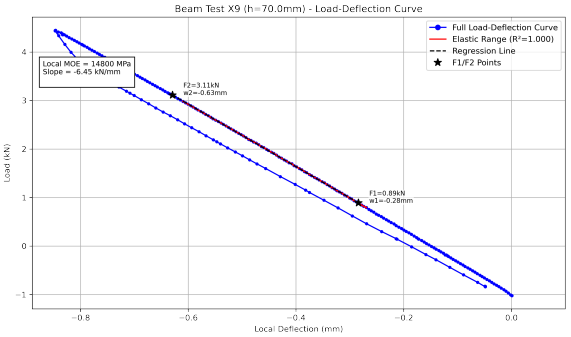

(g) X9

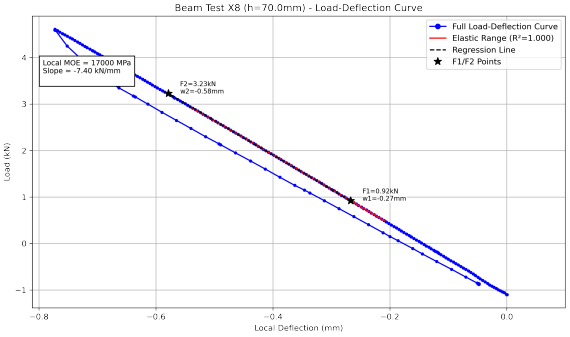

(d) X8

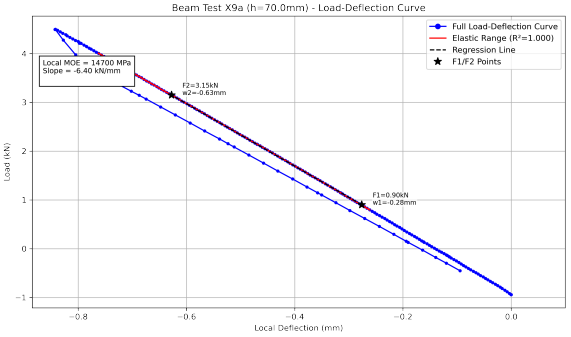

(h) X9a

Figure A.6: Load-deflection diagrams (LOCAL-MOE).

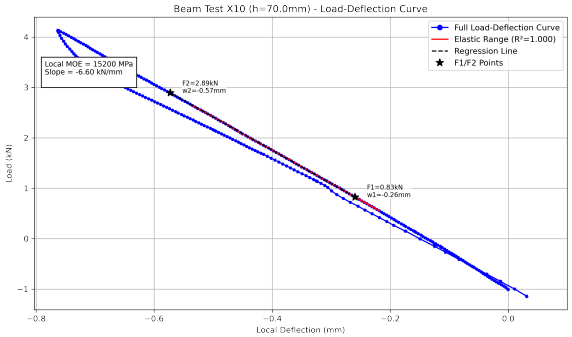

(a) X10

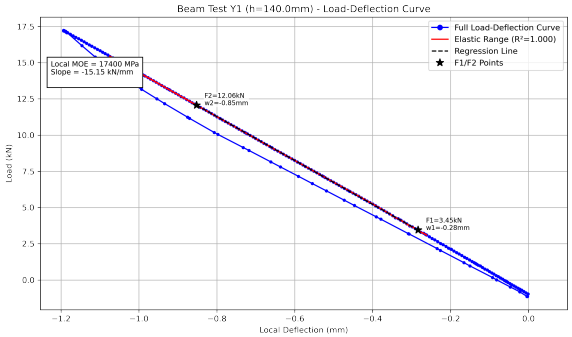

(b) Y1

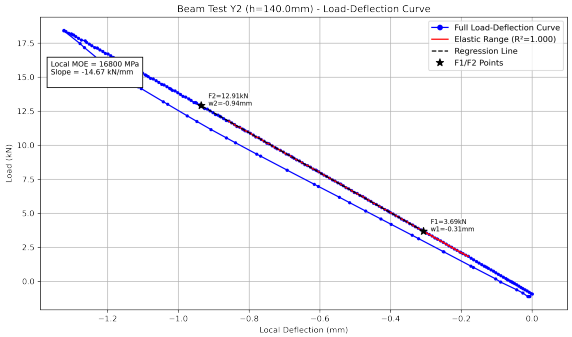

(c) Y2

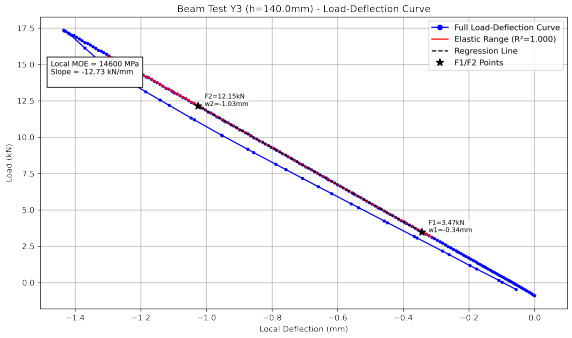

(d) Y3

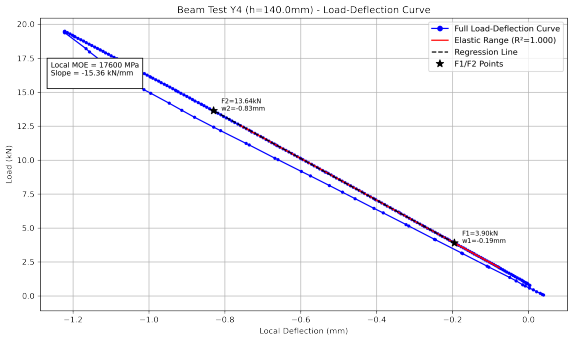

(e) Y4

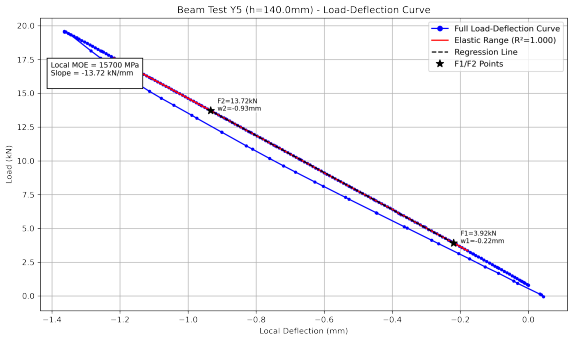

(f) Y5

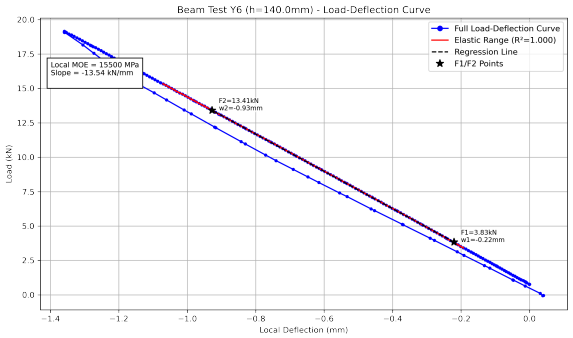

(g) Y6

Figure A.7: Load-deflection diagrams for the (LOCAL-MOE).

A.3. Stacked Beams

A.3.1. 4-Point Loading

Table A.1: Stacked Beam performance parameters

Beam Type	Configuration	Maximum Load (kN)	Maximum Deflection (mm)	Permanent Deformation (mm)	EI_{eff} (Nmm^2)	Elastic Stiffness (kN/mm)
A1	2-layer (140 × 140)	36.79	27.99	0.30	1.24e+12	1.27
A2	2-layer (140 × 140)	35.14	26.80	0.62	1.20e+12	1.23
B1-1	4-layer (140 × 70)	19.20	55.62	1.06	3.25e+11	0.33
B2-2	4-layer (140 × 70)	19.19	57.45	1.63	3.18e+11	0.33

Table A.2: EI_{eff} represents the effective bending stiffness of the jointed beam system.

The effective bending stiffness EI_{eff} is computed using the following formula:

$$EI_{\text{eff}} = \text{slope} \times \frac{\left(3\,a\,L^2 - 4\,a^3\right)}{48} \quad (\text{in N mm}^2) \tag{A.1}$$

In this expression, L represents the length of the beam where $L = 3600\,\text{mm}$ and $a = 1200\,\text{mm}$.

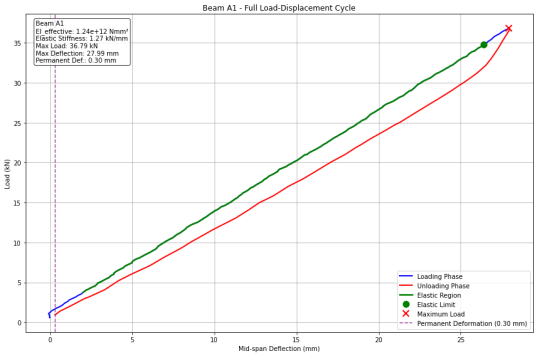

(a) Load displacement curve Beam A1

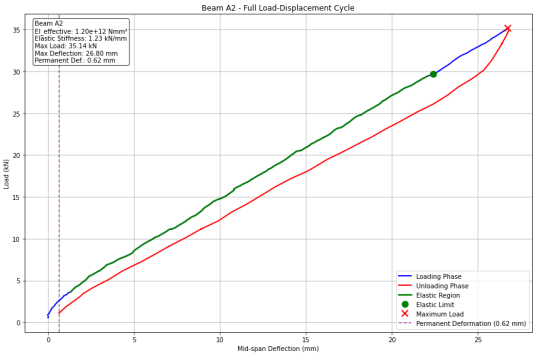

(b) Load displacement curve Beam A2

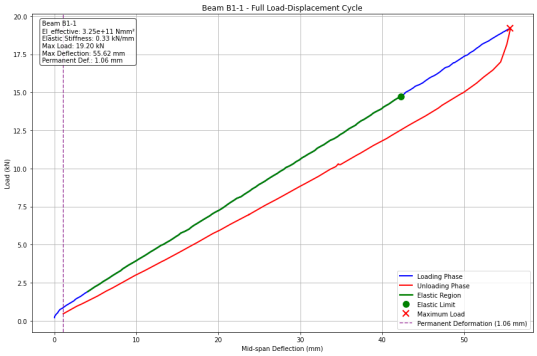

(c) Load displacement curve Beam B1-1

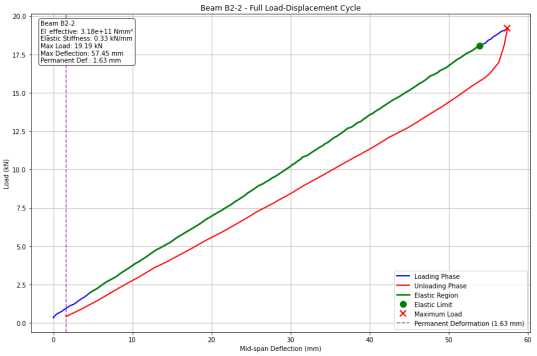

(d) Load displacement curve Beam B2-2

Figure A.8: Load-displacement curves for stacked beams in the 4point deformation series.

A.3.2. 3-Point Loading

Table A.3: stacked Beam performance parameters

Beam Type	Configuration	Maximum Load (kN)	Maximum Deflection (mm)	Permanent Deformation (mm)	EI_{eff} (Nmm^2)	Elastic Stiffness (kN/mm)
A1	2-layer (140 × 140)	22.35	20.23	0.25	1.04e+12	1.07
A2	2-layer (140 × 140)	20.16	19.88	0.12	8.79e+11	0.90
A3	2-layer (140 × 140)	87.74	173.38	38.46	9.92e+11	1.02
B1-1	4-layer (140 × 70)	12.61	42.58	1.16	2.62e+11	0.27
B2-2	4-layer (140 × 70)	12.85	43.48	0.28	2.66e+11	0.27

Table A.4: EI_{eff} represents the effective bending stiffness of the jointed beam system.

The effective bending stiffness EI_{eff} is computed using the following formula:

$$EI_{\text{eff}} = \frac{\text{slope} \cdot L^3}{48} \quad (\text{in N mm}^2) \tag{A.2}$$

In this expression, L represents the length of the beam, where $L = 3600\,\text{mm}$.

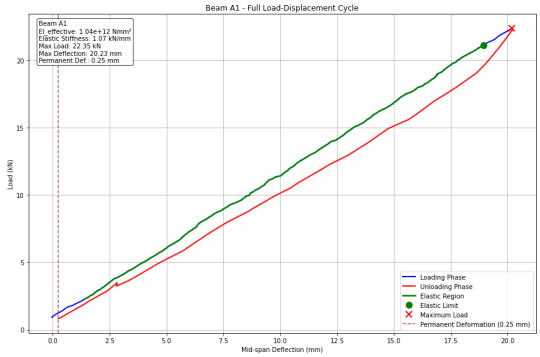

(a) Load displacement curve Stacked Beam A1

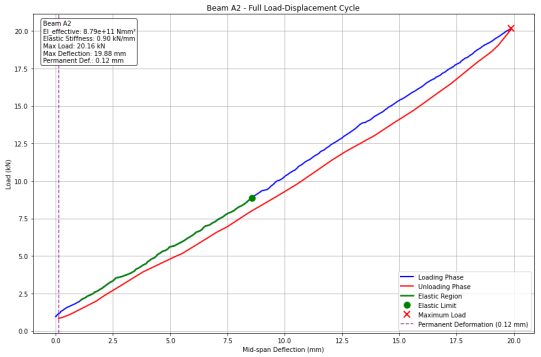

(b) Load displacement curve Stacked Beam A2

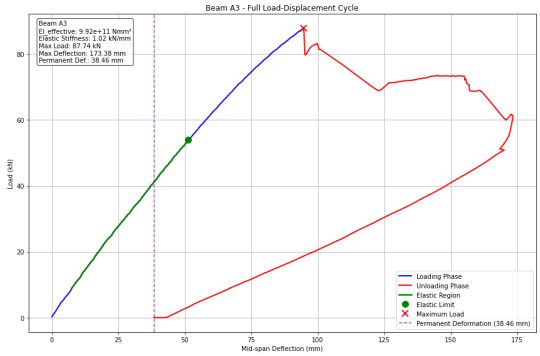

(c) Load displacement curve Stacked Beam A3

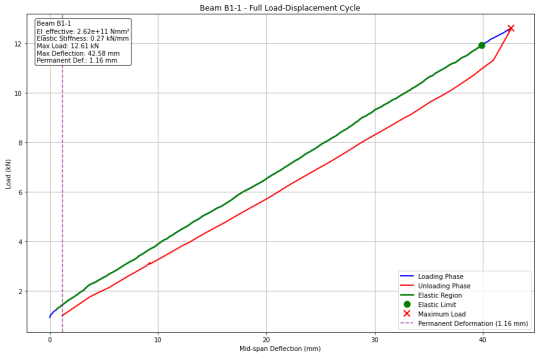

(d) Load displacement curve Stacked Beam B1-1

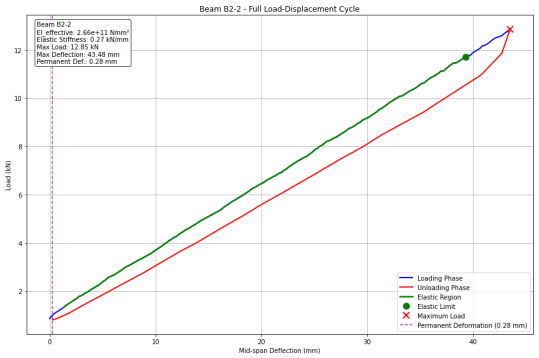

(e) Load displacement curve Stacked Beam B2-2

Figure A.9: Load-displacement curves for all tested stacked beams. The A-series (A1, A2, A3) and the B-series (B1-1, B2-2) represent different stacking configurations.

A.4. Mechanically Jointed Beams In 3-Point Loading To 100KN

Table A.5: Beam performance parameters

Beam Type	Configuration	Maximum Load (kN)	Maximum Deflection (mm)	Permanent Deformation (mm)	EI_{eff} (Nmm^2)	Elastic Stiffness (kN/mm)
A1	2-layer (140 × 140)	100.06	62.35	6.27	2.33e+12	2.40
A2	2-layer (140 × 140)	100.06	54.52	4.45	2.26e+12	2.32
B1-1	4-layer (140 × 70)	75.44	89.66	9.81	1.35e+12	1.38
B1-1*	4-layer (140 × 70)	98.86	163.90	27.62	-	1.03
B2-2	4-layer (140 × 70)	97.37	171.04	31.15	1.36e+12	1.39

Table A.6: EI_{eff} represents the effective bending stiffness of the jointed beam system. *Denotes repeated test reaching further loading.

The effective bending stiffness EI_{eff} is computed using the following formula:

$$EI_{\text{eff}} = \frac{\text{slope} \cdot L^3}{48} \quad (\text{in N mm}^2) \tag{A.3}$$

In this expression, L represents the length of the beam. $L = 3600\,\text{mm}$

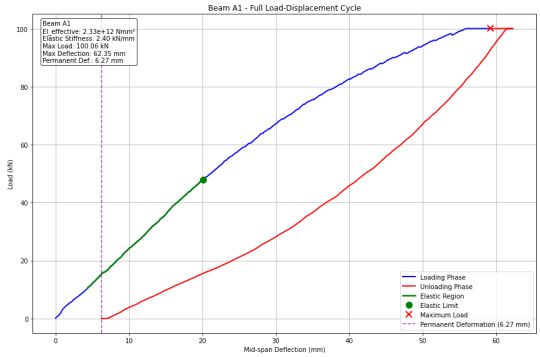

(a) Load displacement curve Beam A1

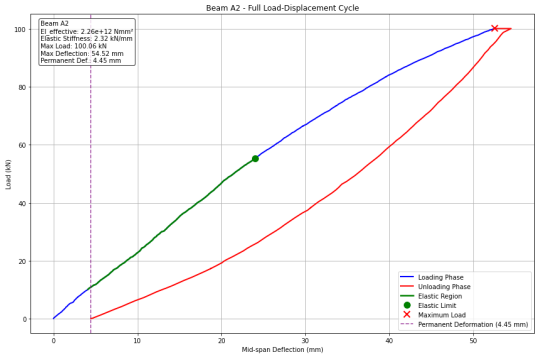

(b) Load displacement curve Beam A2

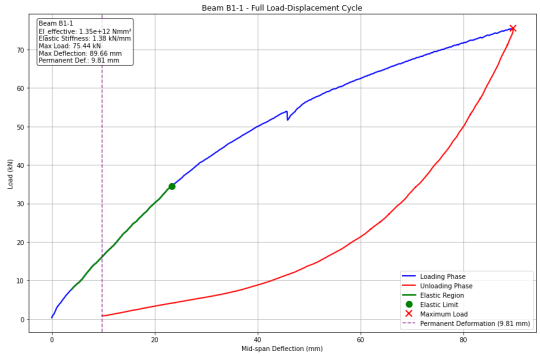

(c) Load displacement curve Beam B1-1

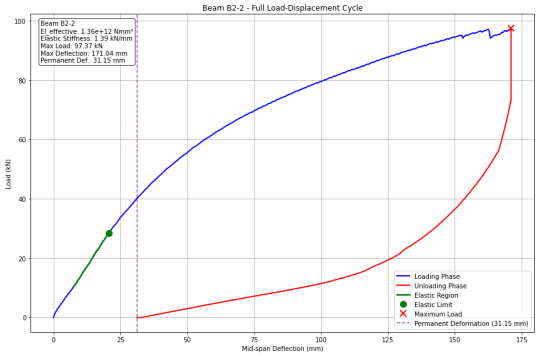

(d) Load displacement curve Beam B2-2

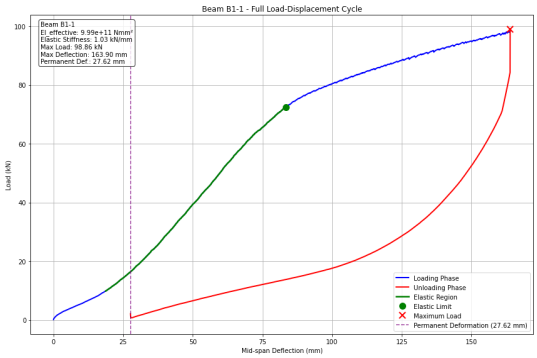

(e) Load displacement curve Beam B1-1*

Figure A.10: Load-displacement curves for all tested beams. The A-series (A1, A2) consists of 2-layer beams, while the B-series (B1-1, B1-1*, B2-2) consists of 4-layer beams. The asterisk (*) denotes a repeated test with higher load.

B

annex 2

Table B.1: Moisture content MC%

Lamella Id	Mass	Old mass	% change	New mass	% change	MC %	Average MC %
X1a	256.52	222.01	15.5	221.72	0.1	15.7	15.9
X1b	252.93	218.14	15.9	217.88	0.1	16.1	
X2a	252.28	216.08	16.8	215.77	0.1	16.9	16.1
X2b	247.21	214.66	15.2	214.44	0.1	15.3	
X3a	264.54	229.37	15.3	229.07	0.1	15.5	17.1
X3b	276.20	232.95	18.6	232.64	0.1	18.7	
X4a	274.07	232.85	17.7	232.57	0.1	17.8	18.0
X4b	262.20	222.27	18.0	222.0	0.1	18.1	
X5a	255.18	218.45	16.8	218.19	0.1	17.0	16.4
X5b	242.59	209.51	15.8	209.27	0.1	15.9	
X6a	260.40	224.31	16.1	224.03	0.1	16.2	16.9
X6b	236.45	201.17	17.5	200.97	0.1	17.7	
X7a	263.97	227.05	16.3	226.81	0.1	16.4	16.5
X7b	262.64	225.53	16.5	225.35	0.1	16.5	
X8a	256.07	219.56	16.6	219.37	0.1	16.7	16.2
X8b	243.63	210.69	15.6	210.47	0.1	15.8	
X9a	244.72	208.59	17.3	208.40	0.1	17.4	17.4
X9b	255.16	217.79	17.2	217.50	0.1	17.3	
X10a	258.85	222.94	16.1	222.64	0.1	16.3	16.4
X10b	253.22	217.36	16.5	217.16	0.1	16.6	
Y1a	640.1	519.96	23.1	519.94	0.0	23.1	24.8
Y1b	545.61	431.37	26.5	431.33	0.0	26.5	
Y2a	320.83	254.16	26.2	254.12	0.0	26.3	26.2
Y2b	521.69	413.29	26.2	413.27	0.0	26.2	
Y3	0	0	—	0	—	—	25.9
Y4a	555.50	441.26	25.9	441.22	0.0	25.9	26.7
Y4b	528.09	414.40	27.4	414.36	0.0	27.4	
Y5	0	0	—	0	—	—	26.0
Y6a	379.55	303.81	24.9	303.79	0.0	24.9	26.1
Y6b	508.09	399.11	27.3	399.07	0.0	27.3	

Table B.2: Beam Configuration Analysis

Case	Beam Configuration	Dimensions (mm)	I (mm^4)	Force (KN)	Deformation (mm)	Bending Stress(MPa)
1	Single Lamella	140×140	3.20×10^7	14.2	24	28
2	Single Lamella	140×70	4.00×10^6	3.6	48	28
3	Two stacked lamellas	$2 \times (140 \times 140)$	6.40×10^7	28.4	24	–
4	Four stacked lamellas	$4 \times (140 \times 70)$	1.60×10^7	14.4	48	–

Table B.3: Analytical vs. Four-Point Tested Stiffness for Beam Types and Setups with Percentage Differences

Beam type	Setup	Analytical stiffness ($E_{m,g}$) (N/mm^2)	Four point bending stiffness ($E_{m,g}$) N/mm^2	Three point tested stiffness $E_{m,g}$ N/mm^2
Beam A1	Y1 Y2	15,600	16,100	16,300
Beam A2	Y6 Y4	15,600	16,000	14,800
Beam B1-1	X8X6X10X4	16,100	17,300	16,400
Beam B1-2	X8X4X6X10	16,100	17,800	-
Beam B2-1	X3X2X7X1	16,100	17,000	-
Beam B2-2	X7X1X3X2	16,100	16,900	16,000

Table B.4: Summary Statistics of Mechanically Jointed Beam Tests

Beam ID	**Maximum Force (kN)**	**Maximum Left Displ. (mm)**	**Left Average at Max Force (mm)**
Test 4p Doweled A1 (Y1-Y2)	51.40	1.03	0.65
Test 4p Doweled A2 (Y6-Y4)	50.94	0.97	0.59
Test 4p Doweled B1-1 (X8-X6-X10-X4)	39.87	1.09	0.63
Test 4p Doweled B2-2 (X7-X1-X3-X2)	34.84	1.17	0.71

Table B.5: Interpolated Displacement and Percentage Differences

	Displacement (mm)				**Percentage Difference (%)**		
Force (kN)	**A1**	**A2**	**B1-1**	**B2-2**	**A2 vs A1**	**B1-1 vs A1**	**B2-2 vs A1**
0.0	–	–	0.000	–	–	–	–
5.0	0.066	0.013	0.020	0.082	−80.45	−69.81	23.45
10.0	0.138	0.051	0.077	0.206	−63.26	−43.98	49.06
15.0	0.199	0.112	0.144	0.317	−43.74	−27.43	59.41
20.0	0.258	0.177	0.210	0.418	−31.37	−18.45	62.12
25.0	0.315	0.245	0.304	0.514	−22.36	−3.76	63.10
30.0	0.374	0.312	0.410	0.613	−16.61	9.76	63.97
35.0	0.433	0.378	0.531	–	−12.74	22.55	–

C

ANNEX

In the context of determining the experimental bending stiffness EI_{eff} of composite beams, the experimental EI_{eff} values are initially calculated as discussed in the preceding sections. EC5 provides a framework for deriving the effective bending stiffness of composite beams, utilizing a series of equations based on the gamma method (γ-method). This method focuses on the theoretical calculations of EI_{eff}:

$$EI_{\text{eff}} = \sum_{i=1}^{n} \left(E_i \times I_i + \gamma_i \times E_i \times A_i \times a_i^2 \right) \tag{C.1}$$

Here, γ_i quantifies the efficiency of each lamina within the composite, taking into account mechanical connectors. It is calculated by the following equation:

$$\gamma_i = \left(1 + \frac{\pi^2 \times E_i \times A_i \times S_i}{K_{ser,i} \times l^2} \right)^{-1} \tag{C.2}$$

The slip modulus of the fasteners, $K_{ser,i}$, is a function of the fastener's density (ρ_m) and diameter (d), detailed in Equation (C.3):

$$K_{ser,i} = \left(\rho_m^{1.5} \times \frac{d^2}{23} \right) \tag{C.3}$$

This study evaluates various EI_{eff} values, from experimental to fully composite, utilizing the framework of Equations. Additionally, Equation (C.4) can be used to assess the efficiency μ of the composite in laminated beams:

$$\mu = \frac{EI_{comp} - EI_{min}}{EI_{max} - EI_{min}} \tag{C.4}$$

This approach enables a comprehensive understanding of the composite behaviour under varying mechanical conditions.

To calculate the deformation caused by a force in a four-point bending test for an Azobe lamella (beam), and to ensure that the member remains within the elastic phase (so it returns to its

original shape after the load is removed), follow these steps: A stress value that is 40% the characteristic bending strength is used

C.1. Calculate the Moment of Inertia (I)

For a rectangular cross-section, the moment of inertia I is calculated using:

$$I = \frac{bh^3}{12}$$

C.2. Beam Specifications

Where:

- b = width of the beam
- h_1 = height of the 2-lamella beam
- h_2 = height of the 4-lamella beam

Given:

$$b = 140mm$$
$$h_1 = 140mm$$
$$h_2 = 70mm$$

C.3. 2. Determine the Loading Configuration

In a four-point bending test, two equal loads P are applied symmetrically at a distance a from each support.

Given:

- Total length of the beam (span): $L = 3.5\,\text{m}$

The loads P are applied at $\frac{L}{3}$ at each end:

For lamellas of H1,H2 and H(full beam height)

$$a = \frac{L}{3} = \text{mm}$$

C.4. Calculate Maximum Bending Moment (M_{max})

The maximum bending moment occurs between the load points and is constant:

$$M_{\text{max}} = P \times a$$

C.5. 4. Ensure that maximum stress is within elastic limits

The maximum bending stress σ_{max} must not exceed the proportional limit (elastic) of the material σ_{allow}:

first for the normal stresses for the individual lamellas are to be calculated with these two formulas to account for the joint stiffness. thus

$$\sigma_{m,i} = \frac{0.5 h_i M}{(I)} \tag{C.5}$$

The maximum shear force will also be calculated as The general formula for the shear stress (τ) in a beam is given by:

$$\tau = \frac{VQ}{Ib}$$

Where:

- V = Shear force at the section
- Q = First moment of the area above (or below) the point where shear stress is being calculated about the neutral axis

For a singular rectangular cross-section, the moment of inertia (I) and the first moment of area (Q) are calculated as follows:

$$Q = \frac{bh \cdot \frac{h}{4}}{2} = \frac{bh^2}{8}$$

$$\tau_{\max} = \frac{3V}{2bh}$$

C.6. Calculate Maximum Deflection ($\delta_{\max}$)

Use the deflection formula for a simply supported beam under four-point bending:

$$\delta_{\max} = \frac{Pa(3L^2 - 4a^2)}{48EI}$$

Where:

- E = Modulus of Elasticity of Azobe = $18,500$ N/mm2)
- P = load at each point

when the beams have no composite action (free sliding): Like in the cases 3 and 4, there is no shear connection at all, and the lamellas simply lie on top of each other without transferring shear, they do not form a stiffer composite section. Instead, each lamella essentially bends independently. If both lamellas are identical and the load is equally shared, the effective stiffness is roughly the sum of their individual stiffnesses in parallel, but without gaining the stiffness that would come from a composite section. For two identical lamellas each with moment of inertia I_0, and no shear coupling, the effective bending stiffness is simply twice I_0 because they do not gain extra stiffness by acting as a taller section. for the 4 layered beam , the logic follows.

In that case:

for 2 layered beam :

$$\delta_{\max} = \frac{P\,a(3L^2 - 4a^2)}{24E(2I_0)} = \frac{P\,a(3L^2 - 4a^2)}{48EI_0}$$

for 4 layered beam :

$$\delta_{\max} = \frac{P\,a(3L^2 - 4a^2)}{24E(4I_0)} = \frac{P\,a(3L^2 - 4a^2)}{96EI_0}$$

- Allowable bending stress: $\sigma_{\text{allow}} = 28N/mm^2$
- Beam span: $L = 4000mm$
- Timber grade: D70, with an approximate mean modulus of elasticity: taking the mean value of MOE

$$E_{0,mean} \approx 21000N/mm^2.$$

We consider a four-point bending setup with two loads P placed at one-third points of the span. Thus the distance from each support to the load is $a = L/3$.

C.7. calculations

- Allowable bending stress: $\sigma_{\text{allow}} = 28N/mm^2$
- Allowable shear stress: $\tau_{\text{allow}} = 2N/mm^2$
- Beam span: $L = 4000mm$
- Timber grade D70: $E_{0,mean} \approx 21000N/mm^2$ (for deflection calculations)
- Four-point bending with loads P at $\frac{L}{3}$ from each support.

C.8. Formulas

C.8.1. Bending Capacity

For a rectangular cross section of width b and height h:

$$I = \frac{bh^3}{12}, \quad y = \frac{h}{2}.$$

The bending stress in the upper and lower extreme fibres is:

$$\sigma = \frac{My}{I}.$$

Given $M = P * \frac{L}{3}$ (for loads at one-third points) and σ_{allow}:

$$\sigma_{\text{allow}} = \frac{M\frac{h}{2}}{bh^3/12} \implies \sigma_{\text{allow}} = \frac{6M}{bh^2}.$$

Thus:

$$M = \frac{\sigma_{\text{allow}} bh^2}{6}.$$

Since $M = P\frac{L}{3}$:

$$P\frac{L}{3} = \frac{\sigma_{\text{allow}} bh^2}{6} \implies P = \frac{\sigma_{\text{allow}} bh^2}{2L}.$$

Substitute $\sigma_{\text{allow}} = 28\,\text{N/mm}^2$:

$$P = \frac{28bh^2}{2L} = \frac{14bh^2}{L}.$$

C.8.2. Shear Capacity

For a single rectangular cross section, the maximum shear stress τ is:

$$\tau_{\max} = \frac{3V}{2bh}$$

where V is the shear force.

In this loading scenario, the maximum shear occurs in the supports. The total load is $2P$, and each support reaction is $R = P$. Thus, the maximum shear force $V = P$.

The allowable shear stress gives:

$$\tau_{\text{allow}} = \frac{3P}{2bh}.$$

So:

$$\tau_{\text{allow}} \implies 2 = \frac{3P}{2bh} \implies P = \frac{2bh \cdot 2}{3} = \frac{4}{3}bh.$$

From shear:

$$P_{\text{shear}} = \frac{4}{3}bh.$$

C.8.3. Deflection Under Four-Point Bending

As derived previously, for two equal loads P at the one-third points:

$$\delta_{\max} = \frac{Pa(3L^2 - 4a^2)}{24EI}, \quad a = \frac{L}{3}.$$

Substituting $a = L/3$ yields:

$$L^3 - 4a^2L + 4a^3 = 0.7037L^3,$$

so:

$$\delta_{\max} \approx \frac{23PL^3}{648EI} \approx 0.035494\frac{PL^3}{EI}.$$

C.8.4. Case 1: Single Lamella 140×140 mm

$$b = 140mm, \quad h = 140mm, \quad L = 4000mm.$$

Bending Limit

$$P_{\text{bend}} = \frac{14bh^2}{L} = \frac{14 \times 140 \times 140^2}{4000}.$$

Calculate $h^2 = 140^2 = 19600$:

$$bh^2 = 140 \times 19600 = 2{,}744{,}000.$$

Thus:

$$P_{\text{bend}} = \frac{14 \times 2{,}744{,}000}{4000} = \frac{38{,}416{,}000}{4000} = 9{,}604\,\text{N}.$$

Shear Limit

$$P_{\text{shear}} = \frac{4}{3}bh = \frac{4}{3} \times 140 \times 140.$$

$$140 \times 140 = 19{,}600.$$

So:

$$P_{\text{shear}} = \frac{4}{3} \times 19{,}600 = \frac{4 \times 19{,}600}{3} = \frac{78{,}400}{3} \approx 26{,}133.3\,\text{N}.$$

Shear capacity (26,133.3 N) is greater than bending capacity (9,604 N), so bending governs.

$$P_{\text{max}} = 9{,}604\,\text{N}.$$

Substitute $\sigma_{\text{allow}} = 28N/mm^2$, $b = 140mm$, $h = 70mm$, and $L = 4000mm$:

$$h^2 = 70^2 = 4900.$$

$$bh^2 = 140 \times 4900 = 686{,}000.$$

Thus:

$$P_{\text{bend}} = \frac{14 \times 686{,}000}{4000} = \frac{9{,}604{,}000}{4000} = 2{,}401\,\text{N}.$$

Shear Capacity

For a rectangular section, maximum shear stress τ_{max} is:

$$\tau_{\text{max}} = \frac{3V}{2bh},$$

where V is the shear force. Under symmetrical loading,

$$V_{\text{max}} = R = P \quad \text{(each support reaction)}.$$

The allowable shear stress condition:

$$\tau_{\text{allow}} = \frac{3P}{2bh}.$$

Given $\tau_{\text{allow}} = 2N/mm^2$:

$$2 = \frac{3P}{2bh} \implies P = \frac{2bh \cdot 2}{3} = \frac{4bh}{3}.$$

Substitute $b = 140\,\text{mm}$ and $h = 70\,\text{mm}$:

$$bh = 140 \times 70 = 9{,}800.$$

$$P_{\text{shear}} = \frac{4 \times 9{,}800}{3} = \frac{39{,}200}{3} \approx 13{,}066.7\,\text{N}.$$

C.8.5. Case 2: Single Lamella 140×70 mm

Compare bending and shear capacities:

$$P_{\text{bend}} = 2{,}401\,\text{N}, \quad P_{\text{shear}} \approx 13{,}067\,\text{N}.$$

Bending is more restrictive:

$$P_{\text{max}} = P_{\text{bend}} = 2{,}401\,\text{N}.$$

Deflection at Maximum Load

The second moment of area:

$$I = \frac{bh^3}{12} = \frac{140 \times 70^3}{12}.$$

Compute 70^3:

$$70^3 = 343{,}000.$$

Thus:

$$I = \frac{140 \times 343{,}000}{12} = \frac{48{,}020{,}000}{12} = 4{,}001{,}666.7\,\text{mm}^4.$$

The maximum deflection for loads at one-third points:

$$\delta_{\max} \approx 0.01466 \frac{PL^3}{EI}.$$

$$L^3 = 4000^3 = 64 \times 10^9 = 64 \times 10^9\,\text{mm}^3.$$

Substitute $P = 2{,}401\,\text{N}, E = 21{,}000\,\text{N/mm}^2, I = 4{,}001{,}666.7\,\text{mm}^4$:

$$\delta_{\max} \approx 0.01466 \frac{2{,}401 \times 64 \times 10^9}{21{,}000 \times 4{,}001{,}666.7}.$$

Evaluating this expression gives approximately:

$$\delta_{\max} \approx 26.8\,\text{mm}.$$

For a single lamella of $140 \times 70\,\text{mm}$:

$$P_{\text{bend}} = 2{,}401\,\text{N}, \quad P_{\text{shear}} = 13{,}067\,\text{N}.$$

Bending governs the allowable load:

$$P_{\max} = 2{,}401\,\text{N}.$$

At this load, the midspan deflection is about:

$$\delta_{\max} \approx 26.8\,\text{mm}.$$

C.9. Case 3: Two Lamellas (140x140 mm) Stacked, No Composite Action

Without composite action, each lamella still has the same bending and shear limits as a single lamella. Stacking does not effectively increase the bending or shear capacity if there is no connection, because each lamella would be stressed similarly. Thus, the same limiting load P applies:

$$P_{\max} = 9{,}604\,\text{N} \quad \text{(from bending)}.$$

Shear is not governing since it allows much more load.

C.10. Case 4: Four Lamellas (140x70 mm) Stacked, No Composite Action

For one lamella $b = 140\,\text{mm}, h = 70\,\text{mm}$:

Bending Limit

$$P_{\text{bend}} = \frac{14bh^2}{L} = \frac{14 \times 140 \times 70^2}{4000}.$$

Compute $70^2 = 4900$:

$$bh^2 = 140 \times 4900 = 686{,}000.$$

Thus:

$$P_{\text{bend}} = \frac{14 \times 686{,}000}{4000} = \frac{9{,}604{,}000}{4000} = 2{,}401\,\text{N}.$$

Shear Limit

$$P_{\text{shear}} = \frac{4}{3}bh = \frac{4}{3} \times 140 \times 70.$$

Compute $140 \times 70 = 9{,}800$:

$$P_{\text{shear}} = \frac{4 \times 9{,}800}{3} = \frac{39{,}200}{3} \approx 13{,}066.7\,\text{N}.$$

Again, shear capacity ($\approx$ 13,067 N) is higher than bending capacity (2,401 N), so bending governs:

$$P_{\text{max}} = 2{,}401\,\text{N}.$$

C.11. Deflection at Maximum Load (Case 1 as Example)

For Case 1:

$$I = \frac{bh^3}{12} = \frac{140 \times 140^3}{12}.$$

$$140^3 = 2{,}744{,}000, \quad I = \frac{140 \times 2{,}744{,}000}{12} = \frac{384{,}160{,}000}{12} = 32{,}013{,}333.3\,\text{mm}^4.$$

At $P_{\text{max}} = 9{,}604\,\text{N}$:

$$\delta_{\text{max}} \approx 0.01466 \frac{PL^3}{EI}.$$

$$L^3 = 4000^3 = 64 \times 10^9\,\text{mm}^3.$$

Substitute $E = 21{,}000\,\text{N/mm}^2$, $I = 32{,}013{,}333.3\,\text{mm}^4$:

$$\delta_{\text{max}} \approx 0.01466 \frac{9{,}604 \times 64 \times 10^9}{21{,}000 \times 32{,}013{,}333.3}.$$

Numerically:

$$EI = 21{,}000 \times 32{,}013{,}333.3 \approx 6.7 \times 10^{11}\,\text{N} \cdot \text{mm}^2,$$

$$9{,}604 \times 64 \times 10^9 \approx 6.14656 \times 10^{14}.$$

$$\delta_{\max} \approx 0.01466 \times \frac{6.14656 \times 10^{14}}{6.7 \times 10^{11}} \approx 0.01466 \times 916 \approx 13.4\,\text{mm}.$$

Thus, the deflection at maximum load for the single 140×140 mm lamella is about $13.4mm$.

C.12. Conclusion

Case 1 (Single 140×140 mm):

$$P_{\text{bend}} = 9{,}604\,\text{N}, \quad P_{\text{shear}} \approx 26{,}133\,\text{N} \implies P_{\max} = 9{,}604\,\text{N}.$$

Deflection at

$$P_{\max} \approx 13.4\,\text{mm}.$$

Case 3 (Two 140×140 mm Stacked, No Composite):** Bending still governs:

$$P_{\max} = 9{,}604\,\text{N}.$$

Deflection was roughly doubled from the single-lamella scenario at the same load.

C.12.1. Case 3

(Four 140×70 mm Stacked, No Composite)

$$P_{\text{bend}} = 2{,}401\,\text{N}, \quad P_{\text{shear}} \approx 13{,}067\,\text{N} \implies P_{\max} = 2{,}401\,\text{N}.$$

(Deflection would be about four times the single lamella (140×70) deflection at this load)

C.13. Calculating the Modulus of Elasticity (MOE)

If you have experimental data for the deflection $\delta_{\max}$ under a known load P, you can rearrange the deflection formula to solve for E:

$$E = \frac{Pa(3L^2 - 4a^2)}{24\delta_{\max} IL}$$

By measuring $\delta_{\max}$ during your test and knowing P, you can calculate the MOE to ensure the member remains elastic.

The bending stress has two components.

Moment Component, $\sigma_{i,m}$

$$\sigma_{i,m} = \frac{M}{(EI)_{ef}} E_i \frac{h_i}{2}$$

Normal Force Component, $\sigma_{i,t(c)}$

$$\sigma_{i,t(c)} = \frac{M}{(EI)_{ef}} \gamma_1 E_i a_i$$

Total Bending Stress

$$\sigma_B = \frac{M}{(EI)_{ef}} E_i \left(\frac{h_i}{2} + \gamma_1 a_i \right)$$

For a 4-layered Beam

Following the same principle but accounting for multiple layers and interfaces, the bending stress is given by:

$$\sigma_B = \frac{M}{(EI)_{ef}} E_i \left(\frac{h_i}{2} + \gamma_1 a_i \right)$$

Let's solve this step by step using the formula:

$$\sigma_B = \frac{M}{(EI)_{ef}} E_i \left(\frac{h_i}{2} + \gamma_1 a_i \right)$$

Given:

- Target stress: $\sigma_B = 25\,\text{MPa} = 25\,\text{N/mm}^2$
- Effective bending stiffness: $(EI)_{ef} = 2{,}209{,}142{,}991{,}708.122\,\text{N} \cdot \text{mm}^2$
- $\gamma_1 = 0.38102449$
- Modulus of elasticity: $E = 16{,}100\,\text{MPa} = 16{,}100\,\text{N/mm}^2$
- $h_i = 140\,\text{mm}$
- $a_i = 70\,\text{mm}$
- For 3-point bending: $M = \frac{P\,L}{4}$

Rearrange the equation to solve for M:

$$25 = \frac{M}{2{,}209{,}142{,}991{,}708.122} \cdot 16100 \cdot \left(\frac{140}{2} + 0.38102449 \cdot 70 \right)$$

Notice that:

$$\frac{140}{2} = 70 \quad \text{and} \quad 0.38102449 \cdot 70 \approx 26.67171.$$

Thus, the equation becomes:

$$25 = \frac{M}{2{,}209{,}142{,}991{,}708.122} \cdot 16100 \cdot (70 + 26.67171)$$

or

$$25 = \frac{M}{2{,}209{,}142{,}991{,}708.122} \cdot 16100 \cdot 96.67171.$$

Solving for M, we obtain:

$$M = \frac{25 \times 2{,}209{,}142{,}991{,}708.122}{16100 \times 96.67171}.$$

Evaluating the expression yields:

$$M \approx 35{,}714{,}285.71\,\text{N} \cdot \text{mm}.$$

For 3-point bending, the moment is related to the applied load P by:

$$M = \frac{P\,L}{4} \quad \text{with } L = 3600\,\text{mm}.$$

Thus,

$$35{,}714{,}285.71 = \frac{P \times 3600}{4}.$$

Solving for P:

$$P = \frac{35{,}714{,}285.71 \times 4}{3600},$$
$$P \approx 39{,}682.54\,\text{N},$$

or approximately,

$$P \approx 39.68\,\text{kN}.$$

We start with the bending stress formula

$$\sigma_B = \frac{M}{(EI)_{ef}}\, E_i \left(\frac{h_i}{2} + \gamma_1\, a_i\right),$$

and substitute the given values:

$$\begin{aligned} \sigma_B &= 25\ \text{MPa} = 25\ \text{N/mm}^2, \\ (EI)_{ef} &= 1.924 \times 10^{12}\ \text{N} \cdot \text{mm}^2, \\ \gamma_1 &= 0.435, \\ E_i &= 16{,}100\ \text{N/mm}^2, \\ h_i &= 70\ \text{mm}, \\ a_i &= 105\ \text{mm}. \end{aligned}$$

For 3-point bending, the moment is given by

$$M = \frac{P\,L}{4},$$

with $L = 3600$ mm.

Step 1. Substitute the values into the stress equation:

$$25 = \frac{M}{1.924 \times 10^{12}} \cdot 16100 \cdot \left(\frac{70}{2} + 0.435 \cdot 105\right).$$

Step 2. Simplify the terms in parentheses:

$$\frac{70}{2} = 35 \quad \text{and} \quad 0.435 \times 105 = 45.675.$$

Thus,

$$35 + 45.675 = 80.675.$$

So the equation becomes:

$$25 = \frac{M}{1.924 \times 10^{12}} \cdot 16100 \cdot 80.675.$$

Step 3. Solve for M:

$$M = \frac{25 \times 1.924 \times 10^{12}}{16100 \times 80.675}.$$

Evaluating this expression gives:

$$M \approx 37{,}142{,}857.14 \text{ N} \cdot \text{mm}.$$

Step 4. Determine the load P for 3-point bending:

Using

$$M = \frac{P\,L}{4},$$

with $L = 3600$ mm, we have:

$$37{,}142{,}857.14 = \frac{P \times 3600}{4}.$$

Solving for P:

$$P = \frac{37{,}142{,}857.14 \times 4}{3600} \approx 41{,}269.84 \text{ N}.$$

Expressed in kilonewtons,

$$P \approx 41.27 \text{ kN}.$$

We wish to calculate the maximum deflection, $\delta_{\max}$, under 3-point bending using the formula:

$$\delta_{\max} = \frac{PL^3}{48(EI)_{\text{eff}}}.$$

For the 2-Layered Beam

Given:

- $P = 39682.54N$
- $L = 3600mm$
- $(EI)_{\text{eff}} = 2.209 \times 10^{12}\, N \cdot mm^2$

First, compute:

$$L^3 = 3600^3 = 46{,}656{,}000{,}000\ mm^3.$$

Substitute into the deflection formula:

$$\delta_{\max} = \frac{39682.54 \times 46{,}656{,}000{,}000}{48 \times 2.209 \times 10^{12}}.$$

Notice that:

$$48 \times 2.209 \times 10^{12} = 106.032 \times 10^{12}.$$

Thus, the deflection is:

$$\delta_{\max} = \frac{39682.54 \times 46{,}656{,}000{,}000}{106.032 \times 10^{12}} \approx 17.48mm.$$

For the 4-Layered Beam

Given:

- $P = 41269.84N$
- $L = 3600mm$
- $(EI)_{\text{eff}} = 1.924 \times 10^{12}\, N \cdot mm^2$

Again, with:

$$L^3 = 3600^3 = 46{,}656{,}000{,}000\ mm^3,$$

the deflection formula becomes:

$$\delta_{\max} = \frac{41269.84 \times 46{,}656{,}000{,}000}{48 \times 1.924 \times 10^{12}}.$$

Here, the denominator evaluates to:

$$48 \times 1.924 \times 10^{12} = 92.352 \times 10^{12}.$$

So,

$$\delta_{\max} = \frac{41269.84 \times 46{,}656{,}000{,}000}{92.352 \times 10^{12}} \approx 20.81mm.$$

/

C.14. Analytical calculation of effective stiffness of Mechanically Jointed Azobe Beam

Basic Parameters Each layer is 70 mm high Total height is 280 mm (4 layers) The center line of the beam is between layers 2 and 3 Width (b) = 140 mm

General Formulas Distance (a_i) from each layer's center to the overall beam center Area of each layer: $A = b \cdot h = 140 \cdot 70 = 9,800$ mm^2 Second moment of area for each layer: $I_i = \frac{bh^3}{12} = \frac{140 \cdot 70^3}{12} = 4,001,666.7$ mm^4

C.14.1. Calculation of Effective Flexural Rigidity $(EI)_{\text{eff}}$

The effective flexural rigidity is given by:

$$(EI)_{\text{eff}} = \sum_{i=1}^{n} (E_i I_i + \gamma_i E_i A_i a_i^2)$$

Where: - E_i is the modulus of elasticity for layer i - I_i is the second moment of area for layer i - γ_i is the shear correction factor for layer i - A_i is the cross-sectional area of layer i - a_i is the distance from the center of layer i to the neutral axis

Beam Arrangements

Beam A1 This arrangement has the stiffest lamella at the lower middle of the arrangement. - Top Layer: Y1 (15,200 N/mm²) - Bottom Layer: Y2 (16,100 N/mm²)

Beam A2 This arrangement has the stiffest lamella at the lower middle of the arrangement. - Top Layer: Y6 (15,200 N/mm²) - Bottom Layer: Y4 (16,000 N/mm²)

Beam B1-1 This arrangement has the stiffest lamella at the very bottom of the arrangement. - Top Layer: X8 (15,700 N/mm²) - Upper Middle Layer: X6 (15,400 N/mm²) - Lower Middle Layer: X10 (15,000 N/mm²) - Bottom Layer: X4 (18,100 N/mm²)

Beam B2-2 This arrangement has the stiffest lamella at the lower middle of the arrangement. - Top Layer (1): X7 (15,300 N/mm²) - Upper Middle Layer (2): X1 (14,400 N/mm²) - Lower Middle Layer (3): X3 (19,100 N/mm²) - Bottom Layer (4): X2 (15,500 N/mm²)

Detailed Calculations for Beam B2-2

Layer distances from neutral axis: - $a_1 = 105$ mm (furthest top layer) - $a_2 = 35$ mm (second layer) - $a_3 = 35$ mm (third layer) - $a_4 = 105$ mm (bottom layer)

Layer 1 (Top): - $E_1 I_1 = 15,300 \times 4,001,666.7 = 6.122 \times 10^{10}$ Nmm^2 - $\gamma_1 E_1 A_1 a_1^2 = 0.435 \times 15,300 \times 9,800 \times 105^2 = 7.324 \times 10^{10}$ Nmm^2

Layer 2 (Upper Middle): - $E_2 I_2 = 14,400 \times 4,001,666.7 = 5.762 \times 10^{10}$ Nmm^2 - $\gamma_2 E_2 A_2 a_2^2 = 0.344 \times 14,400 \times 9,800 \times 35^2 = 5.373 \times 10^9$ Nmm^2

Layer 3 (Lower Middle): - $E_3 I_3 = 19,100 \times 4,001,666.7 = 7.643 \times 10^{10}$ Nmm^2 - $\gamma_3 E_3 A_3 a_3^2 = 0.344 \times 19,100 \times 9,800 \times 35^2 = 7.128 \times 10^9$ Nmm^2

Layer 4 (Bottom): - $E_4 I_4 = 15,500 \times 4,001,666.7 = 6.203 \times 10^{10}$ Nmm^2 - $\gamma_4 E_4 A_4 a_4^2 = 0.435 \times 15,500 \times 9,800 \times 105^2 = 7.419 \times 10^{10}$ Nmm^2

Sum of all components:

$$(EI)_{ef} = \sum_{i=1}^{4} (E_i I_i + \gamma_i E_i A_i a_i^2)$$

$$(EI)_{ef} = 4.173 \times 10^{11} \text{ Nmm}^2$$

Detailed Calculations for Beam B1-1

Layer 1 (Top): - $E_1 I_1 = 15,700 \times 4,001,666.7 = 6.283 \times 10^{10}$ Nmm^2 - $\gamma_1 E_1 A_1 a_1^2 = 0.435 \times 15,700 \times 9,800 \times 105^2 = 7.514 \times 10^{10}$ Nmm^2

Layer 2 (Upper Middle): - $E_2 I_2 = 15,400 \times 4,001,666.7 = 6.163 \times 10^{10}$ Nmm^2 - $\gamma_2 E_2 A_2 a_2^2 = 0.344 \times 15,400 \times 9,800 \times 35^2 = 5.747 \times 10^9$ Nmm^2

Layer 3 (Lower Middle): - $E_3 I_3 = 15,000 \times 4,001,666.7 = 6.003 \times 10^{10}$ Nmm^2 - $\gamma_3 E_3 A_3 a_3^2 = 0.344 \times 15,000 \times 9,800 \times 35^2 = 5.597 \times 10^9$ Nmm^2

Layer 4 (Bottom): - $E_4 I_4 = 18,100 \times 4,001,666.7 = 7.243 \times 10^{10}$ Nmm^2 - $\gamma_4 E_4 A_4 a_4^2 = 0.435 \times 18,100 \times 9,800 \times 105^2 = 8.665 \times 10^{10}$ Nmm^2

Sum of all components:

$$(EI)_{ef} = \sum_{i=1}^{4} (E_i I_i + \gamma_i E_i A_i a_i^2)$$

$$(EI)_{ef} = 4.301 \times 10^{11} \text{ Nmm}^2$$

D

ANNEX 3

D.1. Calculating the Modulus of Elasticity (MOE)

If you have experimental data for the deflection $\delta_{\max}$ under a known load P, you can rearrange the deflection formula to solve for E:

$$E = \frac{Pa(3L^2 - 4a^2)}{24\delta_{\max} IL}$$

By measuring $\delta_{\max}$ during your test and knowing P, you can calculate the MOE to ensure the member remains elastic.

D.1.1. The bending stress has two components

Moment Component, $\sigma_{i,m}$

$$\sigma_{i,m} = \frac{M}{(EI)_{ef}} E_i \frac{h_i}{2}$$

Normal Force Component, $\sigma_{i,t(c)}$

$$\sigma_{i,t(c)} = \frac{M}{(EI)_{ef}} \gamma_1 E_i a_i$$

Total Bending Stress

$$\sigma_B = \frac{M}{(EI)_{ef}} E_i \left(\frac{h_i}{2} + \gamma_1 a_i \right)$$

For a 4-layered Beam

Following the same principle but accounting for multiple layers and interfaces, the bending stress is given by:

$$\sigma_B = \frac{M}{(EI)_{ef}} E_i \left(\frac{h_i}{2} + \gamma_1 a_i \right)$$

Let's solve this step by step using the formula:

$$\sigma_B = \frac{M}{(EI)_{ef}} E_i \left(\frac{h_i}{2} + \gamma_1 a_i \right)$$

Given:

- Target stress: $\sigma_B = 25$ MPa
- Effective bending stiffness: $(EI)_{\text{eff}} = 2.209 \times 10^{12}$ N $\cdot$ mm^2
- For outermost layer: $\gamma_1 = 0.38102449$
- Modulus of elasticity: $E = 16100$ N/mm^2
- $h_i = 140$ mm
- $a_i = 70$ mm
- For 3-point bending: $M = \frac{P\,L}{4}$

Rearrange the equation to solve for M:

$$25 = \frac{M}{2{,}209{,}142{,}991{,}708.122} \cdot 16100 \cdot \left(\frac{140}{2} + 0.38102449 \cdot 70 \right)$$

Notice that:

$$\frac{140}{2} = 70 \quad \text{and} \quad 0.38102449 \cdot 70 \approx 26.67171.$$

Thus, the equation becomes:

$$25 = \frac{M}{2{,}209{,}142{,}991{,}708.122} \cdot 16100 \cdot (70 + 26.67171)$$

Solving for M, we obtain the following:

$$M \approx 35{,}714{,}285.71\,\text{N} \cdot \text{mm}.$$

For 3-point bending, the moment is related to the applied load P by:

$$M = \frac{P\,L}{4} \quad \text{with } L = 3600\,\text{mm}.$$

Thus,

$$35{,}714{,}285.71 = \frac{P \times 3600}{4}.$$

Solving for P:

$$P \approx 39.68\,\text{kN}.$$

We start with the bending stress formula

$$\sigma_B = \frac{M}{(EI)_{ef}}\, E_i \left(\frac{h_i}{2} + \gamma_1\, a_i \right),$$

and substitute the given values:

$$\begin{aligned} \sigma_B &= 25\ \text{MPa} = 25\ \text{N/mm}^2, \\ (EI)_{ef} &= 1.924 \times 10^{12}\ \text{N} \cdot \text{mm}^2, \\ \gamma_1 &= 0.435, \\ E_i &= 16{,}100\ \text{N/mm}^2, \\ h_i &= 70\ \text{mm}, \\ a_i &= 105\ \text{mm}. \end{aligned}$$

For 3-point bending, the moment is given by

$$M = \frac{P\,L}{4},$$

with $L = 3600$ mm.

Step 1. Substitute the values into the stress equation:

$$25 = \frac{M}{1.924 \times 10^{12}} \cdot 16100 \cdot \left(\frac{70}{2} + 0.435 \cdot 105 \right).$$

Step 2. Simplify the terms in parentheses:

$$\frac{70}{2} = 35 \quad \text{and} \quad 0.435 \times 105 = 45.675.$$

Thus,

$$35 + 45.675 = 80.675.$$

So the equation becomes:

$$25 = \frac{M}{1.924 \times 10^{12}} \cdot 16100 \cdot 80.675.$$

Step 3. Solve for M:

$$M = \frac{25 \times 1.924 \times 10^{12}}{16100 \times 80.675}.$$

Evaluating this expression gives:

$$M \approx 37{,}142{,}857.14\ \text{N} \cdot \text{mm}.$$

Step 4. Determine the load P for 3-point bending:

Using

$$M = \frac{P\,L}{4},$$

with $L = 3600$ mm, we have:

$$37{,}142{,}857.14 = \frac{P \times 3600}{4}.$$

Solving for P:

$$P = \frac{37{,}142{,}857.14 \times 4}{3600} \approx 41{,}269.84\ \text{N}.$$

Expressed in kilonewtons,

$$P \approx 41.27 \text{ kN}.$$

We wish to calculate the maximum deflection, $\delta_{\max}$, under 3-point bending using the formula:

$$\delta_{\max} = \frac{PL^3}{48(EI)_{\text{eff}}}.$$

For the 2-Layered Beam

Given:

- $P = 39682.54N$
- $L = 3600mm$
- $(EI)_{\text{eff}} = 2.209 \times 10^{12} \, \text{N} \cdot \text{mm}^2$

First, compute:

$$L^3 = 3600^3 = 46{,}656{,}000{,}000 \text{ mm}^3.$$

Substitute into the deflection formula:

$$\delta_{\max} = \frac{39682.54 \times 46{,}656{,}000{,}000}{48 \times 2.209 \times 10^{12}}.$$

Notice that:

$$48 \times 2.209 \times 10^{12} = 106.032 \times 10^{12}.$$

Thus, the deflection is:

$$\delta_{\max} = \frac{39682.54 \times 46{,}656{,}000{,}000}{106.032 \times 10^{12}} \approx 17.48mm.$$

For the 4-Layered Beam

- $P = 41269.84N$
- $L = 3600mm$
- $(EI)_{\text{eff}} = 1.924 \times 10^{12} \, \text{N} \cdot \text{mm}^2$

Again, with:

$$L^3 = 3600^3 = 46{,}656{,}000{,}000 \text{ mm}^3,$$

the deflection formula becomes:

$$\delta_{\max} = \frac{41269.84 \times 46{,}656{,}000{,}000}{48 \times 1.924 \times 10^{12}}.$$

Here, the denominator evaluates to:

$$48 \times 1.924 \times 10^{12} = 92.352 \times 10^{12}.$$

So,

$$\delta_{\max} = \frac{41269.84 \times 46{,}656{,}000{,}000}{92.352 \times 10^{12}} \approx 20.81mm.$$

D.2. Equations for the kser values and gamma values reverse engineered

D.2.1. K_{ser} Equation Derivation for Two-Layered Beam

For a two-layered beam, the effective stiffness is given by:

$$(EI)_{\text{eff}} = E_1 I_1 + E_2 I_2 + \gamma\big(E_1 A_1 a_1^2 + E_2 A_2 a_2^2\big). \tag{D.1}$$

The factor γ can be extracted from the experimental results:

$$\gamma = \frac{(EI)_{\text{eff}} - \big(E_1 I_1 + E_2 I_2\big)}{E_1 A_1 a_1^2 + E_2 A_2 a_2^2}. \tag{D.2}$$

For two identical layers with spacing s, the relationship between γ and k_{ser} is:

$$\gamma = 1 + \frac{\pi^2\, E\, A\, s}{K_{\text{ser}}\, L^2}. \tag{D.3}$$

Solving for k_{ser}:

$$k_{\text{ser}} = \frac{\pi^2\, E\, A\, s}{\big(\frac{1}{\gamma} - 1\big)\, L^2}. \tag{D.4}$$

for the 2 layers with different elastic moduli, a more precise formula is:

$$k_{\text{ser}} = \frac{\pi^2 s}{L^2} \cdot \frac{E_1 A_1 \cdot E_2 A_2}{E_1 A_1 + E_2 A_2} \left(\frac{1}{\frac{1}{\gamma} - 1} \right). \tag{D.5}$$

D.2.2. K_{ser} Equation Derivation for Four-Layered Beam

Let us start with the effective stiffness equation for a four-layered beam:

$$(EI)_{\text{eff}} = \sum_{i=1}^{4} E_i I_i + \gamma_1 E_1 A_1 a_1^2 + \gamma_2 E_2 A_2 a_2^2 + \gamma_3 E_3 A_3 a_3^2 + \gamma_4 E_4 A_4 a_4^2. \tag{D.6}$$

the relationships for the γ_i factors according to Schelling :

$$\gamma_2 = \gamma_3 = \frac{1}{2K^2 - 1}, \tag{D.7}$$

$$\gamma_1 = \gamma_4 = \frac{2K + 1}{3\,(2K^2 - 1)}. \tag{D.8}$$

The parameter K is then defined as:

$$K = 1 + \frac{\pi^2\, E\, A_1}{l^2 \,\cdot\, 2 \,\cdot\, \frac{k_{\text{ser}}}{s}} = 1 + \frac{\pi^2\, E\, A_1\, s}{l^2 \,\cdot\, 2 \,\cdot\, k_{\text{ser}}}. \tag{D.9}$$

Introduction of auxillary constants

Define the following constants:

$$\sum_{i=1}^{4} E_i I_i \;=\; (EI)_0, \qquad E_1 A_1 a_1^2 + E_4 A_4 a_4^2 \;=\; C_1, \qquad E_2 A_2 a_2^2 + E_3 A_3 a_3^2 \;=\; C_2.$$

Then the effective stiffness equation becomes:

$$(EI)_{\text{eff}} = (EI)_0 + \frac{(2K+1)}{3\,(2K^2-1)}\,C_1 + \frac{1}{2K^2-1}\,C_2. \tag{D.10}$$

Rearrange this to isolate the terms involving K. First, let

$$\Delta EI = (EI)_{\text{eff}} - (EI)_0.$$

Hence,

$$\Delta EI = \frac{1}{2K^2-1}\left[\frac{(2K+1)}{3}\,C_1 + C_2\right]. \tag{D.11}$$

Multiply both sides by $(2K^2-1)$ to get:

$$\Delta EI\,\left(2K^2-1\right) = \frac{(2K+1)}{3}\,C_1 + C_2. \tag{D.12}$$

Rewrite the above in standard polynomial form:

$$2\,\Delta EI\,K^2 - \Delta EI = \frac{2K\,C_1}{3} + \frac{C_1}{3} + C_2.$$

Collect like terms to form a quadratic $aK^2 + bK + c = 0$:

$$2\,\Delta EI\,K^2 - \frac{2C_1}{3}\,K - \left(\Delta EI + \frac{C_1}{3} + C_2\right) = 0.$$

Identifying coefficients:

$$a = 2\,\Delta EI, \quad b = -\frac{2\,C_1}{3}, \quad c = -\left(\Delta EI + \frac{C_1}{3} + C_2\right).$$

The solution for K is:

$$K = \frac{-\,b \,\pm\, \sqrt{b^2-4ac}}{2a}. \tag{D.13}$$

Since K is a physical parameter and must be positive, we typically take the positive root.

D.2.3. Final Expression for k_{ser}

Once K is found, we can compute K_{ser} using:

$$k_{\text{ser}_{1,2}} = k_{\text{ser}_{3,4}}, \tag{D.14}$$

$$\tag{D.15}$$

$$k_{\text{ser}_{1,2}} = \frac{\pi^2\,E_{1,2}\,A_{1,2}\,s}{2\,l^2\,(K-1)}, \tag{D.16}$$

$$\tag{D.17}$$

$$k_{\text{ser}_{2,3}} = \frac{\pi^2\,E_{2,3}\,A_{2,3}\,s}{2\,l^2\,(K-1)}. \tag{D.18}$$

This provides a direct method to obtain k_{ser} from the experimentally determined $(EI)_{\text{eff}}$ for a four-layered beam.

D.2.4. Quadratic Equation in K

We define:

$$a = 2\,\Delta EI,$$
$$b = -\frac{2\,C_1}{3},$$
$$c = -\Big(\Delta EI + \frac{C_1}{3} + C_2\Big).$$

The solution for K follows the standard quadratic formula:

$$K = \frac{-b \pm \sqrt{b^2 - 4\,a\,c}}{2\,a}.$$

D.2.5. Required Quantities

$$(EI)_0 = \sum_{i=1}^{4} E_i\, I_i,$$

$$C_1 = E_1 A_1 a_1^2 \;+\; E_4 A_4 a_4^2,$$

$$C_2 = E_2 A_2 a_2^2 \;+\; E_3 A_3 a_3^2,$$

$$\Delta EI = (EI)_{\text{eff}} \;-\; (EI)_0.$$

D.3. Slip Modulus K_{ser} Calculations for the Mechanically Jointed Azobe Beams

D.3.1. Two-Layered Beam (A1)

The two-layered beam consists of two lamellae (Y1 and Y2) with dimensions 140 mm × 140 mm each.

Material Properties

$$E_1 = 24,439 \text{ MPa (Y1)} \tag{D.19}$$
$$E_2 = 23,807 \text{ MPa (Y2)} \tag{D.20}$$
$$\tag{D.21}$$

Section Properties

For each layer (140 mm × 140 mm):

$$A = 140 \times 140 = 19,600 \text{ mm}^2 \tag{D.22}$$
$$\tag{D.23}$$
$$I = \frac{140 \times 140^3}{12} = 32,006,667 \text{ mm}^4 \tag{D.24}$$

Individual Layer Stiffness

$$(EI)_1 = E_1 \times I_1 = 24,439 \times 32,006,667 = 7.82 \times 10^{11}\ \text{N} \cdot \text{mm}^2 \tag{D.25}$$

(D.26)

$$(EI)_2 = E_2 \times I_2 = 23,807 \times 32,006,667 = 7.62 \times 10^{11}\ \text{N} \cdot \text{mm}^2 \tag{D.27}$$

(D.28)

$$(EI)_0 = (EI)_1 + (EI)_2 = 1.54 \times 10^{12}\ \text{N} \cdot \text{mm}^2 \tag{D.29}$$

Neutral Axis Position

Assuming origin at the bottom of the beam:

$$y_1 = 210\ \text{mm (centroid of top layer)} \tag{D.30}$$

$$y_2 = 70\ \text{mm (centroid of bottom layer)} \tag{D.31}$$

(D.32)

$$\bar{y} = \frac{E_1 A_1 y_1 + E_2 A_2 y_2}{E_1 A_1 + E_2 A_2} \tag{D.33}$$

(D.34)

$$= \frac{24,439 \times 19,600 \times 210 + 23,807 \times 19,600 \times 70}{24,439 \times 19,600 + 23,807 \times 19,600} \tag{D.35}$$

(D.36)

$$= 141.14\ \text{mm} \tag{D.37}$$

Distance from Layer Centroids to Neutral Axis

$$a_1 = |210 - 141.14| = 68.86\ \text{mm} \tag{D.38}$$

$$a_2 = |70 - 141.14| = 71.14\ \text{mm} \tag{D.39}$$

Composite Term Calculation

$$E_1 A_1 a_1^2 + E_2 A_2 a_2^2 = 24,439 \times 19,600 \times 68.86^2 + 23,807 \times 19,600 \times 71.14^2 \tag{D.40}$$

(D.41)

$$= 4.633 \times 10^{12}\ \text{N} \cdot \text{mm}^2 \tag{D.42}$$

Gamma Calculation

Given experimental $EI_{eff} = 2.33 \times 10^{12}\ \text{N} \cdot \text{mm}^2$:

$$\gamma = \frac{(EI)_{eff} - (EI)_0}{E_1 A_1 a_1^2 + E_2 A_2 a_2^2} \tag{D.43}$$

(D.44)

$$= \frac{2.33 \times 10^{12} - 1.54 \times 10^{12}}{4.63 \times 10^{12}} \tag{D.45}$$

(D.46)

$$= 0.171 \tag{D.47}$$

Slip Modulus Calculation

Given span length $L = 3600$ mm and fastener spacing $s = 200$ mm:

$$E_{avg} = \frac{E_1 A_1 + E_2 A_2}{A_1 + A_2} = 24,123 \text{ MPa} \tag{D.48}$$

$$\tag{D.49}$$

$$K_{ser} = \frac{\pi^2 E_{avg} A s}{L^2 \left(\frac{1}{\gamma} - 1\right)} \tag{D.50}$$

$$\tag{D.51}$$

$$= \frac{\pi^2 \times 24,123 \times 19,600 \times 200}{3600^2 \times \left(\frac{1}{0.171} - 1\right)} \tag{D.52}$$

$$\tag{D.53}$$

$$= 14854 \text{ N/mm} \tag{D.54}$$

D.3.2. Beam A2 (Y6Y4)

This is a two-layered beam with dimensions 140 mm × 140 mm per layer.

Input Parameters

:

$$\text{Top Layer (Y6)} : E_1 = 22,113 \text{ MPa} \tag{D.55}$$

$$\text{Bottom Layer (Y4)} : E_2 = 24,945 \text{ MPa} \tag{D.56}$$

Each layer: 140 mm × 140 mm, $EI_{eff} = 2.26 \times 10^{12}$ N · mm^2, $L = 3600$ mm, $s = 200$ mm

Section Properties

$$A = 140 \times 140 = 19,600 \text{ mm}^2 \tag{D.57}$$

$$I = \frac{140 \times 140^3}{12} = 32,013,333 \text{ mm}^4 \tag{D.58}$$

Individual Layer Stiffness

$$(EI)_0 = \sum_{i=1}^{2} E_i I_i \tag{D.59}$$

$$\tag{D.60}$$

$$= 22,113 \times 32,013,333 + 24,945 \times 32,013,333 \tag{D.61}$$

$$\tag{D.62}$$

$$= 1,507,123,494,414 \text{ N} \cdot \text{mm}^2 \tag{D.63}$$

Neutral Axis Position

Assuming origin at the bottom of the beam:

$$y_1 = 210 \text{ mm (centroid of top layer)} \tag{D.64}$$
$$y_2 = 70 \text{ mm (centroid of bottom layer)} \tag{D.65}$$
$$\tag{D.66}$$
$$\bar{y} = \frac{E_1 A_1 y_1 + E_2 A_2 y_2}{E_1 A_1 + E_2 A_2} \tag{D.67}$$
$$\tag{D.68}$$
$$= \frac{22,113 \times 19,600 \times 210 + 24,945 \times 19,600 \times 70}{22,113 \times 19,600 + 24,945 \times 19,600} \tag{D.69}$$
$$\tag{D.70}$$
$$= 136.0 \text{ mm} \tag{D.71}$$

Distance from Layer Centroids to Neutral Axis

$$a_1 = |210 - 136.0| = 74.0 \text{ mm} \tag{D.72}$$
$$a_2 = |70 - 136.0| = 66.0 \text{ mm} \tag{D.73}$$

Calculate γ

$$E_1 A_1 a_1^2 + E_2 A_2 a_2^2 = 22,113 \times 19,600 \times 74.0^2 + 24,945 \times 19,600 \times 66.0^2 \tag{D.74}$$
$$\tag{D.75}$$
$$= 4,506,830,281,600 \tag{D.76}$$

$$\gamma_{1,2} = \frac{EI_{eff} - (EI)_0}{E_1 A_1 a_1^2 + E_2 A_2 a_2^2} \tag{D.77}$$
$$\tag{D.78}$$
$$= \frac{2.26 \times 10^{12} - 1,507,123,494,414}{4,506,830,281,600} \tag{D.79}$$
$$\tag{D.80}$$
$$= 0.167 \tag{D.81}$$

Calculate (K_{ser})

$$E_{avg} = \frac{E_1 + E_2}{2} = \frac{22,113 + 24,945}{2} = 23,529 \text{ MPa} \tag{D.82}$$
$$\tag{D.83}$$
$$K_{ser} = \frac{\pi^2 \times E_{avg} \times A \times s}{L^2 \times \left(\frac{1}{\gamma} - 1\right)} \tag{D.84}$$
$$\tag{D.85}$$
$$= \frac{\pi^2 \times 23,529 \times 19,600 \times 200}{(3,600)^2 \times \left(\frac{1}{0.167} - 1\right)} \tag{D.86}$$
$$\tag{D.87}$$
$$= 14,082 \text{ N/mm} \tag{D.88}$$

D.3.3. Beam B1-1 (X8X6X10X4)

This is a four-layered beam with dimensions 140 mm × 70 mm per layer.

$$\text{Top Layer (X8)} : E_1 = 19,184 \text{ MPa} \tag{D.89}$$
$$\text{Upper Middle Layer (X6)} : E_2 = 19,335 \text{ MPa} \tag{D.90}$$
$$\text{Lower Middle Layer (X10)} : E_3 = 17,319 \text{ MPa} \tag{D.91}$$
$$\text{Bottom Layer (X4)} : E_4 = 22,989 \text{ MPa} \tag{D.92}$$

Each layer: 140 mm × 70 mm, $EI_{eff} = 1.35 \times 10^{12}$ N · mm^2, $L = 3600$ mm, $s = 200$ mm

Section Properties

$$A = 140 \times 70 = 9,800 \text{ mm}^2 \tag{D.93}$$
$$\tag{D.94}$$
$$I = \frac{140 \times 70^3}{12} = 4,000,833 \text{ mm}^4 \tag{D.95}$$

Individual Layer Stiffness

$$(EI)_0 = \sum_{i=1}^{4} E_i I_i \tag{D.96}$$
$$\tag{D.97}$$
$$= 19,184 \times 4,000,833 + 19,335 \times 4,000,833 + 17,319 \times 4,000,833 + 22,989 \times 4,000,833 \tag{D.98}$$
$$\tag{D.99}$$
$$= 315,373,684,091 \text{ N} \cdot \text{mm}^2 \tag{D.100}$$

Neutral Axis Position

Assuming origin at the bottom of the beam:

$$y_1 = 245 \text{ mm (centroid of top layer)} \tag{D.101}$$
$$y_2 = 175 \text{ mm (centroid of upper middle layer)} \tag{D.102}$$
$$y_3 = 105 \text{ mm (centroid of lower middle layer)} \tag{D.103}$$
$$y_4 = 35 \text{ mm (centroid of bottom layer)} \tag{D.104}$$
$$\tag{D.105}$$
$$\bar{y} = \frac{E_1A_1y_1 + E_2A_2y_2 + E_3A_3y_3 + E_4A_4y_4}{E_1A_1 + E_2A_2 + E_3A_3 + E_4A_4} \tag{D.106}$$
$$\tag{D.107}$$
$$= \frac{19,184 \times 9,800 \times 245 + 19,335 \times 9,800 \times 175 + 17,319 \times 9,800 \times 105 + 22,989 \times 9,800 \times 35}{19,184 \times 9,800 + 19,335 \times 9,800 + 17,319 \times 9,800 + 22,989 \times 9,800} \tag{D.108}$$
$$\tag{D.109}$$
$$= 135.74 \text{ mm} \tag{D.110}$$

Distance from Layer Centroids to Neutral Axis

$$a_1 = |245 - 135.74| = 109.26 \text{ mm} \tag{D.111}$$
$$\tag{D.112}$$
$$a_2 = |175 - 135.74| = 39.26 \text{ mm} \tag{D.113}$$
$$\tag{D.114}$$
$$a_3 = |105 - 135.74| = 30.74 \text{ mm} \tag{D.115}$$
$$\tag{D.116}$$
$$a_4 = |35 - 135.74| = 100.74 \text{ mm} \tag{D.117}$$

Calculation of C_1 and C_2

$$C_1 = E_1 A_1 a_1^2 + E_4 A_4 a_4^2 \tag{D.118}$$
$$\tag{D.119}$$
$$= 19,184 \times 9,800 \times 109.26^2 + 22,989 \times 9,800 \times 100.74^2 \tag{D.120}$$
$$\tag{D.121}$$
$$= 4,532,267,770,196 \text{ N} \cdot \text{mm}^2 \tag{D.122}$$
$$\tag{D.123}$$
$$C_2 = E_2 A_2 a_2^2 + E_3 A_3 a_3^2 \tag{D.124}$$
$$\tag{D.125}$$
$$= 19,335 \times 9,800 \times 39.26^2 + 17,319 \times 9,800 \times 30.74^2 \tag{D.126}$$
$$\tag{D.127}$$
$$= 452,519,689,060 \text{ N} \cdot \text{mm}^2 \tag{D.128}$$

ΔEI Calculation

$$\Delta EI = EI_{eff} - (EI)_0 \tag{D.129}$$
$$\tag{D.130}$$
$$= 1.35 \times 10^{12} - 315,373,684,091 \tag{D.131}$$
$$\tag{D.132}$$
$$= 1,034,626,315,909 \text{ N} \cdot \text{mm}^2 \tag{D.133}$$

Quadratic Equation Setup for K

$$a = 2 \times \Delta EI = 2 \times 1,034,626,315,909 = 2,069,252,631,818 \tag{D.134}$$
$$\tag{D.135}$$
$$b = -\frac{2C_1}{3} = -\frac{2 \times 4,532,267,770,196}{3} = -3,021,511,846,797 \tag{D.136}$$
$$\tag{D.137}$$
$$c = -(\Delta EI + \frac{C_1}{3} + C_2) \tag{D.138}$$
$$\tag{D.139}$$
$$= -(1,034,626,315,909 + \frac{4,532,267,770,196}{3} + 452,519,689,060) \tag{D.140}$$
$$\tag{D.141}$$
$$= -2,997,901,928,368 \tag{D.142}$$

Solve for K

$$K = \frac{-b\sqrt{b^2 - 4ac}}{2a} \tag{D.143}$$

$$= \frac{3,021,511,846,797 + \sqrt{(-3,021,511,846,797)^2 - 4 \times 2,069,252,631,818 \times (-2,997,901,928,368)}}{2 \times 2,069,252,631,818} \tag{D.144}$$

$$= 2.138, -0.678 \tag{D.145}$$

Discard the negative value

Calculate K_{ser}

$$E_1, E_2, E_3, E_4 = 19184, 19335, 17319, 22989 \tag{D.146}$$

$$\tag{D.147}$$

$$k_{ser_1} = \frac{\pi^2 \times E_1 \times A \times s}{L^2 \times 2 \times (K-1)} \tag{D.148}$$

$$\tag{D.149}$$

$$= \frac{\pi^2 \times 19,184 \times 9,800 \times 200}{(3,600)^2 \times 2 \times (2.138 - 1)} \tag{D.150}$$

$$\tag{D.151}$$

$$= 12,581 \text{ N/mm} \tag{D.152}$$

D.3.4. Four-Layered Beam (B2-2)

The four-layered beam configuration has the following arrangement:

$$\text{Top Layer (X7)} : E_1 = 18,203 \text{ MPa} \tag{D.153}$$

$$\text{Upper Middle Layer (X1)} : E_2 = 18,245 \text{ MPa} \tag{D.154}$$

$$\text{Lower Middle Layer (X3)} : E_3 = 23,658 \text{ MPa} \tag{D.155}$$

$$\text{Bottom Layer (X2)} : E_4 = 18,099 \text{ MPa} \tag{D.156}$$

Section Properties

For each layer (140 mm × 70 mm):

$$A = 140 \times 70 = 9,800 \text{ mm}^2 \tag{D.157}$$

$$\tag{D.158}$$

$$I = \frac{140 \times 70^3}{12} = 4,000,833 \text{ mm}^4 \tag{D.159}$$

Individual Layer Stiffness

$$(EI)_0 = \sum_{i=1}^{4} E_i I_i \tag{D.160}$$

$$\tag{D.161}$$

$$= 18,203 \times 4,000,833 + 18,245 \times 4,000,833 + 23,658 \times 4,000,833 + 18,099 \times 4,000,833 \tag{D.162}$$

$$\tag{D.163}$$

$$= 312,904,903,417 \text{ N} \cdot \text{mm}^2 \tag{D.164}$$

Neutral Axis Position

Assuming origin at the bottom of the beam:

$$y_1 = 245 \text{ mm (centroid of top layer)} \tag{D.165}$$
$$y_2 = 175 \text{ mm (centroid of upper middle layer)} \tag{D.166}$$
$$y_3 = 105 \text{ mm (centroid of lower middle layer)} \tag{D.167}$$
$$y_4 = 35 \text{ mm (centroid of bottom layer)} \tag{D.168}$$
$$\tag{D.169}$$
$$\bar{y} = \frac{E_1A_1y_1 + E_2A_2y_2 + E_3A_3y_3 + E_4A_4y_4}{E_1A_1 + E_2A_2 + E_3A_3 + E_4A_4} \tag{D.170}$$
$$\tag{D.171}$$
$$= \frac{18,203 \times 9,800 \times 245 + 18,245 \times 9,800 \times 175 + 23,658 \times 9,800 \times 105 + 18,099 \times 9,800 \times 35}{18,203 \times 9,800 + 18,245 \times 9,800 + 23,658 \times 9,800 + 18,099 \times 9,800} \tag{D.172}$$
$$\tag{D.173}$$
$$= 138.94 \text{ mm} \tag{D.174}$$

Distance from Layer Centroids to Neutral Axis

$$a_1 = |245 - 138.94| = 106.06 \text{ mm} \tag{D.175}$$
$$\tag{D.176}$$
$$a_2 = |175 - 138.94| = 36.06 \text{ mm} \tag{D.177}$$
$$\tag{D.178}$$
$$a_3 = |105 - 138.94| = 33.94 \text{ mm} \tag{D.179}$$
$$\tag{D.180}$$
$$a_4 = |35 - 138.94| = 103.94 \text{ mm} \tag{D.181}$$

Calculation of C_1 and C_2

$$C_1 = E_1A_1a_1^2 + E_4A_4a_4^2 \tag{D.182}$$
$$\tag{D.183}$$
$$= 18,203 \times 9,800 \times 106.06^2 + 18,099 \times 9,800 \times 103.94^2 \tag{D.184}$$
$$\tag{D.185}$$
$$= 2,007,429,118,048 \text{ N} \cdot \text{mm}^2 \tag{D.186}$$
$$\tag{D.187}$$
$$C_2 = E_2A_2a_2^2 + E_3A_3a_3^2 \tag{D.188}$$
$$\tag{D.189}$$
$$= 18,245 \times 9,800 \times 36.06^2 + 23,658 \times 9,800 \times 33.94^2 \tag{D.190}$$
$$\tag{D.191}$$
$$= 324,711,456,157 \text{ N} \cdot \text{mm}^2 \tag{D.192}$$

ΔEI Calculation

Given experimental $EI_{eff} = 1.36 \times 10^{12}$ N $\cdot$ mm^2:

$$\Delta EI = EI_{eff} - (EI)_0 \tag{D.193}$$
$$\tag{D.194}$$
$$= 1.36 \times 10^{12} - 312,904,903,417 \tag{D.195}$$
$$\tag{D.196}$$
$$= 1,047,095,096,583 \text{ N} \cdot \text{mm}^2 \tag{D.197}$$

Quadratic Equation Setup for K

$$a = 2 \times \Delta EI = 2 \times 1,047,095,096,583 = 2,094,190,193,166 \tag{D.198}$$
$$\tag{D.199}$$
$$b = -\frac{2C_1}{3} = -\frac{2 \times 2,007,429,118,048}{3} = -1,338,286,078,699 \tag{D.200}$$
$$\tag{D.201}$$
$$c = -(\Delta EI + \frac{C_1}{3} + C_2) \tag{D.202}$$
$$\tag{D.203}$$
$$= -(1,047,095,096,583 + 669,143,039,349 + 324,711,456,157) \tag{D.204}$$
$$\tag{D.205}$$
$$= -2,040,949,592,089 \tag{D.206}$$

Solve for K

$$K = \frac{-b + \sqrt{b^2 - 4ac}}{2a} \tag{D.207}$$
$$\tag{D.208}$$
$$= \frac{1,338,286,078,699 + \sqrt{(-1,338,286,078,699)^2 - 4 \times 2,094,190,193,166 \times (-2,040,949,592,089)}}{2 \times 2,094,190,193,166} \tag{D.209}$$
$$\tag{D.210}$$
$$= 1.355, -0.718 \tag{D.211}$$

Discard the negative value

Calculate K_{ser}

Given span length $L = 3600$ mm and fastener spacing $s = 200$ mm:

$$k_{\text{ser}_1} = \frac{\pi^2 \times E_1 \times A_1 \times s}{L^2 \times 2 \times (K - 1)} \tag{D.212}$$
$$= \frac{\pi^2 \times 18\,203 \times 9\,800 \times 200}{(3\,600)^2 \times 2 \times 0.355} \tag{D.213}$$
$$= \frac{\pi^2 \times 18\,203 \times 9\,800 \times 200}{25\,920\,000 \times 0.71} \tag{D.214}$$
$$= 19\,133 \text{ N/mm} \tag{D.215}$$

D.3.5. Empirical Formula Calculation

The empirical formula for K_{ser} is:

$$K_{ser} = \frac{\rho^{1.5} \times d}{23} \tag{D.216}$$

$$\tag{D.217}$$

Given wood density $\rho = 1080$ kg/m^3 and dowel diameter $d = 20$ mm:

$$K_{ser} = \frac{1080^{1.5} \times 20}{23} \tag{D.218}$$

$$\tag{D.219}$$

$$= 30,864 \text{ N/mm} \tag{D.220}$$